UNIVERSITY RESEARCH PROGRAM IN ROBOTICS

Robotics Technology Development Program
Grant No.: DE-FG52-2004NA25588

TECHNICAL FINAL ANNUAL REPORT
Project Period: 9/1/04 – 8/31/05

Investigators
James S. Tulenko – P.I.
Carl D. Crane, III – Co-P.I.

University of Florida
College of Engineering

P.O. Box 118300, Gainesville, FL, 32611-8300
(352) 392-1401 · (352) 392-3380
tulenko@ufl.edu

Table of Contents

Appendices (Attached)

Research Team Personnel

A. Principal Faculty

Prof. James S. Tulenko, P.I.
Dr. Carl D. Crane, Co-P.I.

B. Associated Faculty

Dr. David Hintenlang
Dr. James Kurtz

C. Sub Faculty & Administrative

Dr. Dean Schoenfeld
Charles L. Scheer

D. Students Supported and Funded

Blair Smith	Ph.D.
Bo Zhang	Ph.D
Hyun Kwon Jung	Ph.D
Jahan Bayat	Ph.D.
Jose Santiago	Ph.D
Julio Correa	Ph.D.
Shannon Ridgeway	Ph.D.
Jean F. Kamath	Ph.D.
Memet Unsal	Ph.D.
Jiwei Wang	M.S.
Ryan Fisher	M.S.

Publications & Reports Issued

- "*Design Optimization of Radionuclide Nano-Scale Batteries,"* Dean Schoenfeld, et al, ANES/SENA 2004 Symposium, Miami Beach, FL, October, 2004.

- "*The Optimum Plutonium Inert Matrix Fuel Form for Reactor-Based Plutonium Disposition,"* James S. Tulenko, et.al, ANES/SENA 2004 Symposium, Miami Beach, FL, October, 2004.

- *"Processing of clinical images for guidance of robotic assisted procedures,*" D.E. Hintenlang, 10th International Conference on Robotics and Remote Systems for Hazardous Environments, 405-410, Gainesville, FL, March 2004.

- "*Design and Implementation of a Modular Manipulator Architecture,*" "A Sosa, O., M.S. Thesis, 2004.

- "*Development of an Autonomous Navigation Technology Test Vehicle,*" Tobler, C., M.S. Thesis, 2004.

- "*Closed-Form Equilibrium Analysis of a Planar Tensegrity Structure*," Bayat, J., and Crane, C., On Advances in Robot Kinematics, Kluwer Academic Publishers, pp. 313-320.

- *"Two Semi-Active Approaches for Vibration Isolation: Piezoelectric Friction Damper and Magnetorhelogical Damper,*" Unsal, M., Niezrecki, C., and Crane, C., Proceedings of the IEEE International Conference on Mechatronics, Istanbul, Turkey, June 2004.

- *"Control Considerations in the Design of a Parallel Kinematic Machine with Separate Actuation and Metrology Mechanisms,*" Ridgeway, S., and Crane, C., Proceedings of the 12th Mediterranean Conference on Control and Automation (MED '04), Kusadasi, Turkey, June 2004.

- *"Autonomous Ground Vehicle Path Tracking,*" Wit, J., Crane, C., and Armstrong, D., Journal of Robotic Systems, Vol. 21, Issue 8, pp. 439-449.

- "*Static Analysis of Tensegrity Structures,*" Correa, J., Crane, C., and Duffy, J., ASME Journal of Mechanical Design, Vol. 127, Issue 2, pp. 257-268.

Terms & Acronyms

AND	Computer 2-state Boolean Logic
CMOS	Complementary Metal Oxide Semi-Conductor
COTS	Commercial off-the-shelf
CMOS Resolver	Complementary Metal Oxide Semiconductor EVBU
GaAs	Gallium Arsenide
GaN	Gallium Nitride
GPIP Bus	General Purpose Interface Bus
JFET	Junction Field Effect Transistor
JPG	JPEG, for Joint Photo Experts Group, a photo file format
LMS	Laser Measuring System
LSI	Large Scale Integration
MOS	Metal oxide semiconductor dosimeters (also radfets)
MOSFETs	Metal-Oxide Semiconductor Field-Effect-Transistors
MOT	Metal-oxide technology
NAND	Negative 2-state computer Boolean logic
NOR	Negative “also” 2-state computer Boolean logic
OR	“Also” 2-state computer Boolean logic
PCCFC	Parallel Compliant Coupler for Force Control
Quadrature	Compare two wave forms of differing phases
Quantized	Subdivided into small, measurable increments
RADFET	Solid State Radiation Dosimeter Field-Effect-Transistors
RDC	Resolver to Digital Converter
RGB	Red, Green, Blue
SOI	Silicon on insulator
TTL	Transistor logic gate
TLM	Transmission Line Method to determine resistivity
UTMC	Rad hard device manufacturer
Vrms meter	Voltage reading meter
WCPMMI	Weight Compensating Parallel Manipulator/Manual Input
XOR gate	Exclusive “no ambiguous” 2-state computer logic

UF 1.0 MEMS & Rad-Hard Technologies

1.1 Nano-Scale Radioisotope Batteries

1.1.1 Objectives

Responding to NNSA/DOE goals during this twelve month period (6/04-5/05), UF evaluated conversion technologies of nano-scale radioisotope batteries for MEMS applications with emphasis on radiation environments. UF's goal was to assess the applicability of fundamental calculations with MCNP (Monte Carlo N-Particle Transport Code) and EGSnrc (Electron-Gamma-Shower program by the National Research Council of Canada) codes for modeling charged particle transport and radiation capture in extremely small scale devices during this phase of the research. Calculations investigated both direct energy conversion pathways and those combined with indirect conversion. The evaluation of luminescent materials for indirect conversion pathways, known to be sensitive to radiation effects, will be addressed in future work.

The UF objective supports development of remote systems to perform visual inspections, monitor operations and enhance security capabilities while minimizing radiation exposure to humans. It can be expected that miniature power supply capabilities will evolve as new technologies are developed and become integrated in the technologies of microsensors, microactuators, and nanotechnology. These developments will create new opportunities for successful implementation of novel nano-scale radioisotope batteries.

1.1.2 Background

This research objective originated with the realization that nanotechnology motors currently being developed need energy sources with comparable dimensions. Current technology suggests an energy converter employing radioactive disintegration has a very favorable energy density advantage over all other energy sources for creation of nano-scale batteries. Nuclear battery technology saw its beginning around 1913, and has received considerable research attention for applications requiring long-life power sources for space. The scientific principles are well known, but modern nano-scale technology and new wide bandgap semiconductors have created potential new devices and interesting material properties not previously available. MEMS nano-scale devices fall into two general power levels based on the transduction scheme. MEMS capacitive and piezoelectric devices are lower power, but higher voltage due to the high

impedance load. Piezoresistive and thermoelastic devices meanwhile are low voltage, but produce higher power. Typical microbattery applications having an effective life measured in years will require a few microamps of current, 1 to 7 volts and power ratings of 10 to 500μW.

Significant gains in semiconductor materials, fabrication equipment, processing methods and higher purity / low defect materials have combined with UF's fundamental understanding of the underlying physics for nano-scale device properties required to develop a working nano-tech battery. The ongoing work of industry, universities and government programs continue to produce major advances crucial to MEMS technology. These state-of-the-art accomplishments promise that UF will eventually meet the challenging goal of developing a long-life nano-scale nuclear battery compatible with MEMS motors and power requiring devices.

1.1.3 Approach

UF directed its research experience in radiation effects on electronics and simulation/ calculation capabilities to discover novel approaches leading to the development of a nano-scale radioisotope MEMS battery. The application of radioisotope knowledge in MEMS dimensions requires major improvements and essential modification of current radioisotope battery designs. UF research experience in the subtleties of radiation transport and absorption is focusing on nanostructures and superlattice solid state devices. This research effort includes analysis and simulation methods crucial for evaluation of radioisotope nano-battery designs implemented in semiconductor materials. Research at the UF Robotics Lab focused on the task of understanding what Monte Carlo codes can and cannot accomplish in the nanometer realm. Two codes were compared, the powerful but unwieldy EGSnrc code and the well-known MCNP5 code. Both codes are routinely used in nuclear engineering and medical physics, but neither code has been extensively used or proven as a tool for studying nanotechnology systems. The initial methodology for comparing and benchmarking these codes with nano-scale structures used a series of quasi-one dimensional test cases, comprising a superlattice structure of fixed height ($\Delta z < 100$ nm). These nanometer radiation conversion layers were surrounded by two buffer zones of p-type and n-type semiconductors (total $z = 2.1\mu m$). A sapphire substrate was modeled (with an essentially large arbitrarily thickness for full absorption). For simplicity a semi-infinite geometry xy-plane was set up, and these ultra thin layers were all assumed infinite in area. The nanoscale thickness of layers in the z direction (normal to the surfaces) combined with infinite xy-planes makes each case a virtual 1-

dimensional problem. The amount of incident $\tilde{\beta}$ energy absorbed in each layer was then calculated by the two codes for different number of superlattice layers ($\Delta z < 100$ nm kept constant), and the results were evaluated. Rudimentary structures designed to isolate key characteristics provided additional information guiding the design pathway for efficient energy conversion in nano- dimensional space. A fundamental issue was a comparison of energy density and radionuclide specific activity. The parameters were examined to evaluate their roles in determining battery dimensions in ultra thin layer semiconductor designs. Previous studies report that nanotechnology materials frequently present characteristics and properties leading to novel developments. It is commonly believed that the basic mechanisms controlling battery conversion power and efficiency are proportional to geometric scale in macro dimensions. Evolving nanoscale technology has shown promise in changing this perception. Additional progress in developing nano-scale battery technology is projected with batteries immune to radiation induced defects from alpha, beta and gamma energy sources. An evaluation of high radiation tolerance to promote use of both direct and indirect conversion methodologies also was conducted. This study seeks to develop longer-life and higher conversion efficiency batteries. This emphasis on gaining a better understanding of physical principles will lead to improvements in nanoscale radioisotope battery designs.

1.1.4 Quarterly Benchmarks

Q1: Perform calculations to study relation of radiation penetration versus specific activities of radionuclides

Improve models of radioisotope sources for calculations (emission Spectrum)

Submit abstract to Americas Nuclear Energy Symposium 2004

Q2: Investigate limitations of candidate semiconductors materials

Submit abstract to ANS 2004 Winter Meeting

Q3: Study limitations of material selection for dielectrics, metallization, etc.

Provide summary of key results

Q4: Perform MCNP and EGS analysis of basic radioisotope battery model

Present research results at ANES (Oct.) and ANS Winter (Nov.) Meetings

1.1.5 Discussion and Results

The quarterly goals for the nano-scale radioisotope battery, outlined in section UF 1.1.4, were completed by work in a number of important areas. These were:

- EGS penetration studies
- Improve models of radioisotope sources
- Evaluate candidate semiconductors
- Dielectric Material selection issues
- MCNP & EGS model
- Analysis of basic model
- Presentation of key design parameters at 2nd Annual TechTransfer Conference

1.1.5.1 EGS penetration studies

The Electron-Gamma-Shower (EGSnrc) program provides an excellent way to evaluate basic concepts for a radioisotope nuclear battery. The literature provides numerous examples of designs for both alpha and beta particle batteries using older proven technologies. The UF approach to new battery designs favors fabrication using semiconductor technology and recent advances provided by nanotechology. Scaling or size involves two separate issues. The active region in which semiconductor energy conversion occurs is in the submicron region, while the total power is often related to physical area and larger dimensions. EGS calculations for the III-V semiconductor GaAs are shown in the two tables below (Figures 1.1.5.1-1a&b).

EGS penetration studies (Helium-Alpha Particle)

Ion Energy	$Ga^{0.7}$ $Al^{0.3}$ As	$Ga^{0.95}$ $Al^{0.05}$ As	GaAs	Δ-delta
1 KeV	72 Aº	69 Aº	68 Aº	4 Aº
10KeV	603 Aº	575 Aº	570 Aº	33 Aº
100KeV	4722 Aº	4638 Aº	4622 Aº	100 Aº
1MeV	2.83 μm	2.78 μm	2.77 μm	600 Aº

MCNP5 penetration studies (Electron-Beta Particle)

Ion Energy	$Ga^{0.7}$ $Al^{0.3}$ As	$Ga^{0.95}$ $Al^{0.05}$ As	GaAs	Δ-delta
1 KeV	283 Aº	312 Aº	285 Aº	4 Aº
10KeV	9,973 Aº	11,695 Aº	9,952Aº	3 Aº

100KeV	499,320 Aº	599,431 Aº	496,191 Aº	0 Aº
1MeV	1,282 μm	1,555 μm	1,270 μm	0 Aº

Figures 1.1.5.1-1a&b Alpha and Beta penetration into two concentrations of AlGaAs

Earlier research reports have shown that MCNP5 has the capability to yield qualitatively similar and occasionally quantitatively comparable results to EGSnrc in problems involving electron transport and deposition through nanoscale superlattice structures. Such problems need to be solved in the UF NNSA research project on radioisotope nanobatteries. When dealing with direct energy conversion pathways for the radioisotope, quantitative agreement between MCNP5 and EGSnrc calculations is sought in order to develop realistic models of radiation energy deposition in the sensitive layers of a prototype design for a nuclear nanobattery. UF conducted a study of energy deposition as a function of depth normal to an infinite plane of AlGaN material, using equivalent simulation input parameters for both codes. The depth deposition from a surface point source of 17.4 keV (63Ni average β^- decay energy) to the surface depth resulting in accumulation of 25% electron energy (absorption) was calculated in both codes. The MCNP5 run used AlGaN in atomic fraction ratio 1:1:1, and with ρ = 4.4g/cm^3. A mesh of cells was overlaid on the homogeneous AlGaN slab. This allowed a profile to be determined and the results are illustrated in the following graph (Figure 1.1.5.1-2).

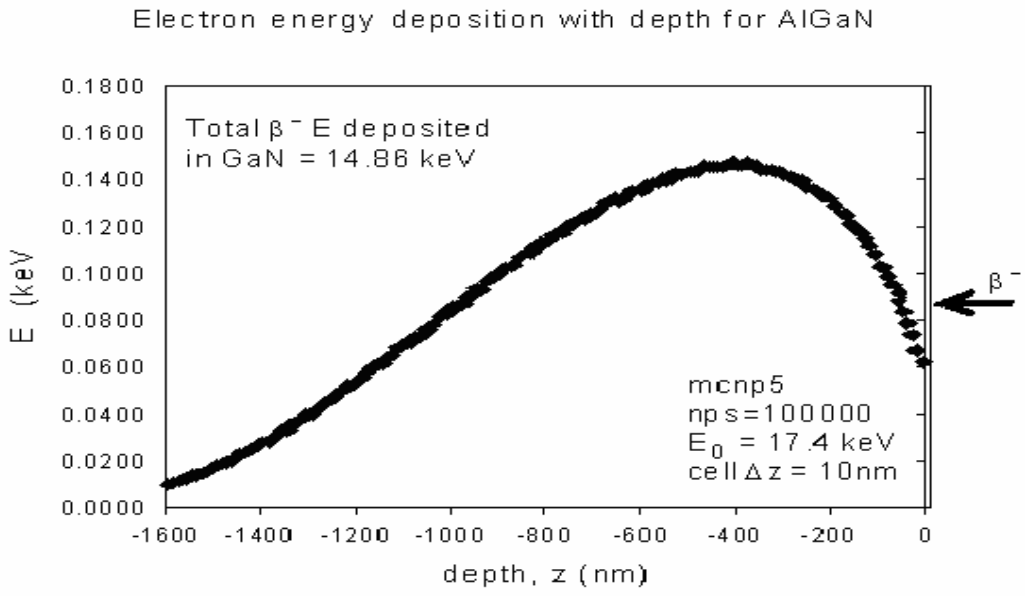

Figure 1.1.5.1-2 Electron energy versus depth in AlGaN for point source

These calculations used the concept of a "meshed cell." A meshed call refers to a connected region of the geometrical space that is occupied by a single homogeneous type of material (in this case AlGaN), but which for tallying purposes is split into multiple cells, thus a split cell is formed by introducing additional surfaces. Such a split cell does not affect electron transport because the additional internal surfaces that create the mesh are not physical interfaces between different materials. This may be true for the EGSnrc code, but it does not hold true for MCNP because MCNP treats all surfaces, even those used to split cells, as boundaries that electrons must cross. This introduces boundary crossing artifacts in MCNP, which become visible when small voxels or thin layers are created with a mesh. This feature in macro dimensions is seen in tallies of recoils at interface boundaries of materials with different densities.

This simplest cell structure resulted in no statistical difference between EGS4nrc and MCNP5 calculations. Modifying the tally to calculate the cumulative energy absorbed results in the following graph (Figure 1.1.5.1-4) .

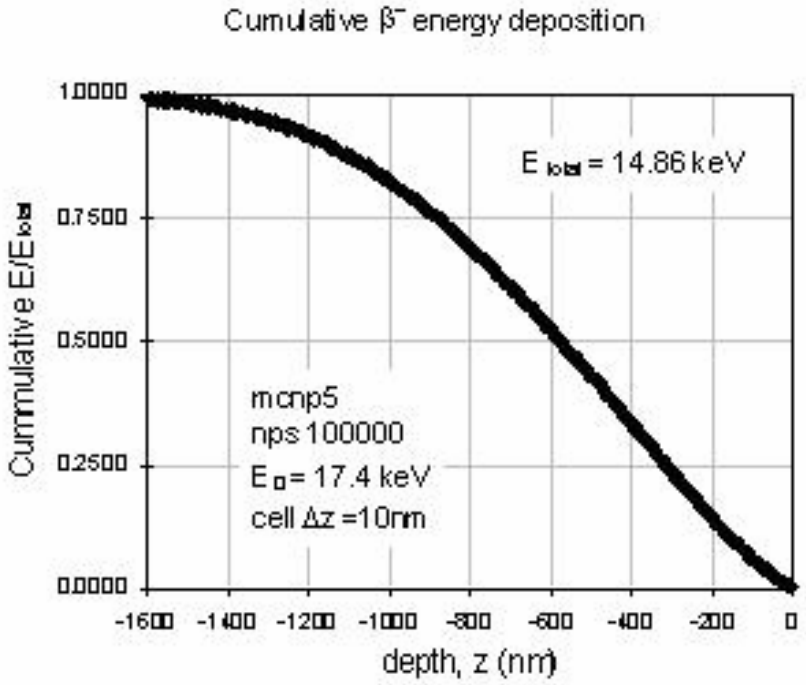

Figure 1.1.5.1-4 Cumulative fractional energy absorption for a 17.4 keV electron incident on AlGaN

1.1.5.2 Improve Models of Radioactive Sources

A Nickel (^{63}Ni) isotope with an end-point energy of 67 KeV (average 17.6 KeV) and a half-life of 92 years has been used as the radioisotope battery source. The energy spectrum of nickel's Beta-minus (β^-) disintegrations is fully documented and compatibility with semiconductor processing to make it a radiation source of interest. UF conducted Monte Carlo N-Particle Transport Code (MCNP5) calculations to determine the effects of self-absorption on the total effective emitted spectrum of β^- disintegrations. The graph (Figure 1.1.5.1-5) below was constructed from these calculations.

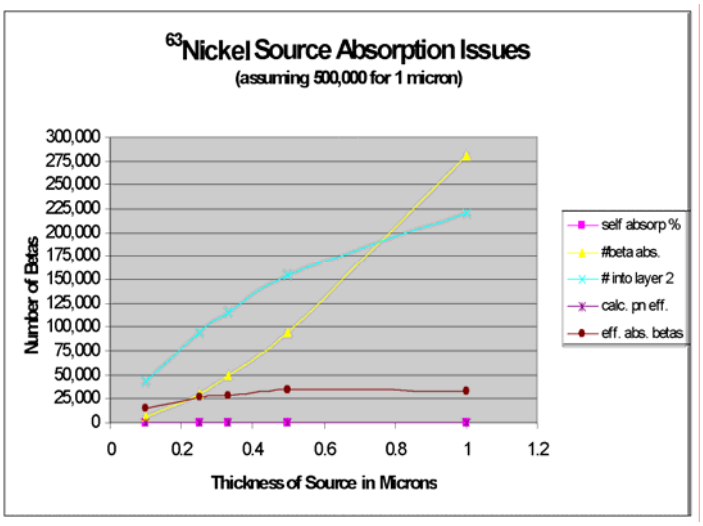

Figure 1.1.5.1-5 Evaluation of self-absorption in ^{63}Ni

The graph shows that the absorption of β^- particles increases significantly as the thickness approaches 1 micron. Many of the low energy β^- particles do not make it out of the source volume. This information is combined in a simulation using a simple silicon pn-junction conversion model optimized by matching the penetration depth with the space charge region of the active junction. When the physical restraints of direct energy conversion are combined with the self-absorption of the source, an optimum source thickness of ~ 0.5 microns is found to yield the highest overall efficiency. This information is shown in the following graph (Figure 1.1.5.1-6).

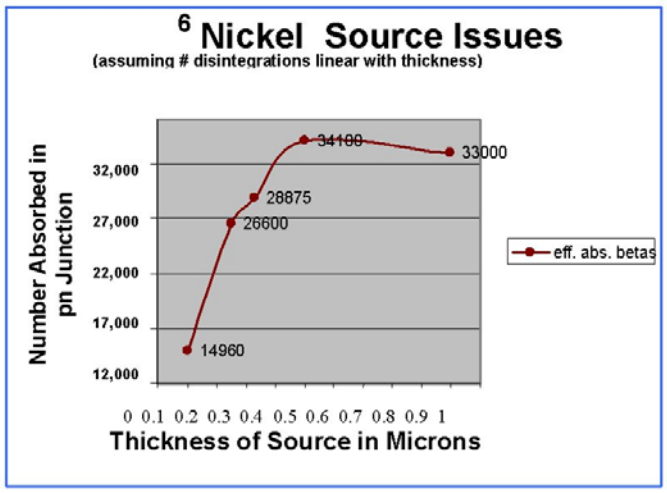

1.1.5.1-6 Optimum Source Thickness for Highest Conversion

1.1.5.3 Evaluate Candidate Semiconductors

Among evaluation criteria for candidate semiconductor, basic properties involving radiation tolerance, semiconductor processing capabilities, direct bandgap potential for reduced non-irradiative recombination, and transparency were studied. Progress during the last year has clarified realistic direct conversion pathways and pointed out the potential benefits of transparent conversion devices with engineered bandgaps in tandem stacked arrays. Full description and testing results of these efforts are reported in UF 1.2.

1.1.5.4 Dielectric Material Selection Issues

Photovoltaic devices based on the III-V and II-VI semiconductor families are different and do not create dielectric isolation with oxides common to silicon technology. Furthermore, ultra-thin isolation layers required by 45 nm technology devices now require fabrication methods for high dielectric constant materials. Concurrent with this development is the totally opposite transparent contact development and copper/ultralow-k structures for copper back-end interconnects. Candidates include vanadium oxide, organic based polymers and even ceramic structures. These state-of-the-art developments will be a focus of next year's work.

1.1.5.5 MCNP & EGS Model

Monte Carlo transport codes, despite some limitations, provide an excellent way to analyze and compare different design concepts for nano-scale radioisotope energy converters. Careful selection of key parameters, such as step size, allow general concepts to be demonstrated. Calculations were conducted for a representative superlattice structure common to many recent photovoltaic devices. Three different models were chosen for the 70nm superlattice layers. One, two and five repeating layers were used for the fixed 70nm thickness. Using ^{63}Ni as incident radioisotope source, the initial β^- electron kinetic energy is 66.9 KeV. The results are shown below (Figure 1.1.5.1-7, 8, and 9):

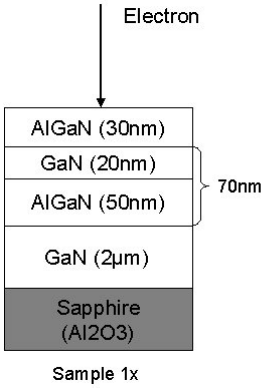

REGION	ENERGY FRACTION
Reflected	**0.13570393621922**
30 nm AlGaN	**0.00093059270876**
20 nm GaN	**0.00084997667000**
50 nm AlGaN	**0.00176707131322**
2 µm GaN	**0.15156464278698**
5 cm Al2O3 Sapphire	**0.70917260646820**
Transmitted	**0.00000000000000**

Figure 1.1.5.1-7 Data for a single repeat layer in the superlattice 70nm

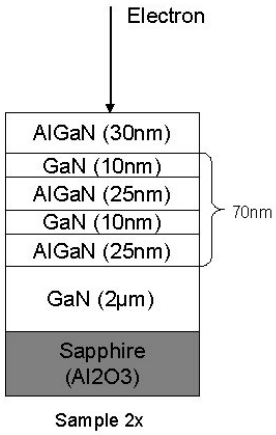

REGION	ENERGY FRACTION
Reflected	**0.14802700281143**
30 nm AlGaN	**0.00104431330692**
10 nm GaN	**0.00047064098180**
25 nm AlGaN	**0.00086734571960**
10 nm GaN	**0.00043829815695**
25 nm AlGaN	**0.00088805973064**
2 µm GaN	**0.15712058544159**
5 cm Al2O3 Sapphire	**0.69113129377365**
Transmitted	**0.00000000000000**

Figure 1.1.5.1-8 Data for a two repeat layers in the superlattice 70nm

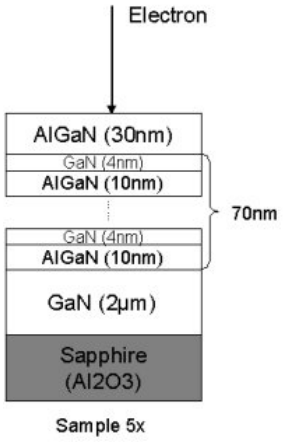

REGION	ENERGY FRACTION
Reflected	**0.14818544685841**
30 nm AlGaN	**0.00103564769961**
4 nm GaN	**0.00019263307331**
10 nm AlGaN	**0.00039630476385**
4 nm GaN	**0.00021354309865**
10 nm AlGaN	**0.00035815767478**
4 nm GaN	**0.00019977764168**
10 nm AlGaN	**0.00037060229806**
4 nm GaN	**0.00021518454014**
10 nm AlGaN	**0.00042862552800**
4 nm GaN	**0.00019589612202**
10 nm AlGaN	**0.00039924986777**
2 µm GaN	**0.15533900260925**
5 cm Al2O3 Sapphire	**0.69245749711990**
Transmitted	**0.00000000000000**

Figure 1.1.5.1-9 Data for a five repeat layers in the superlattice 70nm

These results indicate that the energy deposit in the desired region increases slightly with increasing number of layers. The higher specific activity of the ^{63}Ni radioisotope results in the majority of the β^- electron kinetic energy stopping outside the effective collection zone of the energy converter. This allows multiple conversion devices to be stacked in a vertical configuration for collection from multiple devices. Earlier simulations provided proof of the concept of designing each converter device to absorb equivalent β^- electrons. This allows matching of performance from each energy converter in series so it would not be limited by the weakest link. This is a concept experienced in multi-battery flashlights. If one limits designs to the existing technology based on the macro world, direct converters are not likely efficient enough to create a nano-scale device.

Another basic design concept researched through calculations and simulations using the MCNP5 and EGSnrc transport codes investigated geometric conversion limitations imposed by semiconductor technology. The central issue was determining when edge losses begin to significantly limit the overall efficiency. A simple square ^{63}Ni radioisotope top uniform surface source (thickness to area ratio adjusted so total number of disintegrations remains constant) was used in the simulations with square dimensions of 100µm, 50µm , 25µm , 10µm , 5µm , 2µm , and 1µm. Tallies of the total β^- electrons entering the top surface of the radioisotope converter were then compared. The edge losses became important at 5µm x 5µm size to the overall efficiency and very limiting at 2µm x 2µm . This suggests conversion devices fabricated with

semiconductor technology may be nanometer in vertical layer thickness but must remain 5μm square (or larger) for optimum efficiency.

1.1.5.6 Basic Model Development

The maximum theoretical value of $\eta = 6\%$ for radioisotope direct conversion is limited by reduced Voc (much smaller than the contact potential difference voltage). This design converts electron-hole pairs, swept by the p-n junction electric field, which arise only in the p-region at the distance from the p-n junction shorter than the electron diffusion length. The overall efficiency is decreased by any contact resistance, interconnection loses, recombination processes, and phonon generated heat.

The weak conversion of radioisotope decay energy available with direct conversion methods evolves to consideration of radioluminescent light indirect conversion for improved power output. Photovoltaic (PV) conversion of monochromatic light has been demonstrated to over 60% at moderate illumination levels. The literature reports a tritium battery using a silicon-based photovoltaic (PV) cell with a vertical junction (≥2μm). Its battery current of 1μA can be obtained with a minimum beta cell area of $10cm^2$. A source of bound tritium in titanium (~1000Å) is projected to provide up to $1.5\mu W/cm^2$ with a conversion current $I_{sc} = 240nA/cm^2$, and Voc = 240mV. A useful semiconductor nuclear battery with an operating voltage of 1.6V would require connection of 16 cells in series.

UF has looked at tandem PV cells and arrays in III-V and II-VI semiconductor materials for generating useful power levels. Two major areas of interest have been radiation tolerance of contacts and luminescent materials in relation to their damage thresholds (ability to withstand higher specific activity radioisotopes). Expansion of the useful PV spectrum is proposed through transparent contacts on II-VI semiconductors. Gallium-Nitride (GaN) and Zinc-Oxide (ZnO) are two major candidates in UF's studies. Both allow engineered bandgaps (E_g depends on alloy compositions-Figure 1.1.5.1-10) and are current state-of-the-art materials receiving significant attention. ZnO's first reported successful p-contact was development at Florida. UF irradiation studies of these materials has resulted in three publications covering radiation effects and ohmic contact performance.

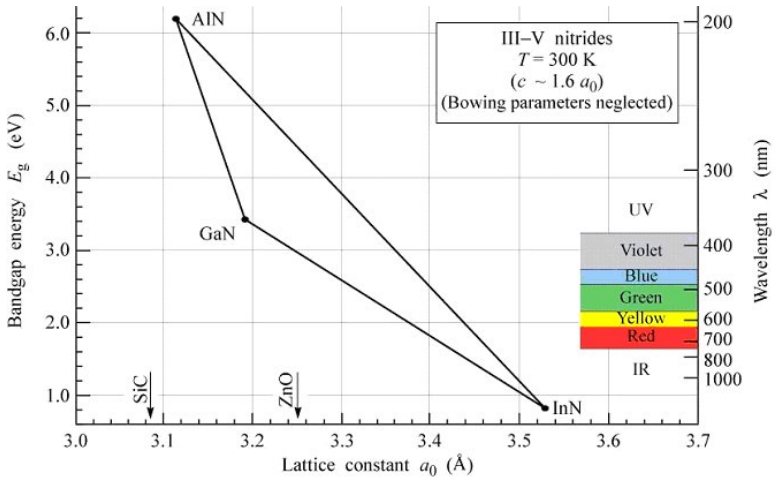

Figure 1.1.5.1-10 Bandgap Energy Versus Lattice Constant of III-V Nitride Semiconductors at Room Temperature

The various families of III-V materials are determined in large part by the wavelength ranges within which they emit and absorb light efficiently. This enables high-performance "band-gap engineered" heterostructures and devices with optical and electronic properties difficult to achieve in other materials. Some common III-V semiconductors are:

- GaAs-related materials: 0.8-1.0 µm
- InP-related materials: 1.3-1.7 µm
- GaN-related materials: 0.3-0.6 µm
- InSb-related materials: 2-10 µm
- GaP-related materials: 0.5-0.7 µm and recently,
- CuInSe2 (Eg= 1.04 eV)
- CuGaSe2 (Eg= 1.68 eV)
- CuIn0.7Ga0.3Se2 (Eg= 1.14 eV), and
- CuInS2 (Eg ≈ 1.5 eV).

The latest reported major breakthrough in interconnect technology was announced in the August, 2005 issue of Semiconductor International. "Aligned Wafer Bonding for 3-D Interconnect" holds promise for significant improvements in matched tandem arrays of PV cell using radioluminescent materials for indirect conversion batteries. (See References, next page.)

Optimization of the individual converter cell would be greatly enhanced by removal of many restriction associated with interconnection issues. Furthermore, the radiation tolerant wide-bandgap II-VI semiconductors can be used to rain in the damaging effects of higher

kinetic electrons to levels compatible with the lower damage thresholds of many luminescent materials. Two advantages offered by this approach are reductions in the number of radioisotope and luminescent layers. A sandwiched layer of radioisotope, surrounded by tandem PV cells arrays, might only require a single external luminescent coating. These basic prototype design elements are pictured in Figure 1.1.5.1-11.

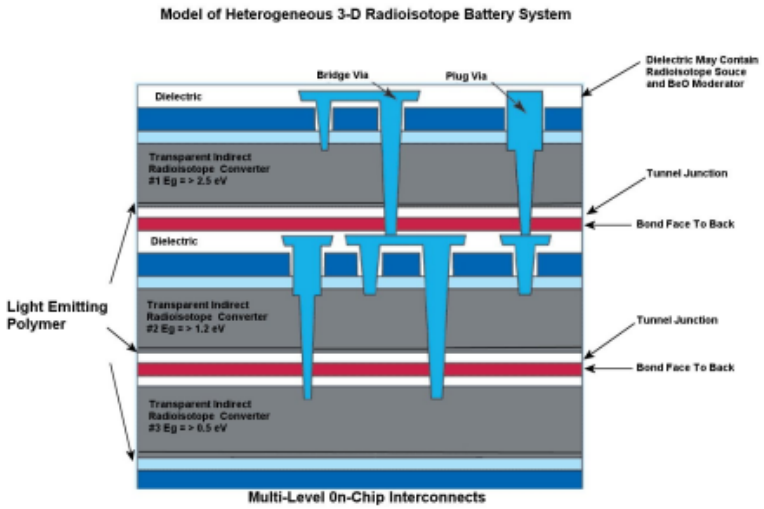

Figure 1.1.5.1-11 Prototype nano-scale radioisotope PV conversion cell

1.1.5.7 Presentation of Key Design Parameters at 2nd Annual Techtransfer Conference

The University Research Program in Robotics (URPR) at Florida continues development of remote long-term radioisotope batteries designed for microelectromechanical systems (MEMS) applications. The NNSA mission faces a rapidly expanding need for miniature long-life remote power sources compatible with evolving nanotechnology applications.

REFERENCES

- *"Wafer-Level 3-D Hyper-Integration Processing Technology,"* J.Q.Lu, 3-D Technology, Modeling and Process Symp., April 2004.
- "*Wafer-Level 3-D Interconnects Via Cu Bonding,*" P. Morrow et al., Proc. Of Advanced Metallization Conf., 2004.

UF presented highlights from its radioisotope nano-scale battery research at the 2nd Annual TechTransfer Conference in Orlando, Florida in May, 2005. Information presented covered radioisotope source design (self-absorption and emission energy spectrum), mitigation of radiation effects with use of wide band-gap materials, the benefits/challenges of tandems/multimode conversion designs, and other important factors affecting overall efficiency in reduced dimensional geometries. Issues identified as important to development of a nano-scale radioisotope battery included: ecological compatibility, low toxicity, relatively low cost, suitable half-life, power density, and absorption of radioactive species with ultra-thin layers.

1.2 Rad-Hard Technologies and Development of MEMS Devices

1.2.1 Objective

The UF objective in support of the development of a nano-scale radioisotope battery sought expanded radiation tolerances in materials limiting photovoltaic technologies for indirect conversion pathways. Investigations involved calculation of the absorption and material interaction of higher specific activity radionuclides (reviewing multiple sources), device structures holding promise of better collection efficiencies, review of collection arrangements, and potential benefits obtained by varying semiconductor device band gaps.

1.2.2 Background

This research objective evolved from the dramatically expanding nanotechnology area. Ultra-small geometry devices, sensors and applications have been created, but they lack an equally scaled power source suitable for sustained operation over extended time periods. Radioisotope batteries are known to have higher power densities and longer life than conventional chemical batteries. However, their development preceded the current nanotechnology revolution. The basic principles of nuclear power based batteries remain, but their application to provide power for nano-scale technology presents a new challenge that is evolving as nanoscale discoveries provide insights into novel battery designs.

1.2.3 Approach

UF directed its research experience in radiation hardening and simulation/calculation capabilities to discover novel approaches leading to the development of a nano-scale radioisotope MEMS battery. The application of radioisotope knowledge in MEMS dimensions requires improvement and essential modification of current radioisotope battery design. One beneficial area realized with development of wide bandgap semiconductor was energy converters capable of utilizing higher specific activity radionuclides and a broader part of the photon spectrum in indirect conversion . The resultant energy density increase offers additional progress in nano-scale battery technology made possible with batteries immune to radiation induced defects from alpha, beta and gamma energy sources. High radiation tolerance will promote use of both direct and indirect conversion methodologies, and make possible development of longer-life and higher conversion efficiency batteries.

1.2.4 Quarterly Benchmarks

Q1: Perform cobalt irradiation evaluations on new devices fabricated in III-V and II-VI semiconductors

Q2: Research technology of new radiation conversion developments

Q3: Design test methods for fundamental nano-scale battery design principles (cathodoluminescence, etc.)

Q4: Provide summary report

1.2.5 Discussion and Results

The UF ^{60}Co irradiation facility, with full automated instrumentation and experimental control, has conducted material and device studies during the last year involving:

- Irradiation studies of special III-V devices
- Irradiation studies of state-of-the-art II-VI devices
- Fundamental properties of nano-scale battery designs
- Ongoing irradiation studies of $CuInGaSe_2$
- Investigation of luminescent and phosphorescent materials
- Future studies of high and ultra-low dielectrics

1.2.5.1 Irradiation Studies of Special III-V Devices

Important information on radiation tolerance and scalability to nanometer dimensions has been realized with gamma ray irradiations of AlGaAs/GaAs Quantum Dot Lasers and InGaN Quantum Well devices studies (these devices have been donated by UCF) shown in Figure 1.2.5.1a & b and a cross-sectional view of the quantum dot lasers in Figure 1.2.5.2. The crystalline structure of the InGaN devices where fabricated such that the zinc-blende GaN parameters are taken equal to the wurtzite GaN parameters.

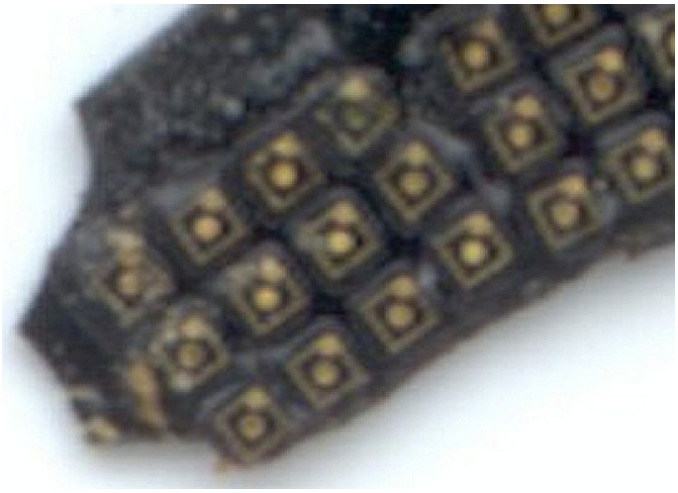

Figure 1.2.5.1a – Photographs of InGaN Quantum Well Devices

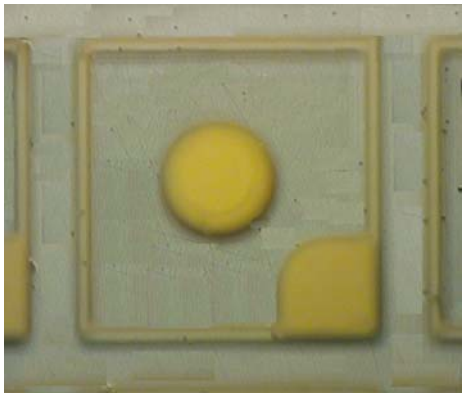

Figure 1.2.5.1b – Closeup of InGaN Quantum Well Device

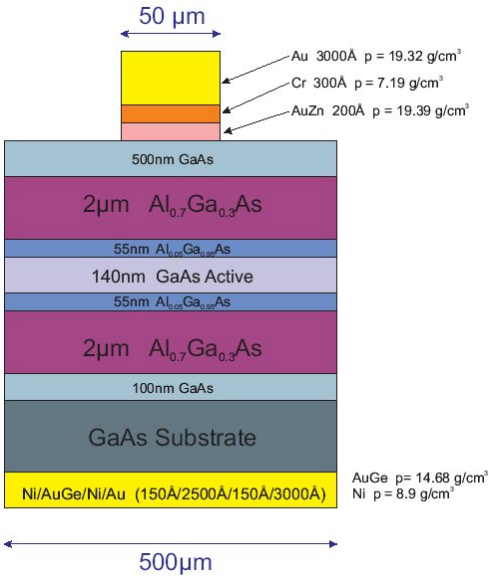

Figure 1.2.5.2 Typical Quantum Dot Laser Cross-Section Structure

Part of the UF focus has been on compounds derived from the column III-V family of elements. These compounds are permutations of the column III elements Al, Ga and In and the column V elements N, P, As and Sb. They are characterized by their excellent optoelectronic (efficient light emission and absorption) and electronic (high carrier mobilities) properties. These properties are essential for efficient indirect conversion in nanoscale radioisotope batteries. The band-gap engineering capabilities of these compounds makes possible tandem stacked configurations for improved conversion efficiency of photoluminescent systems. Each band-gap is designed to convert a portion of the photon spectrum. The first cell is designed to favor the UV part of the spectrum (short wavelength), and the last cell absorbs longer wavelengths in the near infrared. This stacked device architecture seeks a match of device absorption and transmission properties with the actual spectrum of the photon emitting phosphor.

1.2.5.2 Irradiation Studies of State-Of-The-Art II-VI Devices

ZnO devices used in radiation tolerance testing (shown in Figure 1.2.5.2.1) are totally transparent. The transparent SnO contacts are partially visible in this photograph because the light source is at an angle on the ZnO devices where thin-film interference colors are created. These colors are similar to the colors we observe with soap bubbles. The energy gap ranges from a very wide value to a very narrow or even negative value. All II-VI binary

semiconductors have direct band-gaps and are good candidates for photo-voltaic indirect radioisotope energy converters using phosphors and photoluminescent materials.

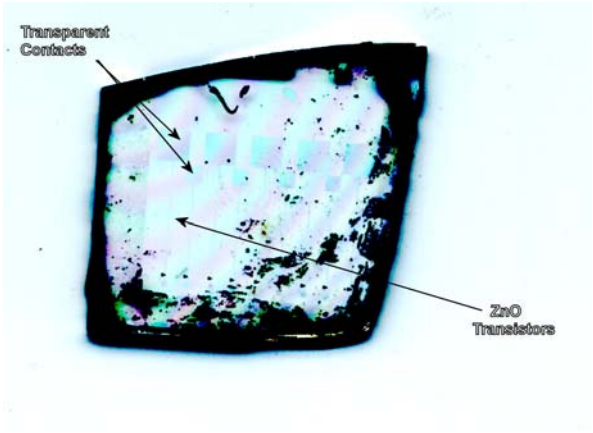

Figure 1.2.5.2.1 – Transparent ZnO Photo-Voltaic Devices

The main challenger for II-VI materials is the difficulty in forming n-type and p-type contacts to II-VI semiconductors on the same substrate. It is also quite difficult to form good ohmic contacts. Usually the optimum contact resistance is a sharp function of the process temperature, and this remains an active area of research for ZnO p-type contacts. The literature reports successful N-type contacts on ZnO Schottky diodes. Irradiation studies have been completed on some p-type ohmic contacts on ZnO. Additional measurements being planned should result in a publication of this work.

1.2.5.3 Fundamental Properties of Nano-Scale Battery Designs

Research into nano-scale radioisotope batteries is aided by general trends in the consumer electronics industry. These include the reduced scaling of device physical dimensions, increased levels of integration (more devices per chip) and low-voltage, low-power designs. These trends are forcing the electronics industry to adopt new materials, device designs, circuit topologies and processing technologies. Emerging changes include deep submicron device dimensions (<45nm), new hi-K as well as low-K dielectrics, copper chip level interconnects, multi-gated transistors and biaxially strained SiGe on silicon. These changes continue to introduce many novel and potential design pathways for higher efficiency radioisotope energy converters designed for MEMS applications.

Nanodevices include those with nanometer-scale gates and air-bridged point contacts, and those with three-dimensional nanometer-scale features, such as photonic lattices. They also

include those, such as quantum dots, that can be used to investigate solid-state physics phenomena based on tunneling and low dimensionality. The long-range goal for these efforts seeks ultra-small and ultra-low-power devices that operate with only a few electrons per device (MEMS).

Principal UF interests are the impacts of radiation exposure on the key industry trends and changes described above: reduced device dimensions (< 0.10 μm); new low-K and high-K dielectric materials; high Z interconnect and contact materials (Cu, W); more radiation resistant III-V and II-VI semiconductors; strained SiGe-Si structures and devices. Pursuit of both direct and indirect energy conversion is UF's major concern. Other related trend issues may be addressed, but these are key to this topic. Next generation or generation-after-next electronics devices are projected to incorporate dielectric and semiconductor layers consisting of only a few atomic layers in one or more dimensions. The attendant fluctuations in the parameters used to characterize radiation effects must be simulated, understood and incorporated into device design tools. Atomic-scale physical modeling is required for this task. These reduced dimensional devices (especially the metastable strained SiGe-Si system) will be forced into a new equilibrium if excessive energy (such as radiation induced heat and ionizing radiation) is introduced. The resulting interaction with the ultra-thin structure of nano-scale energy conversion devices may result in threading dislocations or higher bulk and interface defect densities that adversely affect converter efficiency. First principles physics calculations of these effects (ideally three dimensional) need to be coupled with the study of designs that would mitigate or eliminate such degradations. Experimental verification of the key features of proposed nano-scale radioisotope battery models is necessary. Ideally, the radiation impacts to be studied should include both ionizing total dose and single event effects.

The UF team has clarified a number of important parameters governing the general principles affecting nano-scale radioisotope energy conversion. Monte Carlo and EGSnrc calculations have investigated the key relationships in radioisotope source design. The roles of self-absorption, planar geometric area versus edge loses, and specific activity are all inter-related and must be optimized for each prototype nano-scale radioisotope energy converter. Ignoring actual simulated output power, it is evident that energy converters fabricated by conventional planar semiconductor technology must be > 2μm by 2μm, while dimensions normal to that plane may be nano-scale.

The literature reports a number of radioisotope battery models with power capabilities of ~ 1μW/cm^2. Designs based on direct radioisotope energy conversion mechanisms must benefit from stacked architectures to increase power by series combination of multiple conversion devices. The increased output voltage must be coupled with designs that adjust each stacked converter for the same output current (previously reported). This was simulated by Monte Carlo calculations, and is possible with current technology. A second concept reported in the literature utilized nanopores to increase the device surface area (an extension of v-groove trenching or nanotexturing concepts). Although a patent has been issued for this nanopore idea in GaP, it is unlikely to develop sufficiently to be available within the time window of this research.

Indirect radioisotope energy conversion pathways promise improved conversion efficiency with recent designs for photovoltaic converters boasting efficiencies >60%. The UF team has examined the latest advances in this area. UF's approach to novel converter designs are based on indirect conversion mechanisms involving long-range high risk research. These endeavors currently fall outside the scope of conventional development threads. UF's work has explored the role of transparent II-VI materials for improved power output potential. High risk areas associated with this work rely of future development of electrical contacts, interconnections and radiation resistant phosphor/photoluminescent materials. Recent developments are providing important advances leading to successful development of an ultra-small radioisotope energy converter for MEMS devices based on UF's novel ideas. The future development of a working nano-scale radioisotope energy converter will ultimately reflect reduce power requirements and progress in MEMS.

1.2.5.4 Ongoing Irradiation Studies of $CuInGaSe_2$

UF research that is focused on nanoscale radioisotope battery technology is currently testing CuInGaSe2 photovoltaic cells (see Figure 1.2.5.1) for radiation induced effects during indirect conversion. These photovoltaic devices are an active development area for a suitable converter to the longer wavelengths (>1μm) above the visible spectrum. UF is evaluating the indirect conversion efficiency of these devices using a phosphor stimulated by a radioisotope source. It is expected that these photovoltaic devices may be radiation tolerant and are good candidates for converting emissions to power using a number of newer phosphor/fluorescent materials.

Early results have determined that these PV cells exhibit an improvement in conversion efficiency after several MRads(Si) of gamma ray irradiation from ^{60}Co. While this particular device is not nearly as radiation tolerant as many of the III-V and II-VI semiconductors, the tested level still is higher than the normal radiation exposure experience by satellite systems.

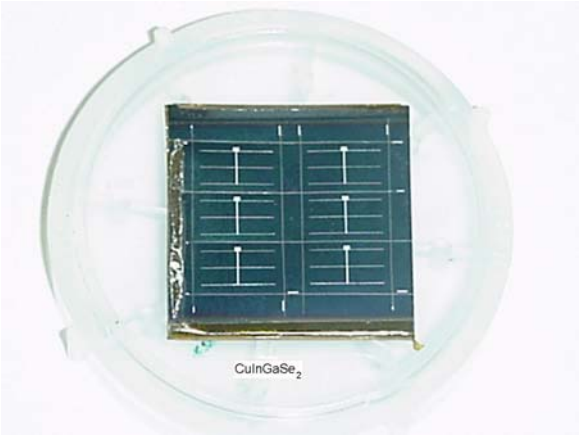

Figure 1.2.5.1 – Array of Six $CuInGaSe_2$ Photovoltaic Cells

Much interest has been expressed in these ternary I<B>-III-VI(2), group semiconductors for use in electro-optical devices such as photovoltaic cells. Subsets of these, AgInS(2),AgInSe(2),CuInS(2) and CuInSe(2) have been combined to form the pentenary alloy system Cu(1-y)Ag(y)InS(2(1-x))Se(2x). This pentenary alloy allows band gap variation while keeping the lattice constant fixed. Samples are prepared by reacting stoichiometric powder mixtures at about 900°C. X-ray diffractometry tests suggests the alloys maintain complete solid solubility throughout the system in a chalcopyrite- type crystal structure. Band-gap energies have been estimated at 300°K using cathodoluminescence studies on pressed bars of these powders. These tests suggest that the alloys are all direct- band-gap semiconductors. A list (below) of the energy gaps versus their composition demonstrates the potential of band-gap engineering for photovoltaic conversion cells.

- $CuInSe_2$ (Eg = 1.04 eV)
- $CuIn_{0.7}Ga_{0.3}Se_2$ (Eg = 1.14 eV)
- $CuInS_2$ (Eg ≈ 1.50 eV)
- $CuGaSe_2$ (Eg = 1.68 eV)

This system has two advantages for near infrared conversion. A combination of these in a stacked cell arrangement can absorb a broad spectrum from a phosphor or photoluminescent emitter, while the direct band-gap is free from phonon generated heat pathways (momentum energy component) of indirect band-gap materials..

1.2.5.5 Investigation of Luminescent and Phosphorescent Materials

The major categories of photon emitting materials are:

DEF.: Luminescence is generally the transition of a higher energy electron to some lower state with the emission of a photon of light.

NAME	PROCESS
• Fluorescence	nanosecond time frame
• Phosphorescence	microsecond to millisecond time frame
• After glow	seconds
• Photoluminescence	incident high-energy photon creates emission of lower energy photon
• Cathodoluminescence	high energy electron (β^-) causes emission of photon

Common phosphorescent materials include:

- ZnS – metal sulfides
- Tungstates
- Oxides
- Many organic compounds

UF's technical task plan for the coming year will be concentrating on this technology and examining best candidates.

1.2.5.6 Future Studies of High And Ultra-Low Dielectrics

Cu/ultra-low dielectric and high dielectric developments are active industrial topics promoting progress in nano-scale applications. These technologies seek improvements in ultra-thin layer uniformity (pin holes/voids), stability over temperature changes induced during fabrication, and reduction of interactions with surrounding atoms in new materials. UF planned tasks during the next phase of UF's work will investigate, and where possible, test candidate

materials with prototype nano-scale radioisotope energy converter materials (ZnO, GaN, etc.). Electrical characterization and identification of induced changes from ionizing radioisotope energy will be studied.

1.2.5.7 References

- Homes,Vogt, Shapiro, Wakimoto, Subramanian, and Ramirez, "*Charge transfer in the high dielectric constant materials CaCu3Ti4O12 and CdCu3Ti4O12*', Physical Review B 67, 092106,(2003).
- Brenton Burnett, "*The Basic Physics and Design of III-V Multijunction Solar Cells*',NREL III-V Report, NREL III-V Project Report,12, Aug. 2002.
- Huang, L. Aucoin and S. Shanfield, "*Hot-Electron-Induced Degradation of Metal-Semiconductor Field Effect Transistors,*" Proc. of IEEE GaAs IC Symp., pp. 259-262, (1994).
- M. Fukuda, "*Reliability and Degradation of Semiconductor Lasers and LEDs*," Artech House: Boston, London, 1991.
- B. G. Rax, C. I. Lee, A. H. Johnston and C. E. Barnes, "*Total Dose and Proton Damage in Optocouplers,*" IEEE Trans. Nucl. Sci., **43**(6), pp. 3167-3174 (1996).
- S. C. Lee, Y. F. Zao, R D. Schrimpf, M. A. Neifield and K. F. Galloway, "*Comparison of Lifetime and Threshold Current Damage Factors for Multi-Quantum-Well GaAs/AlGaAs Laser Diodes,*" IEEE Trans. Nucl. Sci., **46**(6), pp. 1797-1804 (1999).

2.1 Visualization for Quality Assurance of MEMS Micro-Assemblies

2.1.1 Two Complimentary MEMS Approaches

Tasks related to the advanced visualization techniques for micro electro-mechanical systems (MEMS) have proceeded throughout the year. The tasks are proceeding along two complimentary approaches that are aimed at ultimately providing optimized micro-CT techniques for the 3-D visualization of advanced MEMS structures. Area 1 focuses on the development of simulation tools that can be used to optimize the parameters for micro-CT visualization of MEMS devices. Area 2 focuses on the empirical development and demonstration of radioGraph 2.1.ic and micro-CT techniques for the visualization of MEMS devices. The current year's efforts focused primarily on Area 1, Visualization Simulation.

2.1.2 Background

This project evolved from a previous project area that was aimed at the visualization of hazards and activities in radiation environments. The new direction extends existing visualization techniques, and explores new techniques, to provide detailed 3-D visualization of MEMS Micro-assemblies. The project capitalizes on expertise developed to address issues dealing with the latest generation of micro electro-mechanical systems. The extremely small physical size of MEMS presents multiple challenges for visualizing these devices without damaging sensitive surfaces and structures. This project reviews techniques that can satisfy these requirements and potentially be extended to autonomous evaluation of MEMS Micro-assemblies in a variety of packaging and environments.

2.1.3 Approach

This task will identify requirements for an integrated effort in simulation and empirical demonstration aimed at developing effective techniques for the 3-D visualization and evaluation of MEMS. The integrated approach will utilize simulation techniques to explore optimum parameters and capabilities that can be achieved utilizing advanced radioGraph 2.1.ic techniques to image MEMS. Simulations will permit the rapid exploration and development of the hardware requirements for advanced radioGraph 2.1.ic imaging techniques such as micro-CT. These will be extended to empirical studies to highlight specific device features using the 3-D visualization techniques developed.

2.1.4 Area 1: Visualization Simulation

This sub-task focuses on utilizing visualization tools that have been previously developed to investigate a wide range of imaging parameters pertinent to radioGraph 2.1.ic and micro-CT imaging of MEMS devices. These efforts are specifically focused on MEMS fabricated using LIGA (LithoGraph 2.1.y electroforming and molding) lithoGraph 2.1.y techniques.

2.1.5 Objective and Purpose

Identify requirements and specifications for the development of non-invasive imaging and visualization of MEMS micro-assemblies. The purpose of the simulation study was to determine the optimal materials and techniques for the micro-CT imaging of a MEMS (micro electrical-mechanical system) device. In order to accomplish this task, a CT reconstruction program available for the IDL programming language was used with a scale (1 pixel = 1um) image of the MEMS device (Figure 2.1.1). The device is composed of a rotating gear and sliding actuator arm, each mounted on pegs to a back-ground substrate. Four different materials were simulated in the study for the modeling of the gear and actuator arm; silver, nickel, polymethyl-methacrylate (PMMA), and Teflon. The mounting pegs and substrate were modeled as silicon for all tests. A simulated, single-slice CT reconstruction was done for each material at beam energies of 20, 30, 40, 50, and 60 keV. Contrast values were calculated for each reconstructed image in order to determine the material and energy which would provide the best image reconstruction of the device. Simulations were also run to determine the optimal settings for several reconstruction parameters including number of projection angles, filter type, kernel size, and interpolation method.

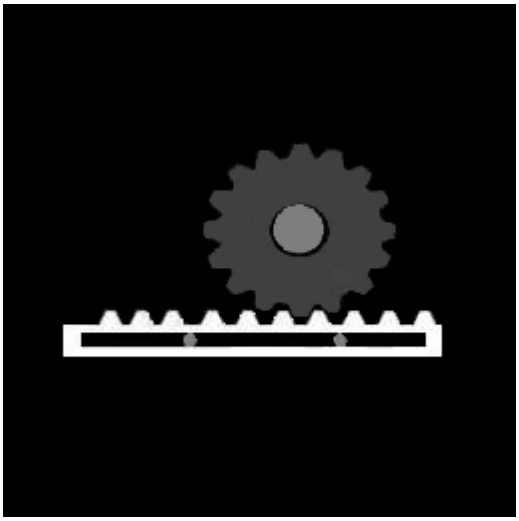

Figure 2.1.1: MEMS device

In order to simulate a single slice CT reconstruction, the scale MEMS image in Figure 2.1.1 was segmented according to pixel value, with each section being replaced by the linear attenuation coefficient of the material and energy being tested. Images were created in which the pixel values of the gear and arm were replaced with the linear attenuation values of silver, nickel, PMMA, and Teflon at beam energies of 20, 30, 40, 50, and 60 keV. Pixel values representing the posts holding the actuator arm and gear were replaced with the linear attenuation coefficient of silicon at the appropriate energy for each simulation. Pixel values for all background pixels were set to zero.

Each of the created images was run though the simulated CT reconstruction program in IDL. All simulations were initially run with 256 projection angles, and a Shepp-Logan filter with a kernel size of 17 and linear interpolation. A program was written in IDL that samples three 12x12 pixel sections of the reconstructed image; one corresponding to the center of the peg supporting the gear, one corresponding to a region towards the edge of the gear, and one corresponding to a region of the back ground just to the left of the gear (Figure 2.1.2). The mean pixel value was taken for each section as well as the standard deviation among those pixel values. A measure of the contrast-to-noise ratio was taken by subtracting the mean pixel value of the background section from that of the gear section, and then dividing by the combined standard deviation of the sections. A larger value for contrast-to-noise ratio indicates that there is a larger difference in the mean pixel values between the two sections with lower variability among the pixel values. The factors combine to indicate that the gear is more visible on the reconstructed image.

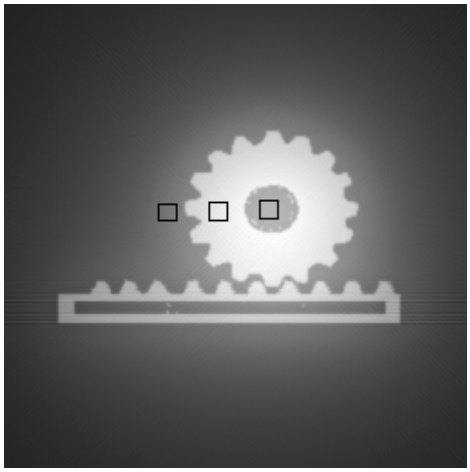

Figure 2.1.2: Three sample sections for reconstructed image

When simulating the CT reconstruction of several of the materials and energies, severe artifacts arose (Figure 2.1.3). This artifact was found in silver for all energies but 60 keV, and in nickel at 20 and 30 keV. No artifact was produced in the simulations for PMMA or Teflon. The artifact produced widely fluctuating mean pixel values in the sample sections as well as large standard deviations. It is not readily apparent if the artifact is a product of the simulation program, or if it would appear were a MEMS device made of those materials imaged in an actual micro-CT system.

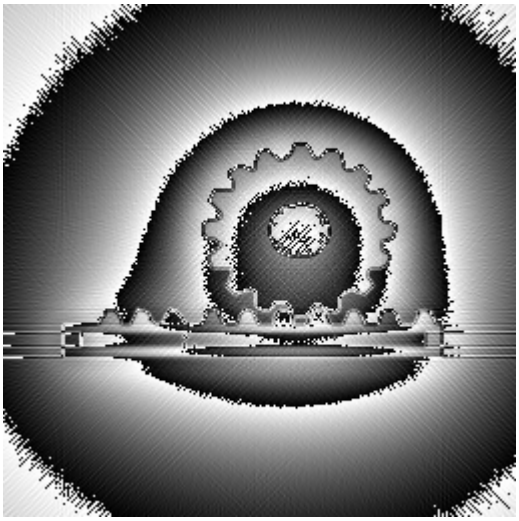

Figure 2.1.3: Reconstruction artifact (silver at 30 keV)

The contrast-to-noise ratios were plotted as a function of energy (Graph 2.1.1), but results are skewed as a result of the aforementioned artifact in the reconstruction images. The largest

contrast-to-noise value for an artifact-free image was for silver at 60 keV, followed closely by nickel at 40, 50, then 60 keV. It should be noted that the contrast values for PMMA and Teflon above 20 keV are all zero, indicating that a MEMS device constructed of these materials would be difficult or impossible to see with micro-CT imaging, without the use of very low energy beams. Based on the simulations, the best CT image reconstruction could be obtained with a MEMS device made of silver or nickel with a beam energy of around 60 keV.

Since it is not known if the artifacts would occur in an actual micro CT system, the linear attenuation values of all the materials were scaled such as to avoid artifacts in the reconstruction in order to provide a better idea of general trends in contrast for the materials. All simulations were rerun with the scaled values to produce Graph 2.1. 2. Based on these scaled simulations, the highest contrast-to-noise ratios were produced by silver at higher energies (>30 keV), while similar ratios were produced by nickel at lower energies (< 40 keV). PMMA and Teflon were zero in all instances with the scaled values. Physical testing of the materials used would be required in order to determine if the artifact would result.

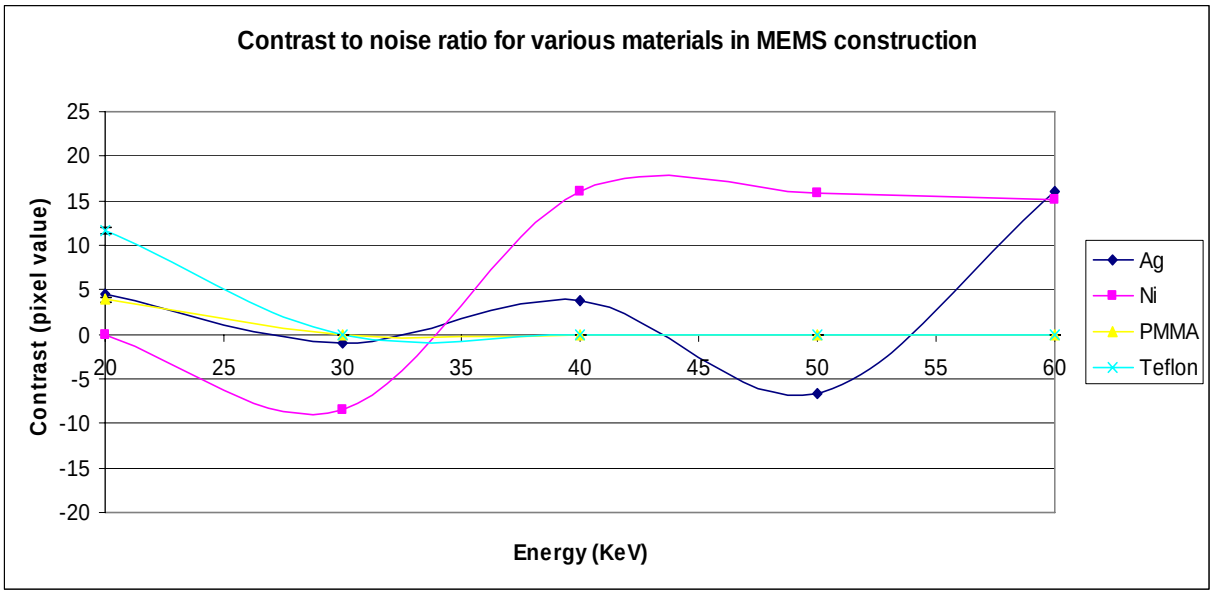

Graph 2.1. 1: Contrast to noise ratio values for materials (including reconstruction artifact)

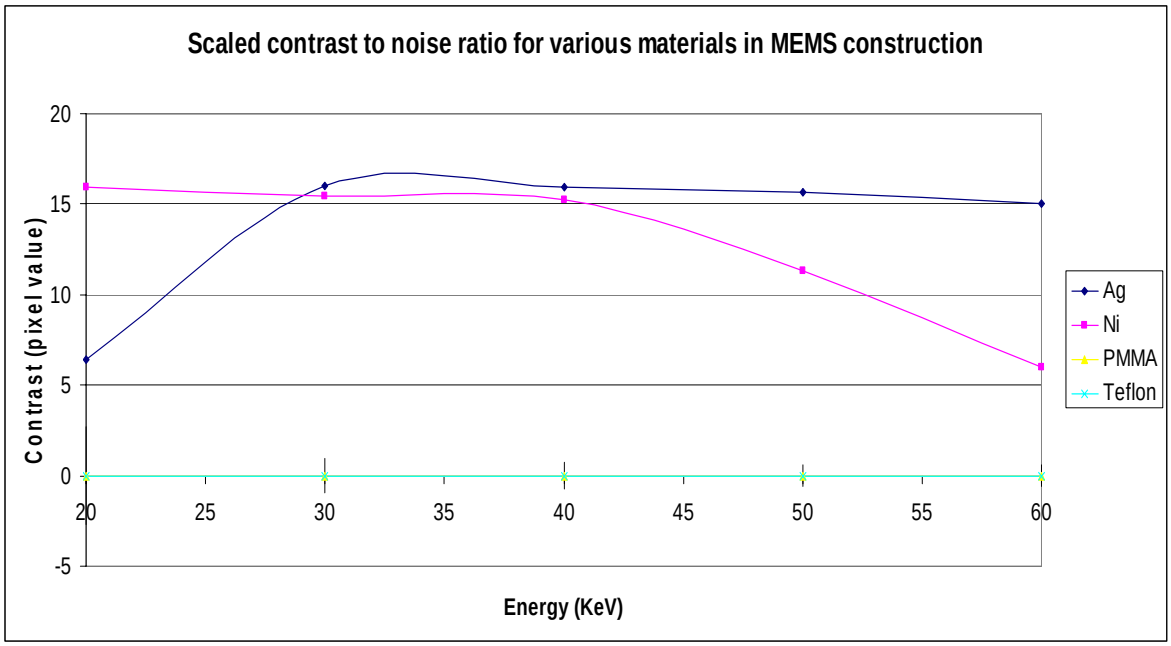

Graph 2.1. 2: Contrast to noise ratio for scaled linear attenuation coefficients to eliminate artifact

Simulations were also run for a fixed material and energy, varying the reconstruction parameters of number of projections, filter size, kernel size, and interpolation method to determine optimal settings. The same measure of contrast-to-noise ratio was used in all the simulations. Simulations were run for both silver and nickel at 30 keV in order to verify trends. Graph 2.1.s are shown below (Graph 2.1.s 3-6) to depict general trends in the reconstruction parameters. In general, the contrast-to-noise ratio increased linearly with increasing number of projection angles up to the maximum of 256 available in the simulation program. Contrast also increased in general as reconstruction kernel size increased (There was some artifact in the reconstruction of silver with a kernel size of 65). It was found that the LP Cosine and Gen-Hamming filters produced the best signal to contrast ratio. Linear and cubic interpolation methods were found to both lead to similar signal ratios, which were significantly higher than that of the nearest neighbor method.

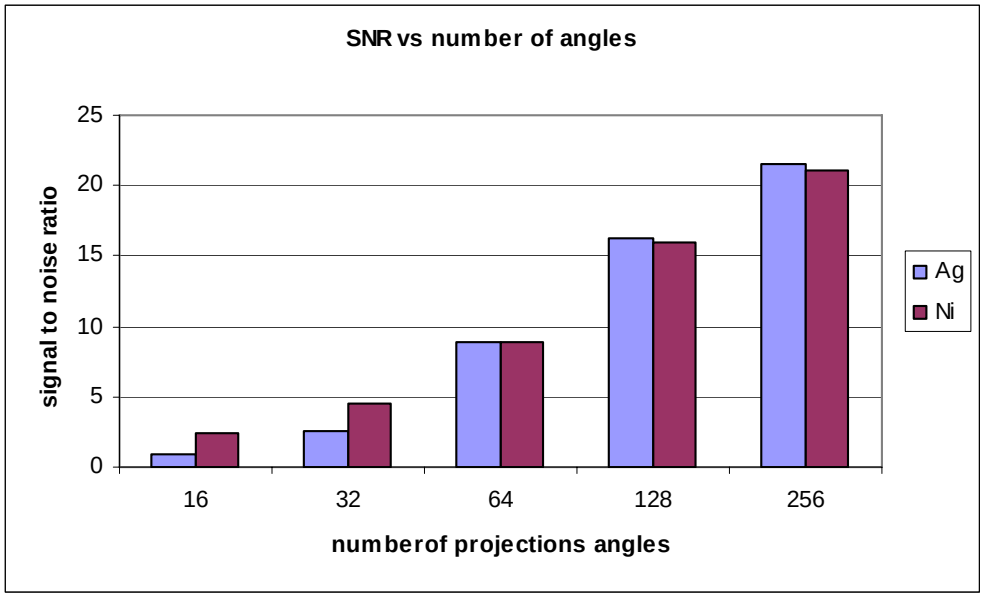

Graph 2.1. 3: Effect of number of projection angles

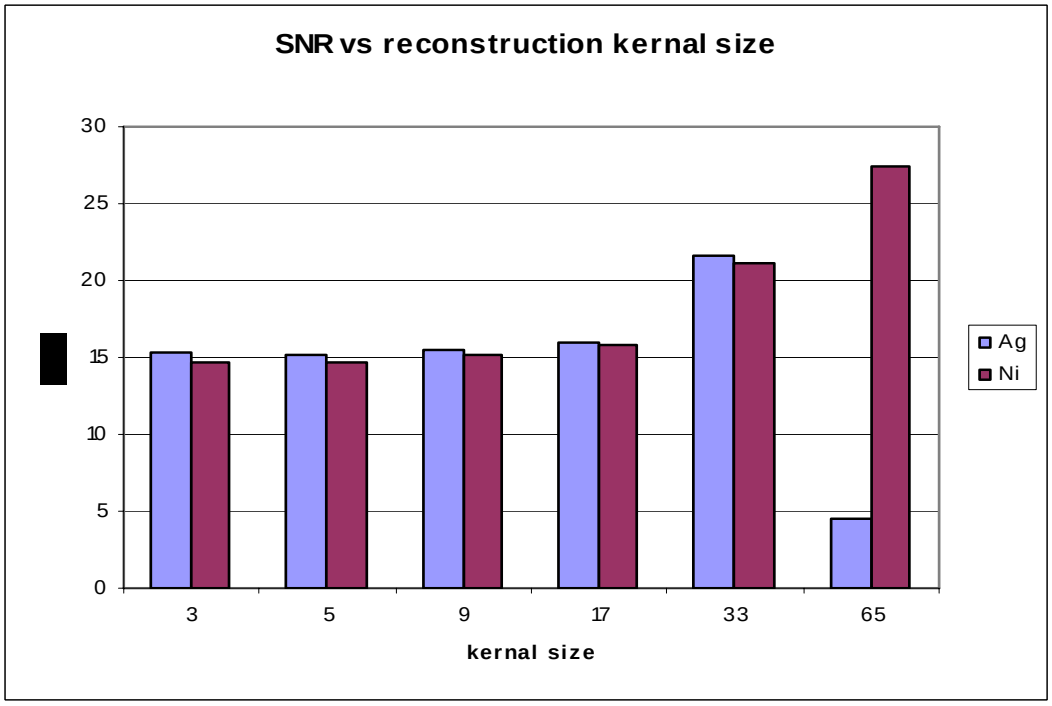

Graph 2.1. 4: Effect of kernel size

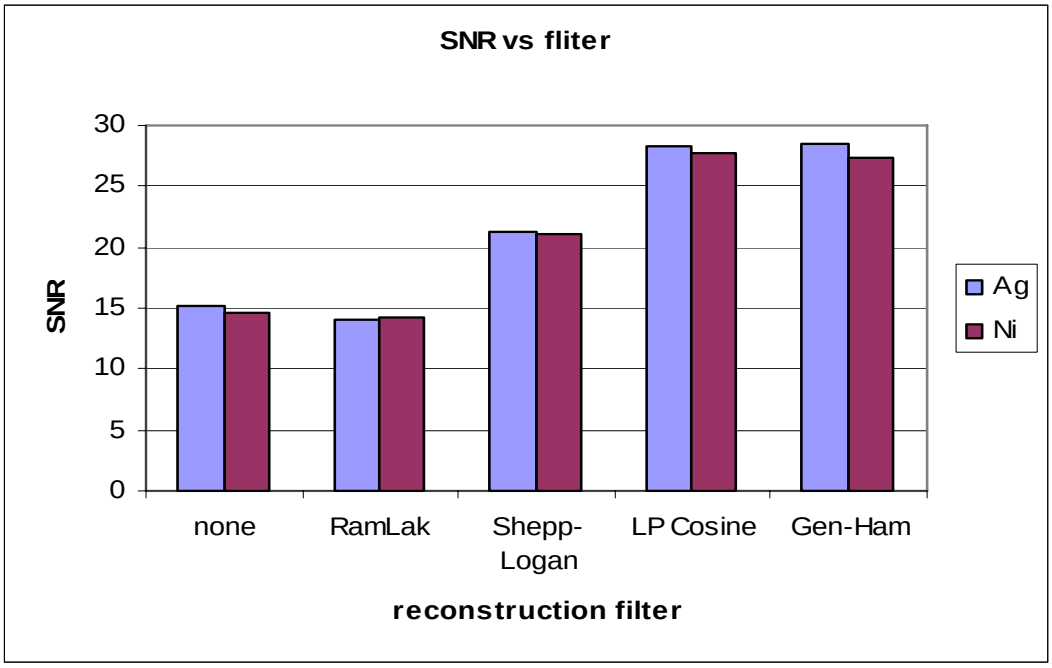

Graph 2.1. 5: Effect reconstruction filter

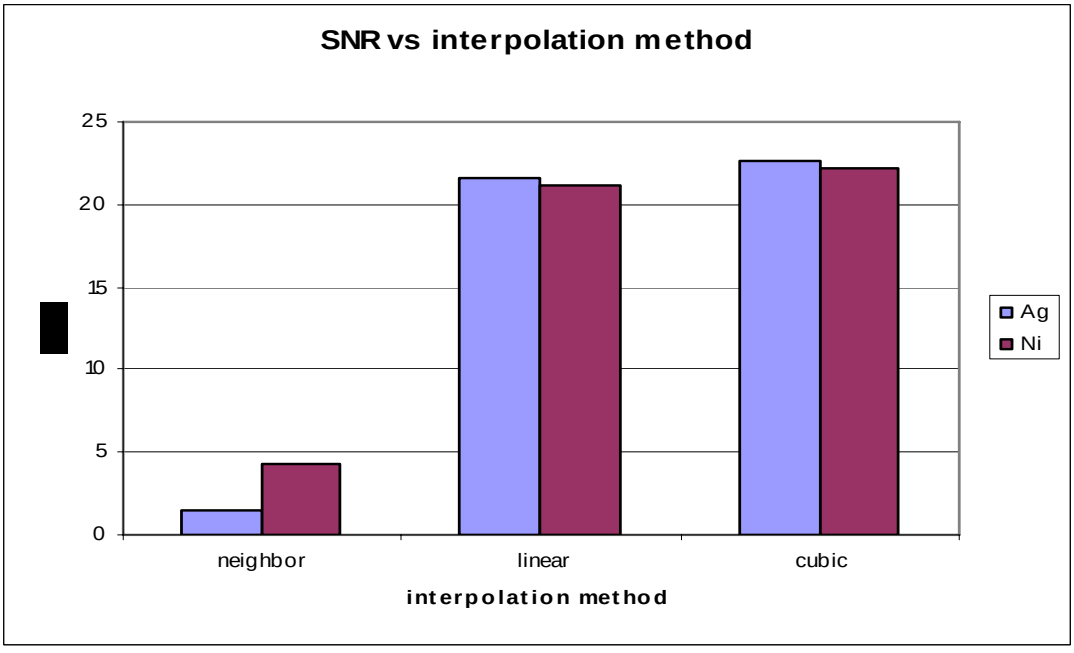

Graph 2.1. 6: Effect of interpolation method

The results obtained from this study could be used in order to guide materials selection foe MEMS device construction, as well as to aid in optimum CT imaging parameters in order to yield high contrast images. As previously mentioned, testing should be done to determine of the artifact

associated with silver and nickel imaging is a product of the simulation program or a physical property of the higher linear attenuation coefficient materials. A test for image resolution in the reconstruction images could also be beneficial in determining optimal parameters.

2.1.6 References

- Brushberg et al. "*The Essential Physics of Medical Imaging,*" Lippincott, Williams and Williams. 2002, New York pp 328-372.
- J.A. Grant et al. "*Reconstruction Strategy Suited to X-Ray Diffraction Tomography,*" J. Opt. Soc. Am. V 12, No. 2 (1995) pp 291-300.
- S. Ho, and D. Hutmacher. "*A Comparison of micro-CT with other techniques used in the characterization of Scaffolds,*" Biomaterials 27 (2006) 1362-1376.
- J. Hsieh, "*Computed Tomography: Principles, Design, Artifacts, and Recent Advances,*" Bellingham, WA: SPIE, 2003, pp79-81.
- Kak and M. Slaney, "*Principles of Computerized Tomographic Imaging,*" Institute of Electrical and Electronic Engineers, New York, 1987.
- Y. Wei, et. al. "*Relationship Between the Filtered Back projection Algorithm and the Back projection Algorithm in CT,*" IEEE Signal Processing Letters v.12 no. 9 (September 2005) p. 633-6
- Y. Wei, G. Wang, and J. Hsieh, "*An intuitive discussion on the ideal ramp filter in computed tomography (I),*" Comput. Math. Appl., vol. 49, pp. 731–740, Apr. 2005.

3. Operator/Machine/Environment Interaction

3.0 Feasibility Study of a Tensegrity-Based MEMS Device

3.0.1 Abstract

This research addresses preliminary considerations for the device of a MEMS device in three-dimensions based on a particular kind of elastic systems known as tensegrity structures. The device is a novel idea to create spatial micromechanisms, using conventional micromachining techniques. The device offers several potential applications as well as poses research challenging problems.

3.0.2 Goals

Three-dimensional devices have the potential capabilities to perform complex tasks but current micromachining techniques impose limitations that make very difficult to create them at the micro level. It is desirable to find different approaches that permit to take advantage of the current techniques and at the same time create more complex geometries. In order to achieve this goal it is necessary to explore material properties and how to implement them, instead of just to resemble macrolevel approaches at the MEMS level. Such kind of alternatives would provide new concepts for the creation of microdevices in the near future.

3.0.3 Brief Description of the Solution

This research focuses on the feasibility to generate three-dimensional devices at the MEMS level using a special kind of elastic systems known as tensegrity structures. Basically the device proposed here consists on three separated curved beams but connected with elastic ties in such a way that they might to pop up the plane and be located in different positions in the three-dimensional space.

The main goal is to find what kind of geometries are suitable for this purpose and to show that they can be achieved using conventional micromachining techniques. Very important issues like those related to detailed design of components and the derivation of the mathematical model that describes the behavior of the device are beyond the scope of this work and they will be addressed in a further step. The device proposed here is completely new and it has wide possibilities of applications.

3.0.4 Background

Since manufacturing techniques used at the MEMS level are confined to work at the plane they are very limited to create 3D structures. Instead to try to replicate processes from the macroworld it is suggestive to explore different alternatives. Planar mechanisms based on compliant links have been used successfully at the microlevel. They suggest that flexible elements might offer advantages. There are many kind of elastic systems among them are tensegrity structures.

Tensegrity structures were discovered by architects at the middle of the last century. At the macroworld there exist some devices based on their properties but never before they have been proposed for applications at the microlevel.

The word tensegrity is a contraction of tension and integrity and refers to structures that maintain their shape due only to their configuration. General speaking there are two kinds of these structures, prismatic, spherical shells, and it is possible to find several alternatives for each kind. In all cases the only elements present are struts and ties. Struts do not touch one another and they do not require external forces to maintain their unloaded position. Figure 3.0.3.1 shows a prismatic tensegrity structure.

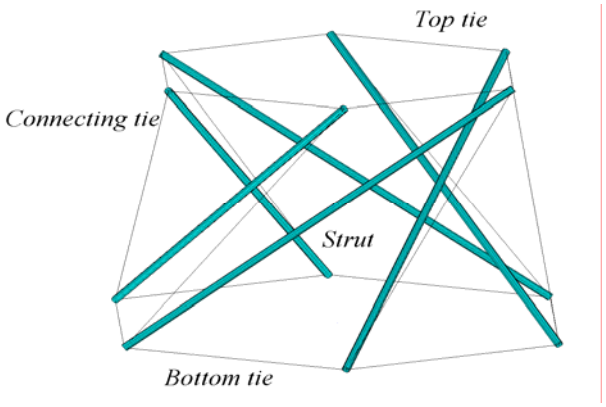

Figure 3.0.1. Prismatic tensegrity structure with 6 struts, [1].

If the lower end of the strut is constrained to remain on the plane and the motion about its axis is neglected each strut has 4 degrees of freedom and can be modeled as a universal joint that in addition to its two rotational motions, is able to move on the plane, Figure 3.0.2.

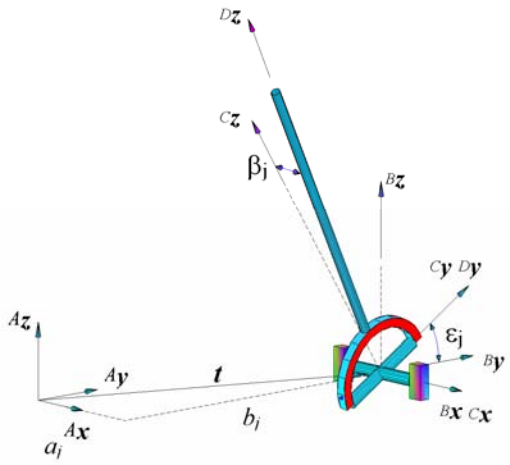

Figure 3.0.2. Strut modeled with a universal joint, [1].

Modeling all the struts with universal joints and then applying the principle of virtual work permit to establish the equilibrium position of the structure when an external force is applied Figure 3.0.3. The resultant system of equations is strongly coupled due to the large number of degree of freedoms and requires numerical techniques for its solution.

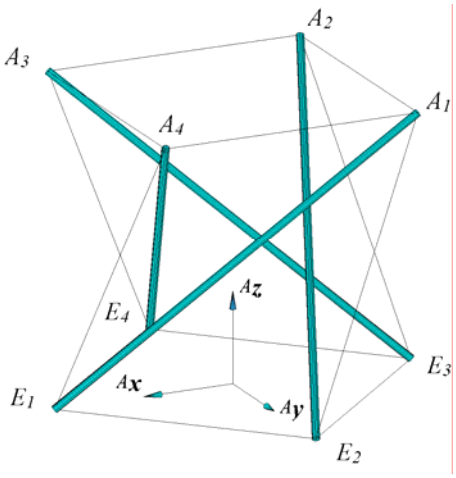

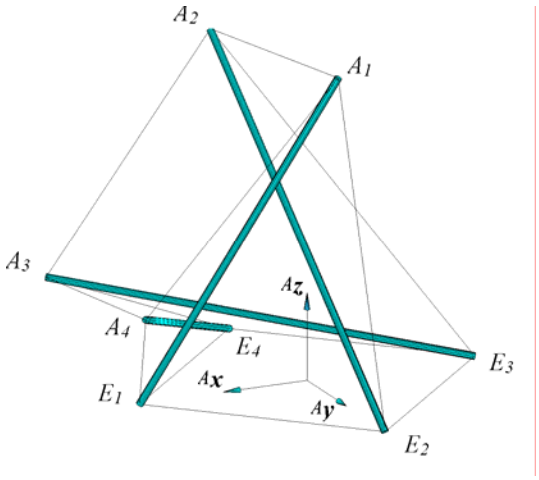

Figure 3.0.3. Unloaded and final equilibrium position of a structure subjected to external loads and constraints, [1].

One remarkable property of tensegrity structures is that they are self-deployable. This fact would permit to create the structure at the planar level and then jump to the 3D space. Figure 3.0.4 illustrates this idea. Lower ends of a prismatic structure were constrained by universal joints fixed to the plane. Struts are parallel to the substrate and the system remains in equilibrium due to the tension generated for some of its ties. When a small force in the upper direction is applied, the system pops up in a suddenly and chaotic movement to reach another equilibrium position but this time a 3D structure has been created. This concept shows the possibilities of tensegrity and it will be developed in more detail.

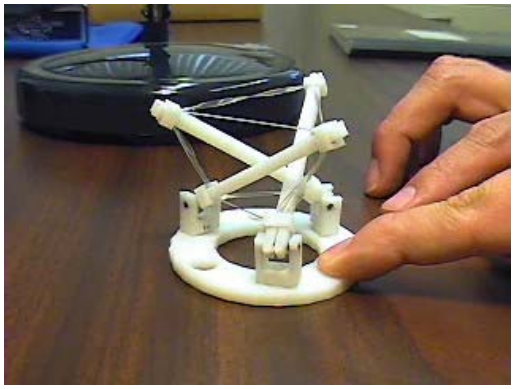

Figure 3.0.4. Tensegrity-based device concept

3.0.5 Literature Review

MEMS devices are basically planar devices. This is due the current manufacturing techniques are derived from IC industry and because to create 3D structures is very difficult. Therefore most of the motion of MEMS devices is constrained to the plane like the shown in Figure 3.0.5, where all moving parts remain on the plane.

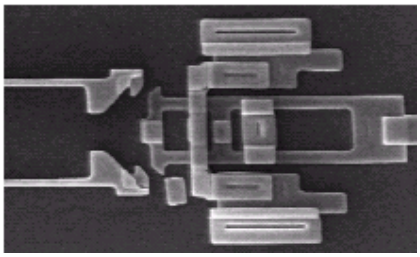

Figure 3.0.5. Typical planar mechanism, [2].

To obtain out-of-plane motion is a challenging problem and current solutions are based on two kinds of approaches.

One of the approaches is to take advantage of the deformation of materials due to shape memory or electrothermal properties. Figure 3.0.6 shows motion obtained based on shape memory alloys.

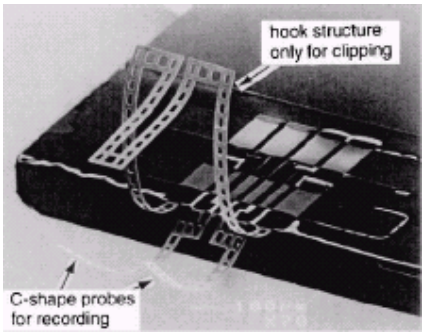

Figure 3.0.6. Motion obtained with a shape memory alloy, [3].

The second alternative is the combination of planar mechanisms in such a way that generate motion in three dimensional spaces like in Figure 3.0.7.

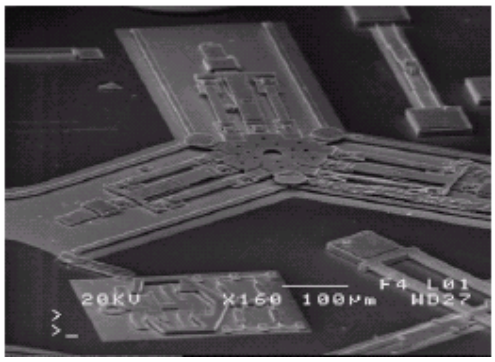

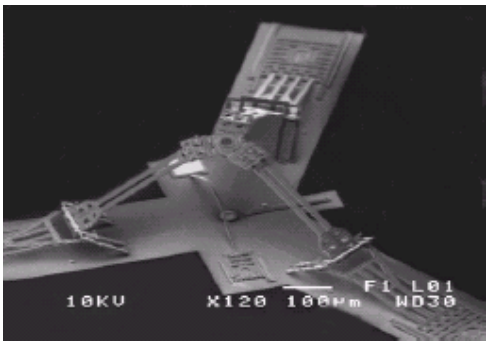

Figure 3.0.7. Particular combination of planar mechanisms makes the platform to move in the vertical direction, [4].

When the deflection of a beam is used to generate out of plane motion the resultant motion is very simple just go up and go down. If complex paths were required for the hook of Figure 3.0.6 it would not possible to accomplish them using this simple motion. In addition shape memories alloys requires training that might be cumbersome and difficult to implement. On the other hand, mechanism like the presented in Figure 3.0.7 may increase the payload because they

are working in parallel, however motion is basically in the vertical axis and the size of the device seems to be very large just to provide motion to the small platform at the center of the system.

So far no attempts to create a microdevice using tensegrity principles have been reported in the literature. This aspect makes the proposal more interesting because it will be the first time that this technique is implemented at the microlevel.

3.0.6 Design and Manufacture of the Device

It can be appreciated in Figure 3.0.4 that at the beginning of the assembly some ties must be in tension. At the macroworld that task does not require an important effort but at the microlevel is virtually impossible to grasp an elastic tie by its ends, stretched it and place it in a desired location. The task seems even more difficult if it is considered that the same sequence of operations must be applied to several ties.

Figure 3.0.8 illustrates one alternative to obtain the same result where the tie is represented by the conventional symbol for a spring. The tie is manufactured at the desired location using surface micromachining techniques and after removing the sacrificial layer the tie by itself reduces its length. This behavior is known as the shrinkage of the elastic element and usually is very small, less than 5% of the original length. For most applications it is desired that materials exhibit no shrinkage. Because of that the proposal illustrated in Figure 3.0.8 does not seem feasible to implement.

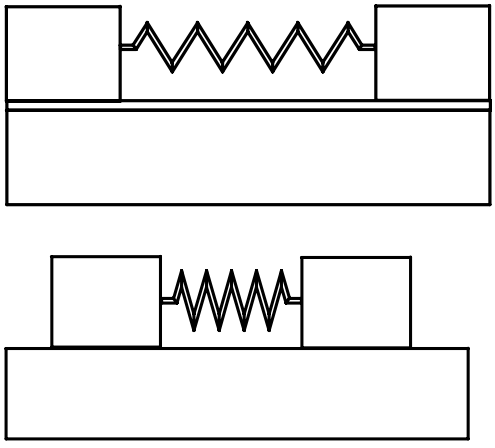

Figure 3.0.8. Representation of an elastic tie after and before releasing the parts joined by the tie.

Control of the length of the ties can be also achieved if the lengths of the struts can be altered. Alloys as Nitinol can change its lengths by about 8%. Some polymers known as electrostrictive, see Figure 3.0.9, exhibit extremely large elongation properties.

They require a voltage applied through compliant electrodes. To implement this, electrodes might be cumbersome and since they should move out of the plane. It is not clear how to achieve this goal.

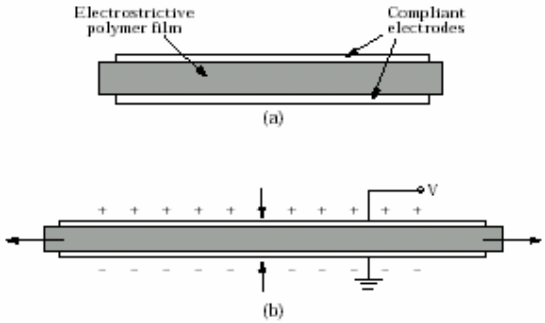

Figure 3.0.9. Electrostrictive polymers, [5].

To consider changing the lengths of the struts to control the length of the ties and in this way the position of the platform is still valid but it does not have to be linearly. If the beam is curved the same effect is achieved. Figure 3.0.10 displays a beam with an initial curved shape that is being extended in several steps.

Figure 3.0.10. Extension of a curved beam.

To obtain the behavior presented in Figure10 is easy to achieve using bimorph materials, this is to manufacture the beam with two materials with different thermal expansion coefficients. It is possible to extend and contract the beam controlling the temperature of the beam by the presence of a resistor embedded in the beam. If instead of one beam the device has three of them, its behavior is like the illustrated in Figure 3.0.11.

Figure 3.0.11. Device with 3 beams that are being extending simultaneously.

Each beam is extending one of its ends. Selecting proper distances among pivots avoid interference among the beams during the extending process.

Motion illustrated in Figure 3.0.11 is still on the plane. In order the beams go up the plane it is necessary appropriate pivots and equilibrium of forces in the space.

Universal joints like the presented in Figure 3.0.2 are ideal to permit the desired motion for each beam however they are not easy to achieve at the MEMS level. Instead of that the same motion can be obtained manufacturing a part like the shown in Figure 3.0.12.

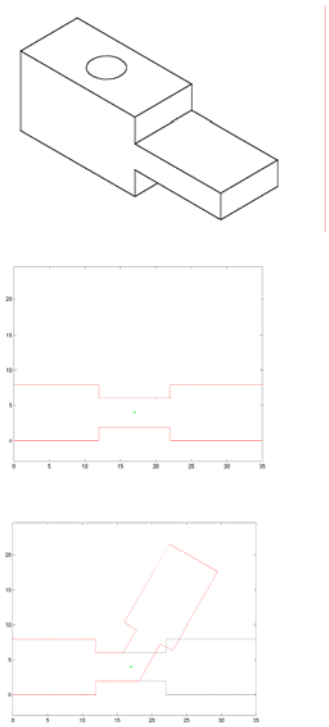

Figure 3.0.12. Revolute joint and compliant member.

The motion about an axis perpendicular to the substrate is provided by the revolute joint which is simple to manufacture using surface micromachining techniques. The motion perpendicular to the axis of the previous joint is obtained from the deformation of the slender

part as is illustrated. This is a common principle used for flexures and can be implemented considering the elastic properties of the material and the dimensions of the neck.

Figure 3.0.13 presents the structure as it is manufactured at the plane level. Bimorph beams elastic joints and ties are illustrated. Displayed shapes are intended only for illustration purposes. The whole structure can be created using basic surface micromachining techniques and conventional materials. Ties are made of silicone rubber.

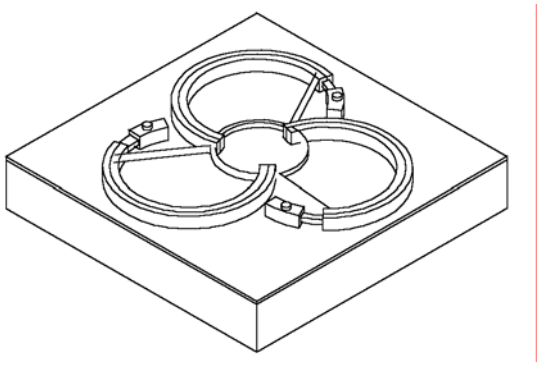

Figure 3.0.13. Device manufactured using surface micromachining.

Once the sacrificial layer is removed the beams are able to be moved by the heating of the resistor inside (connections and resistors are not shown). The curvature and therefore the distance between ends for each point can be controlled separately. Figure 3.0.14 left shows the device in its first position; this is when all its links lie on the plane. Right Figure 3.0.displays a closer view of the forces acting on the ties of the structure. To initiate the motion in the space is necessary that at least one of components of the forces presented be not parallel to the plane. If this little offset is not created just due to the deformation of the beams as a result of the stresses accumulated during the process, it will be necessary an additional device to create the initial offset. In any case this is a simple task.

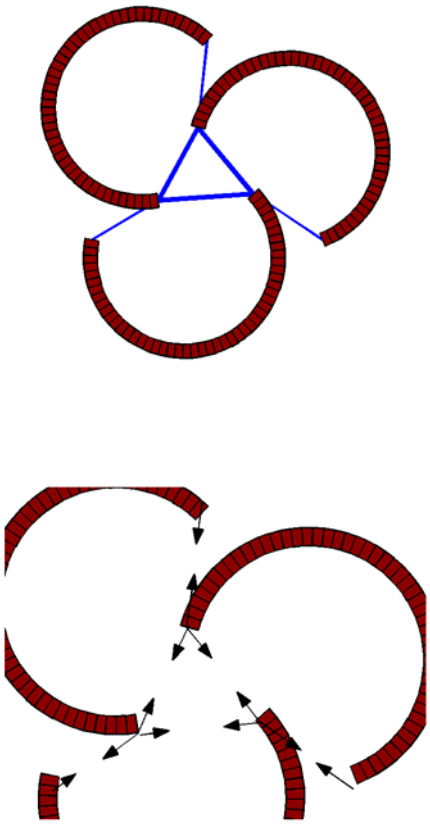

Figure 3.0.14. Initial distribution of forces on the plane.

Figure 3.0.15 shows a scheme of several positions that can be obtained just due to the change of curvature of the beams. Joints details are not presented in these schemes.

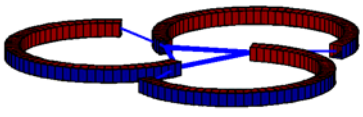

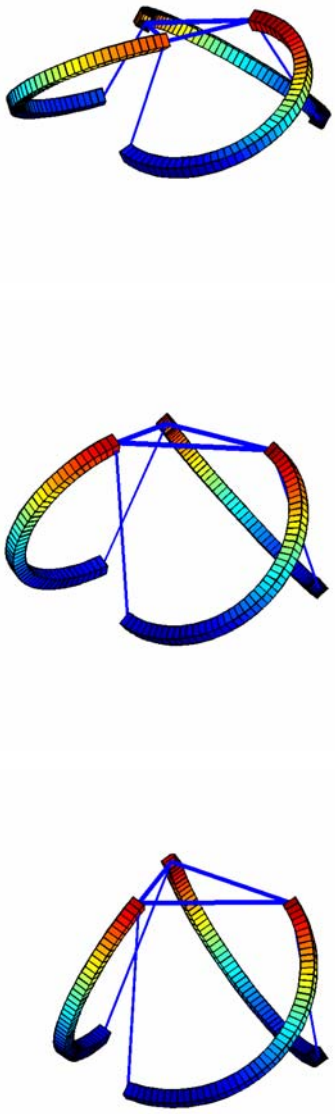

Figure 3.0.15. Several possible positions of the device.

3.0.7 Discussion

The device presented is completely feasible. It permits to generate complex paths based on simple motions and with low energy requirements in proportion to a similar device at the macrolevel.

3.0.7 Potential Applications

Potential applications for this device include:

To use it as a kind of parallel manipulator. In this way an object can be placed in any of the positions allowed inside the workspace of the mechanism.

The top platform can be designed in such a way that a mirror or a lens can be placed on it, see Figure 3.0.16, then the mirror or the lens is able to move with 6 DOF.

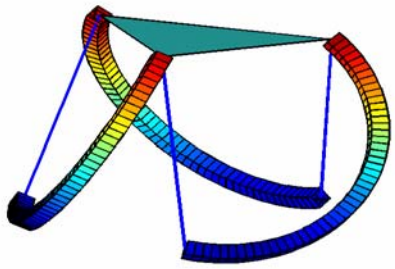

Figure 3.0.16. Device with a top platform.

The ends of the beams can be designed to act as arms of a microgripper. Again the microgripper can handle objects in 3D.

The beam presented here is not the only alternative. It is also possible to pop up the structure without using active actuators. If a passive structure is created at 3D, any force or torque applied to it will be reflected on the joints; therefore the structure could be used as a sensor of torque and force in all directions and about all the axes.

Structure can be very compliant according to the stiffness of the ties. If very low stiffness is used, the system will be able to vibrate easily. If the signals due to vibrations can be measured, a monolithic accelerometer in 3D is available.

3.0.8 Future Work

The completion of any of the ideas suggested above requires theoretical and experimental work to solve new challenging problems like the following.

It is necessary to develop a mathematical model for the forward analysis; this is to predict the equilibrium position of the device given the shape of the beams and the stiffness of the ties.

Mathematical model for the reverse analysis, with this tool it is possible to know what are the lengths of the beams to achieve a particular position of the top ends of the beams for the current material properties.

Given geometry and the materials for the beams, it is desirable to evaluate the maximum force that a beam can develop and its behavior as function of the distance between ends.

Since conventional modeling software do not include compliant elements, it is important to develop proper 3D representation of the computed results.

The shapes of the components presented here is only preliminary. It is necessary to go to the detail and to refine the design of each component.

Some of the answers require experimental research. For example answers to issues associated to the behavior of the silicone rubber as additives, curing times, evaluation of the stiffness, compatibility with other processes might be found easier by experimentation at the laboratory

3.0.9 Conclusions

The device is feasible.

The proposal is absolutely new.

It offers interesting potential applications.

It suggests challenging problems for experimental and theoretical research.

To modify the point of view of a problem may give new and better approaches to the solution.

3.0.10 References

- [1] Correa J., Duffy J., Crane C. *Static analysis of tensegrity structures*. ASME 2002 Design Engineering Technical Conferences, Montreal, Canada.
- [2] Howell L. *Two-position micro latching mechanism requiring a single actuator.* ASME 2002 Design Engineering Technical Conferences Montreal, Canada.
- [3] Fua Y., Dua H., Huanda W. *TiNi-based thin films in MEMS applications: a review*. Sensors and Actuators A, 112 (2004), 395–408.
- [4] Jensen K., Howell L., Lusk K. *Force relationships for and XYZ micromanipulator with three translational degrees of freedom.* ASME 2004 Design Engineering Technical Conferences, Salt Lake City, Utah, USA.
- [5] Heydt, R., Kornbluh, R., Pelrine R., Mason, V. *Design and performance of an electrostrictive-polymer-film acoustic actuator*. Journal of Sound and Vibration (1998), 215(2), 297-311, Academic Press.

3.2a Passive Force Control Mechanisms and Waste Management

3.2a.1 Objective

In-contact operations are differentiated from non-contact processes due to the increased danger associated with applying forces to a hazardous object. For example, during an in-contact operation care must be taken to assure that the correct amount of force, and no more, is applied to the hazardous object. A manipulator must apply enough force to maintain a grip on an object, but not so much that the object is damaged. The objective of this research is to develop passive mechanisms that incorporate compliance in order to control contact forces.

3.2a.2 Background

It has been shown that compliance can be used to control contact forces when a manipulator comes into contact with objects in its environment. Figure 3.2a.1 shows a simple example. Here it is desired to control the contact force of a wheel as it is moved along a surface. The wheel is connected to a two degree-of-freedom manipulator by two compliant connectors (B_1C and B_2C). The question is how to move the end-effectors of the manipulator (the body containing points B_1 and B_2) so that the wheel will move along the surface with the desired contact force. This can be accomplished if the spring constants, k_1 and k_2, the associated free lengths of the springs, and the angles θ_1 and θ_2 are known. As a result, the manipulator is performing a pure position move of the end effectors to achieve position and force control of the wheel. Research here is aimed at extending the concept presented here to spatial environments.

3.2a.3 Approach:

The research is based on recent work at the University of Florida with regards to the geometric stability of parallel platform based manipulators. The passive system is designed to be used in the "wrist" of a manipulator, i.e. between the end effectors gripper and the last link of the manipulator. The device is instrumented so that the pose and force/torque applied to the top of the device (the side connected to the end effector's gripper) can be measured with respect to the base of the device (the side connected to the last link of the manipulator). Based on this information, the manipulator can be commanded to perform a pure-position move that will achieve a desired force/torque and pose state for the end effectors.

Current work is aimed at designing, fabricating, and testing a new prototype (see Figure 3.2a.2) that overcomes frictional problems that occurred with an earlier prototype device. The design has been completed and parts fabricated. Testing and documentation of the device will be completed during the first and second quarters.

3.2a.4 Content:

In the previous annual reports, the conceptual design, solid model simulation and the mechanical design are all finished, the work done after that is to finalize the prototype mechanisms and provide theoretical analysis for force/ wrench measuring and compliance force control.

3.2a.5 Stiffness analysis:

The analysis of stiffness matrix for the planar structure was presented in the previous sections. Now the spatial stiffness property will be explored. In this section, necessary concepts of projective geometry for point and line-vector are provided briefly, followed by the analysis of a spatial 3-3 octahedron and the desired special 6-6 spatial parallel manipulator.

In order to perform the analysis, it is essential to expand some of the concepts from the 2-D plane to 3-D space. In the planar case, the Cartesian coordinate for a point is defined by two dimensionless scalar values: X and Y, which are also dependent on the reference point of the selected coordinate system. In Screw theory [Cra01], homogeneous coordinates (w; x, y, z) are used to describe the location of a point and $r_i = \frac{x_i\mathbf{i} + y_i\mathbf{j} + z_i\mathbf{k}}{w_i}$ refers to the position vector from the reference point O to the point A with Cartesian coordinate (x_i, y_i, z_i). Usually it is assumed that w=1 so that the ratios of x/w, y/w, z/w are equal to x, y and z. This homogeneous coordinate system also allows for a point at infinity. When |w|=0, the point A is at infinity in the direction parallel to $(x\mathbf{i} + y\mathbf{j} + z\mathbf{k})$. For points not at infinity, w is always a non-zero value. To simplify the expressions in this work, the coordinate of a point will also be expressed as (x, y, z).

It is clear that in the planar case, the equation of a line can be expressed by three numbers L, M, and R, which are first introduced by Plücker, and are called Plücker line coordinates. In 3-D space, the ray coordinate of a line is defined by any two distinct points on the line. The

coordinate of point 1 and point 2 are $\mathbf{r}_1(x_1, y_1, z_1)$ and $\mathbf{r}_2(x_2, y_2, z_2)$ respectively. The vector S whose direction is parallel to the line could be written as:

$$\mathbf{S} = (\mathbf{r_2} - \mathbf{r_1}), \qquad (1)$$

or $$\mathbf{S} = L\mathbf{i} + M\mathbf{j} + N\mathbf{k} \qquad (2)$$

So vector S provides directional information for the line segment composed by the two points. Now consider another vector r from the reference origin to any general point (x_1, y_1, z_1) on the line, the cross product of the two vectors defines a new vector which is perpendicular to both of the vectors. This is written as

$$\mathbf{S}_{OL} = \mathbf{r} \times \mathbf{S} \ . \qquad (3)$$

The vector $\mathbf{S}_{OL}$ is the moment of the line about the origin O and is clearly origin dependent, while the vector S provides the directional information for the line. Thus the coordinate of a line is written as $\{\mathbf{S};\mathbf{S}_{OL}\}$ and this is also called the Plücker coordinates of the line. The semi-colon in the coordinates indicates that the dimensions of S and $\mathbf{S}_{OL}$ are different, i.e. S is dimensionless while S_{0L} has units of length.

From equation (3), the moment vector $\mathbf{S}_{OL}$ is:

$$\mathbf{S}_{OL} = \begin{vmatrix} \mathbf{i} & \mathbf{j} & \mathbf{k} \\ x_1 & y_1 & z_1 \\ L & M & N \end{vmatrix} = P\mathbf{i} + Q\mathbf{j} + R\mathbf{k}, \qquad (4)$$

where

$$\begin{aligned} P &= y_1 N - z_1 L \\ Q &= z_1 L - x_1 N \\ R &= x_1 M - y_1 L \end{aligned} \qquad (5)$$

The Plücker coordinates for the line joining two points with coordinates $(1; x_1, y_1, z_1)$ and $(1; x_2, y_2, z_2)$ was expressed by Grassmann by the six 2×2 determinants of the array:

$$\begin{bmatrix} 1 & x_1 & y_1 & z_1 \\ 1 & x_2 & y_2 & z_2 \end{bmatrix} \qquad (6$$

as

$$L=\begin{vmatrix}1 & x_1\\ 1 & x_2\end{vmatrix},\ M=\begin{vmatrix}1 & y_1\\ 1 & y_2\end{vmatrix},\ N=\begin{vmatrix}1 & z_1\\ 1 & z_2\end{vmatrix},\ \text{and}\ P=\begin{vmatrix}y_1 & z_1\\ y_2 & z_2\end{vmatrix}, Q=\begin{vmatrix}z_1 & x_1\\ z_2 & x_2\end{vmatrix}, P=\begin{vmatrix}x_1 & y_1\\ x_2 & y_2\end{vmatrix}$$

The Plücker line coordinates $\{\mathbf{S};\mathbf{S}_{OL}\}=\{L,M,N;P,Q,R\}$ are homogeneous since non-zero scalar multiples of all the coordinates still determine the same line [Cra01]. The semicolon inside the coordinate separates the (L, M, N) and (P, Q, R) because their dimensions are different. From equation (5.19), the direction ratios (L, M, N) are related to the distance |S| by

$$L^2+M^2+N^2=|\mathbf{S}|^2 \qquad (7)$$

It is useful to unitize these directional values of these homogeneous coordinates to simplify the application:

$$L=\frac{x_2-x_1}{|S|}, M=\frac{y_2-y_1}{|S|}, N=\frac{z_2-z_1}{|S|} \qquad (8)$$

which are also called direction cosines of the lines or unit direction ratios. Therefore, the new set of L, M, and N has the new restriction

$$L^2+M^2+N^2=1\ . \qquad (9)$$

Using the Plücker line coordinates, a force $\mathbf{f}$ is expressed as a scalar multiple $f\mathbf{S}$. The reference point is selected in such a way that the moment of the force $\mathbf{f}$ about this reference point, $\mathbf{m_0}$, can be expressed as a scalar multiple $f\mathbf{S}_{OL}$ where $\mathbf{S}_{OL}$ is the moment vector of the line. So the action of the force applied on the body can be expressed as a scalar multiple of the standard Plucker line coordinates and the coordinates of the force are:

$$\hat{w}=f\cdot\hat{\mathbf{S}}=f\{\mathbf{S};\mathbf{S}_{OL}\}=\{\mathbf{f},\mathbf{m_0}\}\ , \qquad (10)$$

where $\{\mathbf{S};\mathbf{S}_{OL}\}$ is the Plucker line coordinates and $|\mathbf{S}|=1$. It is clear that $\mathbf{f}$ is a line bound vector and coordinate independent, while the moment $\mathbf{m_0}$ is origin dependent.

For spatial parallel mechanisms, the forward static analysis consists of computing the resultant wrench $\hat{w}=\{\mathbf{f};\mathbf{m}\}$ due to linearly independent forces generated in the legs acting upon the moving platform. The resultant wrench could be simply expressed:

$$\begin{aligned}\hat{w}&=\{\mathbf{f};\mathbf{m}\}=\{\mathbf{f}_1;\mathbf{m}_{01}\}+\{\mathbf{f}_2;\mathbf{m}_{02}\}+\{\mathbf{f}_3;\mathbf{m}_{03}\}+\ldots\\ &=f_1\{S_1;S_{01}\}+f_2\{S_2;S_{02}\}+f_3\{S_3;S_{03}\}+\ldots\end{aligned}\ . \qquad (11)$$

Equation (11) may be written as

$$\hat{w} = \mathbf{j}\boldsymbol{\lambda}, \tag{12}$$

where j is the Jacobian matrix of the structure. The columns of the matrix are composed of the Plücker coordinates of the lines of the leg connector forces as

$$\mathbf{j} = \begin{bmatrix} S_1 & S_2 & S_3 & \dots \\ S_{01} & S_{02} & S_{03} & \dots \end{bmatrix}. \tag{13}$$

λ is the column vector with the scalar of the forces as its elements.

$$\lambda = \begin{bmatrix} f_1 \\ f_2 \\ f_3 \\ \dots \end{bmatrix} . \tag{14}$$

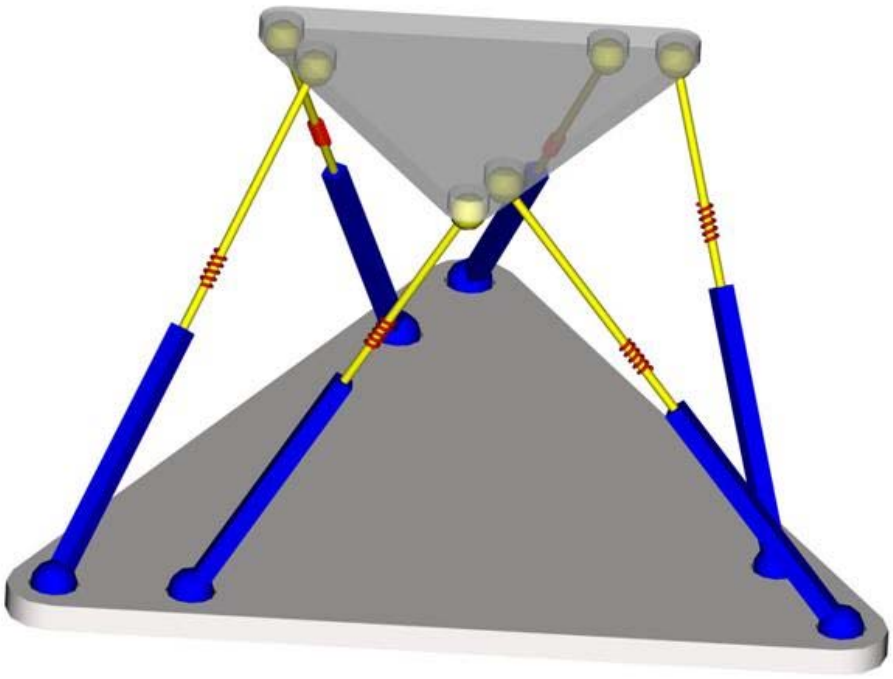

Figure 3.2a.1. 3-D Model for special 6-6 parallel mechanism

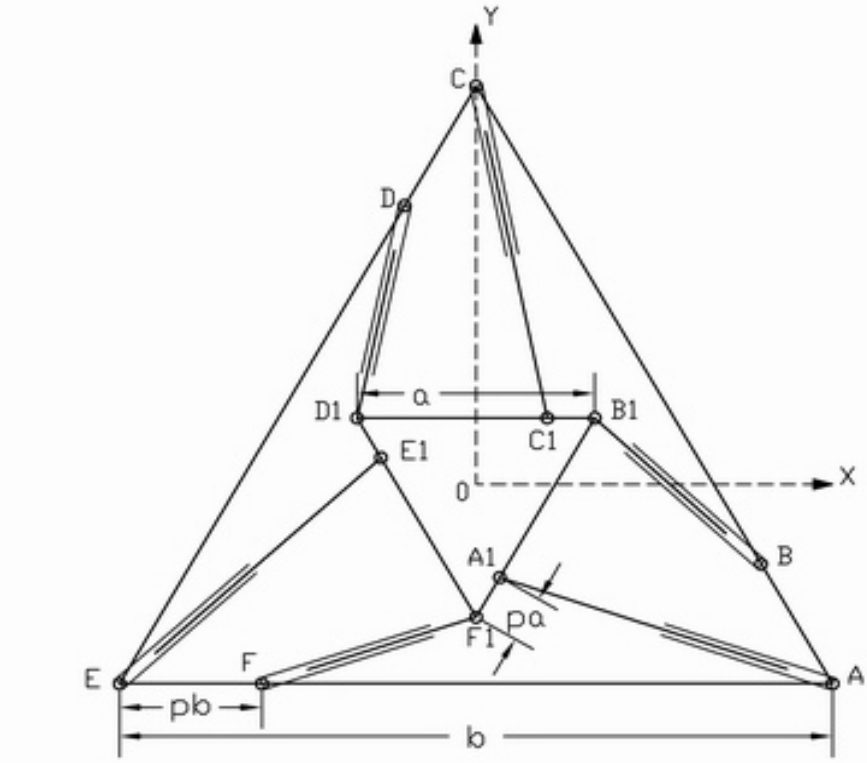

Figure 3.2a.2. Top view of the special 6-6 configuration

Now consider the proposed special 6-6 parallel passive structure, its 3-D model and plan view are shown in Figures1 and 2.

This special 6-6 spatial parallel manipulator has a moveable top platform connected to the fixed platform (ground) by six translational springs acting in-parallel. Each leg has a conventional spring as the compliant component and as acting in the prismatic joint of spherical-prismatic-spherical serial chain. The parallel manipulator with six such compliant legs as well as one top platform and one base platform thus has six degrees of freedom.

The top platform is connected to the base platform by the initially unloaded compliant coupling which restricts any relative spatial motion between the bodies. The corresponding stiffness mapping is thus a one-to-one correspondence that associates a twist describing the relative displacement between the top and base platform with the corresponding resultant wrench provided by the springs between them.

The basic shapes of the top platform and the base platform of this special configuration are equilateral triangles with the top and base triangle side lengths being a and b respectively while pa and pb are the joints separation distance between the pivots. The distance h between the geometrical center of the top platform and the geometrical center of the base platform is selected

in such a way that it is qualify the following expression based on the analysis in the previous chapters:

$$h = a = \frac{b}{2}. \tag{15}$$

The top platform has 6 spherical pivot points $A1, B1, C1, D1, E1, F1$ located along its triangle sides and the base platform has 6 spherical pivot points A, B, C, D, E, F along its triangle sides. The six springs are connected respectively and in order to simplify the process of the analysis, it is necessary to establish the geometry of the system. The following are position vectors that define the directions of the six legs and their magnitudes define the lengths of the six legs:

$$\begin{aligned} l_1 &= \left\|\overrightarrow{AA_1}\right\| = \left\|\overrightarrow{OA_1} - \overrightarrow{OA}\right\|, l_2 = \left\|\overrightarrow{BB_1}\right\| = \left\|\overrightarrow{OB_1} - \overrightarrow{OB}\right\| \\ l_3 &= \left\|\overrightarrow{CC_1}\right\| = \left\|\overrightarrow{OC_1} - \overrightarrow{OC}\right\|, l_4 = \left\|\overrightarrow{DD_1}\right\| = \left\|\overrightarrow{OD_1} - \overrightarrow{OD}\right\|. \\ l_5 &= \left\|\overrightarrow{EE_1}\right\| = \left\|\overrightarrow{OE_1} - \overrightarrow{OE}\right\|, l_6 = \left\|\overrightarrow{FF_1}\right\| = \left\|\overrightarrow{OF_1} - \overrightarrow{OF}\right\| \end{aligned} \tag{16}$$

One coordinate system is attached to the base platform, which is fixed to ground, with the z axis pointing upwards to the top platform. The origin of the coordinate system is located right on the geometrical center of the base triangle platform.

Now considering some external wrench is applied on the top platform and the whole system is in static equilibrium with the six spring forces as the moving top platform twists relative to the fixed base platform. Here a wrench $\hat{w} = [\mathbf{f}; \mathbf{m_0}]$ can be thought of as a force $[\mathbf{f}; \mathbf{0}]$ acting though the origin together with a general couple $[\mathbf{0}; \mathbf{m_0}]$, adding these sets of coordinates together reproduces the original wrench coordinates. Similar to the wrench, a twist (written in axial coordinates) can be thought of as a rotation $[\mathbf{0}, \boldsymbol{\varphi}]$ about a line through the origin together with a general translation $[\mathbf{X}, \mathbf{0}]$, adding these sets of coordinates together reproduces the original six twist coordinates: $\hat{D} = [\mathbf{X}, \boldsymbol{\varphi}]$.[Gri91A]

In order to maintain the system equilibrium, the top platform moves as the external wrench changes. The incremental change of wrench may be written as $\delta\hat{w} = [\delta\mathbf{f}; \delta\mathbf{m}]$, and the form of the desired stiffness mapping of the compliant structure may be written as

$$\delta\hat{w} = [K]\delta\hat{D} \ , \tag{17}$$

where $[K]$ is the 6×6 stiffness matrix, which relates the incremental twist ($\delta\hat{D} = [\delta X, \delta\phi]$) of the top platform relative to the fixed base platform/ground to the incremental change of the wrench.

As it is specified in the previous chapters, the geometrical properties of the platform are known: the leg lengths are measured, while the dimensional values of the top and base triangles are invariant and pre-defined. The individual spring constants of the springs are also known.

In order to determine the mapping of (17), it is necessary to first differentiate (13), [Pigoski 98], which could also be written as

$$\begin{bmatrix} \mathbf{f} \\ \mathbf{m_0} \end{bmatrix} = \hat{w} = \mathbf{j}\boldsymbol{\lambda} = \mathbf{j} \begin{bmatrix} k_1(l_1 - l_{01}) \\ k_2(l_2 - l_{02}) \\ k_3(l_3 - l_{03}) \\ k_4(l_4 - l_{04}) \\ k_5(l_5 - l_{05}) \\ k_6(l_6 - l_{06}) \end{bmatrix},$$

(18)

where k_i is the individual spring constant of the i^{th} spring, and l_i, l_{0i} are the current length and free length of the i^{th} spring respectively, so that $k_i(l_i - l_{0i})$ is the force in the i^{th} leg due to the extension of the i^{th} spring. The Jacobian matrix **j** is:

$$\mathbf{j} = \begin{bmatrix} \mathbf{S}_1 & \mathbf{S}_2 & \mathbf{S}_3 & \mathbf{S}_4 & \mathbf{S}_5 & \mathbf{S}_6 \\ \mathbf{OA} \times \mathbf{S}_1 & \mathbf{OB} \times \mathbf{S}_2 & \mathbf{OC} \times \mathbf{S}_3 & \mathbf{OD} \times \mathbf{S}_4 & \mathbf{OE} \times \mathbf{S}_5 & \mathbf{OF} \times \mathbf{S}_6 \end{bmatrix}, \qquad (19)$$

where, S_i is the direction cosine of the axial line of the i^{th} leg. These direction cosines could be calculated and unitized via (8):

$$\mathbf{S}_1 = \frac{\mathbf{AA1}}{l_1}, \mathbf{S}_2 = \frac{\mathbf{BB1}}{l_2}, \mathbf{S}_3 = \frac{\mathbf{CC1}}{l_3}, \mathbf{S}_4 = \frac{\mathbf{DD1}}{l_4}, \mathbf{S}_5 = \frac{\mathbf{EE1}}{l_5}, \mathbf{S}_6 = \frac{\mathbf{FF1}}{l_6}$$

The lower three rows of the 6×6 matrix in (5.36) are the moments of the six lines relative to the reference point O. Because OA, OB, OC, OD, OE and OF are all fixed line vectors on the base platform triangle, and are constant, this matrix is solely a function of the direction cosines of the six legs.

The differential of equation (19) is expressed as

$$\begin{bmatrix} \boldsymbol{\delta f} \\ \boldsymbol{\delta m_o} \end{bmatrix} = \begin{bmatrix} S_1 & S_2 & S_3 & S_4 & S_5 & S_6 \\ OA \times S_1 & OB \times S_2 & OC \times S_3 & OD \times S_4 & OE \times S_5 & OF \times S_6 \end{bmatrix} \begin{bmatrix} k_1 \delta l_1 \\ k_2 \delta l_2 \\ k_3 \delta l_3 \\ k_4 \delta l_4 \\ k_5 \delta l_5 \\ k_6 \delta l_6 \end{bmatrix}$$

$$+ \begin{bmatrix} \delta S_1 & \delta S_2 & \delta S_3 & \delta S_4 & \delta S_5 & \delta S_6 \\ OA \times \delta S_1 & OB \times \delta S_2 & OC \times \delta S_3 & OD \times \delta S_4 & OE \times \delta S_5 & OF \times \delta S_6 \end{bmatrix} \begin{bmatrix} k_1 (l_1 - l_{01}) \\ k_2 (l_2 - l_{02}) \\ k_3 (l_3 - l_{03}) \\ k_4 (l_4 - l_{04}) \\ k_5 (l_5 - l_{05}) \\ k_6 (l_6 - l_{06}) \end{bmatrix}$$

(20)

Here δl_i is related to δD by the following expression:

$$\delta l = [\mathbf{j}]^T \, \delta \hat{D} \qquad (21)$$

where $[\mathbf{j}]$ is the Jacobian matrix of the parallel structure. The column of this 6×6 matrix is the line coordinates of the i^{th} leg [Gri91A].

Griffis demonstrated that in order to relate δS_i with $\delta \hat{D}$, each leg needs to have two derivatives, which are perpendicular to the axis of that leg at its base point, to describe the δS_i. Because each leg is individually connected to the base platform and top platform via a ball joint and a hook joint, it only possess two degrees of freedom: two rotations whose rotation axis are mutual perpendicular. Griffis also provides the stiffness mapping analysis for a 3-3 octahedral spatial platform: the analysis is based on Screw theory and utilizes some geometrical restrictions and configurations of the octahedral structure. Three examples include that two legs sharing one concentric ball joint at one fixed pivot, four legs sharing one triangle side and the pivots are located on the vertexes of the triangles. Although the analysis result is exclusively for the 3-3 octahedral mechanism, the conceptual approach is applicable to the general spatial stiffness analysis. The stiffness mapping of the special 6-6 parallel manipulator is determined by following the same procedure.

The general expression of the stiffness matrix for the special 6-6 parallel platform is presented as

$$\begin{aligned}[K] &= [\mathbf{j}][k_i][\mathbf{j}]^T + [\delta\mathbf{j_0}][k_i(1-\rho_i)][\delta\mathbf{j_0}]^T + [\delta\mathbf{j}_\alpha][k_i(1-\rho_i)][\delta\mathbf{j}_\alpha]^T \\ &+ [\delta\mathbf{j_0}][k_i(1-\rho_i)][V_\theta]^T + [\delta\mathbf{j}_\alpha][k_i(1-\rho_i)][V_\alpha]^T\end{aligned}, \quad (22)$$

where $[\mathbf{j}] = \begin{bmatrix} \mathbf{S}_1 & \mathbf{S}_2 & \mathbf{S}_3 & \mathbf{S}_4 & \mathbf{S}_5 & \mathbf{S}_6 \\ \mathbf{OA}\times\mathbf{S}_1 & \mathbf{OB}\times\mathbf{S}_2 & \mathbf{OC}\times\mathbf{S}_3 & \mathbf{OD}\times\mathbf{S}_4 & \mathbf{OE}\times\mathbf{S}_5 & \mathbf{OF}\times\mathbf{S}_6 \end{bmatrix}$

(22)

$$[k_i] = \begin{bmatrix} k_1 & 0 & 0 & 0 & 0 & 0 \\ 0 & k_2 & 0 & 0 & 0 & 0 \\ 0 & 0 & k_3 & 0 & 0 & 0 \\ 0 & 0 & 0 & k_4 & 0 & 0 \\ 0 & 0 & 0 & 0 & k_5 & 0 \\ 0 & 0 & 0 & 0 & 0 & k_6 \end{bmatrix}$$

$$[k_i(1-\rho_i)] = \begin{bmatrix} k_1(1-\rho_1) & 0 & 0 & 0 & 0 & 0 \\ 0 & k_2(1-\rho_2) & 0 & 0 & 0 & 0 \\ 0 & 0 & k_3(1-\rho_3) & 0 & 0 & 0 \\ 0 & 0 & 0 & k_4(1-\rho_4) & 0 & 0 \\ 0 & 0 & 0 & 0 & k_5(1-\rho_5) & 0 \\ 0 & 0 & 0 & 0 & 0 & k_6(1-\rho_6) \end{bmatrix} \quad (23)$$

and where $\rho_i = l_{0i} / l_i$ are dimensionless ratios incorporated to simplify the expressions.

Further,

$$[\delta\mathbf{j_0}] = \begin{bmatrix} \delta\mathbf{S}_1{}^\theta & \delta\mathbf{S}_2{}^\theta & \delta\mathbf{S}_3{}^\theta & \delta\mathbf{S}_4{}^\theta & \delta\mathbf{S}_5{}^\theta & \delta\mathbf{S}_6{}^\theta \\ \mathbf{OA}\times\delta\mathbf{S}_1{}^\theta & \mathbf{OB}\times\delta\mathbf{S}_2{}^\theta & \mathbf{OC}\times\delta\mathbf{S}_3{}^\theta & \mathbf{OD}\times\delta\mathbf{S}_4{}^\theta & \mathbf{OE}\times\delta\mathbf{S}_5{}^\theta & \mathbf{OF}\times\delta\mathbf{S}_6{}^\theta \end{bmatrix} \quad (24)$$

and

$$[\delta\mathbf{j}_\alpha] = \begin{bmatrix} \delta\mathbf{S}_1{}^\alpha & \delta\mathbf{S}_2{}^\alpha & \delta\mathbf{S}_3{}^\alpha & \delta\mathbf{S}_4{}^\alpha & \delta\mathbf{S}_5{}^\alpha & \delta\mathbf{S}_6{}^\alpha \\ \mathbf{OA}\times\delta\mathbf{S}_1{}^\alpha & \mathbf{OB}\times\delta\mathbf{S}_2{}^\alpha & \mathbf{OC}\times\delta\mathbf{S}_3{}^\alpha & \mathbf{OD}\times\delta\mathbf{S}_4{}^\alpha & \mathbf{OE}\times\delta\mathbf{S}_5{}^\alpha & \mathbf{OF}\times\delta\mathbf{S}_6{}^\alpha \end{bmatrix}, \quad (25)$$

where $\delta\mathbf{S}_i{}^\theta$, $\delta\mathbf{S}_i{}^\alpha$ are all unitized direction cosine vectors for the derivatives of the S_i vector; the three vectors are mutually perpendicular at the pivot point.

Next, six unit vectors are defined as intermediate variables describing the directional information of the base platform triangle sides as

$$\mathbf{u_1} = \frac{-\mathbf{EA}}{\|\mathbf{EA}\|}, \mathbf{u_2} = \frac{\mathbf{AC}}{\|\mathbf{AC}\|}, \mathbf{u_3} = \frac{-\mathbf{AC}}{\|\mathbf{AC}\|}, \mathbf{u_4} = \frac{-\mathbf{EC}}{\|\mathbf{EC}\|}, \mathbf{u_5} = \frac{\mathbf{EC}}{\|\mathbf{EC}\|}, \mathbf{u_6} = \frac{\mathbf{EA}}{\|\mathbf{EA}\|}. \quad (26)$$

$\mathbf{V}_i$ is given by the follow expression:

$$\mathbf{V}_i = \frac{\mathbf{u_i} \times \mathbf{S}_i}{\|\mathbf{u_i} \times \mathbf{S}_i\|} \quad (27)$$

$$\delta \mathbf{S}_i^{\ \theta} = \mathbf{V}_i \quad \text{and} \quad \delta \mathbf{S}_i^{\ \alpha} = \mathbf{V}_i \times \mathbf{S}_i \quad (28)$$

$$[\mathbf{V}_\alpha] = \begin{bmatrix} \mathbf{0} & \mathbf{0} & \mathbf{0} & \mathbf{0} & \mathbf{0} & \mathbf{0} \\ l_1 \cdot \mathbf{V}_1 & l_2 \cdot \mathbf{V}_2 & l_3 \cdot \mathbf{V}_3 & l_4 \cdot \mathbf{V}_4 & l_5 \cdot \mathbf{V}_5 & l_6 \cdot \mathbf{V}_6 \end{bmatrix} \quad (29)$$

$$[\mathbf{V}_\theta] = \begin{bmatrix} \mathbf{0} & \mathbf{0} & \mathbf{0} & \mathbf{0} & \mathbf{0} & \mathbf{0} \\ l_1 \cdot \mathbf{S}_1 \times \mathbf{V}_1 & l_2 \cdot \mathbf{S}_2 \times \mathbf{V}_2 & l_3 \cdot \mathbf{S}_3 \times \mathbf{V}_3 & l_4 \cdot \mathbf{S}_4 \times \mathbf{V}_4 & l_5 \cdot \mathbf{S}_5 \times \mathbf{V}_5 & l_6 \cdot \mathbf{S}_6 \times \mathbf{V}_6 \end{bmatrix} \quad (30)$$

where ‘ **0** ’ is a zero vector.

Substituting all the necessary components in equation (22) yields the global stiffness matrix of the special 6-6 parallel passive mechanism via the stiffness mapping analysis.

It is clear that the stiffness matrix can be written as the sum of five different matrices, the first three matrices are symmetric, while the last two matrices are asymmetric, so the overall stiffness matrix is asymmetric. It is obvious that the stiffness matrix is dependent on the selection of the coordinate system, so by using different coordinate systems, it might be possible to have a shorter or longer expression, but the change of coordinate system does not change the stiffness properties of the system, such as the rank of the matrix, or the eigenvectors and eigenvalues of the stiffness matrix (which are also called corresponding eigen-screw of stiffness and eigen-stiffness) [Gri91B], [Selig 02]. It is also intuitive that the stiffness property of a given compliant manipulator should not change just by using a different coordinate system, and neither could it be changed to be a symmetric matrix by choosing a different coordinate system

In the five matrices constituting the global stiffness matrix, only the first matrix does not have the diagonal matrix of $[k_i(1-\rho_i)]$. When the parallel compliant manipulator sustains a relatively small deflection (and a correspondingly small twist), and each leg also endures a relatively small amount of axial force, therefore each leg length is close to its initial length.

Then because $\rho_i = \frac{l_{0i}}{l_i} \approx \frac{l_{0i}}{l_{0i}} = 1$, all the other four matrice's components who contain the diagonal matrix of $[k_i(1-\rho_i)]$ are so close to the zero matrix that their effects can be neglected and only the first part of the global stiffness matrix is left. With these simplifications, the stiffness matrix is a positive definite symmetric matrix.

Consider an example parallel passive platform with the special 6-6 configuration shown in Figure 3.2a.1) that has the following specifications:

a = 60 mm, b =120 mm,

p=0.233,

k_i = 20 lb/ in = 3.5003 N/mm.

The stiffness matrix of the system will be calculated for the case when it is sustaining a small external wrench in static equilibrium and the top platform is slightly deflected from its original position. The corresponding Jacobian matrix of the structure is calculated as

$$[j] = \begin{bmatrix} -0.65457 & -0.23529 & 0.19761 & -0.23529 & 0.45696 & 0.47059 \\ 0.14974 & 0.40754 & -0.64174 & -0.40754 & 0.492 & 0 \\ 0.74102 & 0.88235 & 0.74102 & 0.88235 & 0.74102 & 0.88235 \\ -25.67 & -9.1697 & 51.34 & 39.735 & -25.67 & -30.566 \\ -44.461 & -40.588 & 0 & 12.353 & 44.461 & 28.235 \\ -13.691 & 16.302 & -13.691 & 16.302 & -13.691 & 16.302 \end{bmatrix}$$

where each column is the Plücker line coordinates of the axis for each leg, the upper three numbers are unit less, the lower three numbers have the unit of mm.

The corresponding stiffness matrix is calculated as

$$\begin{bmatrix} 3.5301 & 0 & 0 & -22.256 & 242.75 & 0 \\ 0 & 3.5301 & 0 & -242.75 & -22.256 & 0 \\ 0 & 0 & 13.942 & 0 & 0 & 44.511 \\ -22.256 & -242.75 & 0 & 22930 & 0 & 0 \\ 242.75 & -22.256 & 0 & 0 & 22930 & 0 \\ 0 & 0 & 44.511 & 0 & 0 & 4758.7 \end{bmatrix}$$

In this matrix, the units are also different. The four 3×3 sub-matrices have the following units

$$\begin{bmatrix} N/mm & N \\ N & N\square mm \end{bmatrix}$$

3.2a.6 Forward Analysis:

The kinematic forward analysis is very important to control applications. In this chapter, the forward kinematic analysis for parallel 3-3 manipulator is introduced. Then a geometrical method, patented by Duffy and Griffis [Gri93], of determining the equivalent 3-3 parallel structure for a special 6-6 configuration mechanism is described.

3.2a.7 Forward Kinematic Analysis for 3-3 Platform

It is necessary to determine the position and orientation of the end effector of the manipulator. Given the geometrical properties of the parallel platform, including leg length, connector pivots locations and etc., the forward kinematic analysis determines the relation between the end effector pose and it geometrical properties. As stated in the previous chapters, the forward kinematic analysis is complicated compared to the reverse kinematic analysis. This problem is also geometrically equivalent to the problem of finding out ways to place a rigid body such that six of its given points lie on six given spheres.

During the late 80's and early 90's of last century, many researchers had worked on the forward kinematic analysis of parallel manipulators. Many different approaches such as closed-form solutions of special cases, numerical schemes, and analytical approaches were considered for both special cases and general 6-6 configurations. Hunt [Hun98] studied the geometry and mobility of the 3-3 in-parallel manipulator. Wen and Liang [Wen 94] used an analytical approach and solved the problem for the 6-6 Stewart platform with a planar base and platform by reducing of the kinematic equations into a uni-variate polynomial and concluded that the upper bound of the solutions for forward kinematic problems is 40 for this class. Merlet [Mer92][Metlet 2000] had studied direct kinematic solutions for general 6-6 parallel platform and special cases with additional sensors.

Various researchers have stated that for a general 6-6 in-parallel platform and with a given set of fixed leg lengths, it is possible to assemble it in 40 different configurations [Hun98], [Dasgupta 2000]. It is not likely that all of the 40 configurations are real and applicable. Due to the difficulty of the forward kinematic analysis for the general 6-6 in-parallel platform, it is worthwhile to consider some special cases with reduced complexity. The simplest form of this class is first analyzed.

Although there are different configurations and designs for a simple spatial parallel platform, the symmetric 3-3 parallel platform shown in Figure 3.2a.3 is among the most important and widely analyzed structures.

This 3-3 parallel platform is also called an 'octahedron'. It has eight triangular faces, six vertices and twelve edges. Four edges are concurrent at each vertex. Every vertex is contained in four faces. The device has all six degrees of freedom, ignoring the trivial freedom of each leg rotating about its own axis.

The forward kinematic analysis for the 3-3 in-parallel manipulator was first solved by Griffis and Duffy [Gri89] who showed that the position and orientation of the top platform can be determined with respect to the base when given the lengths of the six connectors as well as the geometry of the connection points on the top and base. The solution is a closed-form solution and is based on the analysis of the input/output relationship of three spherical four bar mechanisms. The three spherical four bar mechanisms (see Figure 3.2a.5) result in three equations in the tan-half angle of the three unknowns θ_x, θ_y, and θ_z. These tan-half angles are simply named x, y, and z. Elimination of the variables y and z results in the following polynomial which contains the variable x as its only unknown [Gri89].

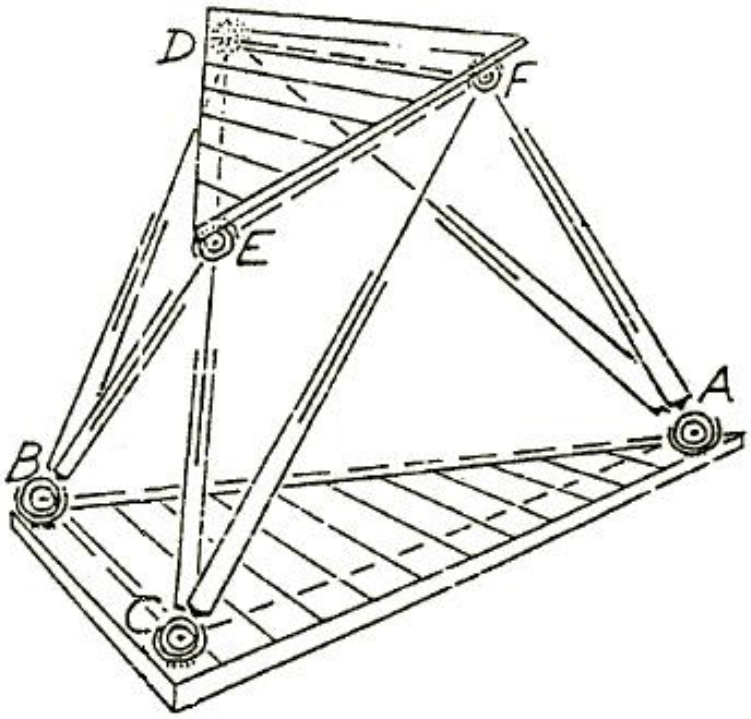

Figure 3.2a. 3-D drawing of the 3-3 in-parallel platform

$$\mathrm{E} = \alpha^2 - 4\beta\rho_1\rho_2, \tag{31}$$

where

$$\begin{aligned}
\alpha \;=\; & 2A_3B_3a_2c_1^{\,2}c_2 - 4A_3B_3c_1^{\,2}b_2^{\,2} + 2A_3C_3a_1c_1c_2^{\,2} - 4A_3C_3c_2^{\,2}b_1^{\,2} \\
& -2A_3E_3a_1a_2c_1c_2 + 4A_3E_3a_1c_1b_2^{\,2} + 4A_3E_3a_2c_2b_1^{\,2} \\
& -8A_3E_3b_1^{\,2}b_2^{\,2} - 2A_3D_3c_1c_1b_1b_2 - 2B_3C_3a_1a_2c_1c_2 \\
& +4B_3C_3a_1c_1b_2^{\,2} + 4B_3C_3a_2c_2b_1^{\,2} - 8B_3C_3b_1^{\,2}b_2^{\,2} \\
& +2B_3E_3a_1a_2^{\,2}c_1 - 4B_3E_3a_2^{\,2}b_1^{\,2} - 2B_3D_3a_2c_1b_1b_2 \\
& +2C_3E_3a_1^{\,2}a_2c_2 - 4C_3E_3a_1^{\,2}b_2^{\,2} - 2C_3D_3a_1c_2b_1b_2 \\
& -2D_3E_3a_1a_2b_1b_2 - D_3^{\,2}a_1a_2c_1c_2 - A_3^{\,2}c_1^{\,2}c_2^{\,2} \\
& -B_3^{\,2}c_1^{\,2}a_2^{\,2} - C_3^{\,2}a_1^{\,2}c_2^{\,2} - E_3^{\,2}a_1^{\,2}a_2^{\,2}
\end{aligned}$$

$$\begin{aligned}
\beta \;=\; & 4A_3E_3b_1b_2 + A_3D_3c_1c_2 + D_3E_3a_1a_2 \\
& -4B_3C_3b_1b_2 - B_3D_3c_1a_2 - C_3D_3a_1c_2
\end{aligned}$$

$$\rho_1 = b_1^{\,2} - a_1c_1$$
$$\rho_2 = b_2^{\,2} - a_2c_2$$

$$a_1 = A_1x^2 + C_1, \quad b_1 = 0.5D_1x, \quad c_1 = B_1x^2 + E_1$$
$$a_2 = A_2x^2 + B_2, \quad b_2 = 0.5D_2x, \quad c_2 = C_2x^2 + E_2$$

The coefficients $A_i, \ldots, E_i, i = 1, 2, 3$ are expressed in terms of known quantities. Their values for the generic spherical four bar mechanism shown in Figure 3.2a.6-2 may be written as

$$\begin{aligned}
A &= s_{12}c_{41}s_{34} - s_{12}s_{41}c_{34} - s_{41}s_{34}c_{12} + c_{23} - c_{12}c_{41}c_{34} \\
B &= -s_{12}c_{41}s_{34} - s_{12}s_{41}c_{34} + s_{41}s_{34}c_{12} + c_{23} - c_{12}c_{41}c_{34} \\
C &= -s_{12}c_{41}s_{34} + s_{12}s_{41}c_{34} - s_{41}s_{34}c_{12} + c_{23} - c_{12}c_{41}c_{34} \\
D &= -4s_{12}s_{34} \\
E &= s_{12}c_{41}s_{34} + s_{12}s_{41}c_{34} + s_{41}s_{34}c_{12} + c_{23} - c_{12}c_{41}c_{34}
\end{aligned}$$

where $s_{ij} = \sin(\alpha_{ij})$ and $c_i = \cos(\alpha_i)$. For this problem, the coefficients are obtained by replacing the vertex as the origin of the three spherical four-bar linkages (shown in Figure 3.2a.6-3) with points o, p, and q respectively. The corresponding mapping of the angles of the spherical four-bar linkages is shown in Table 3.2a. 1.

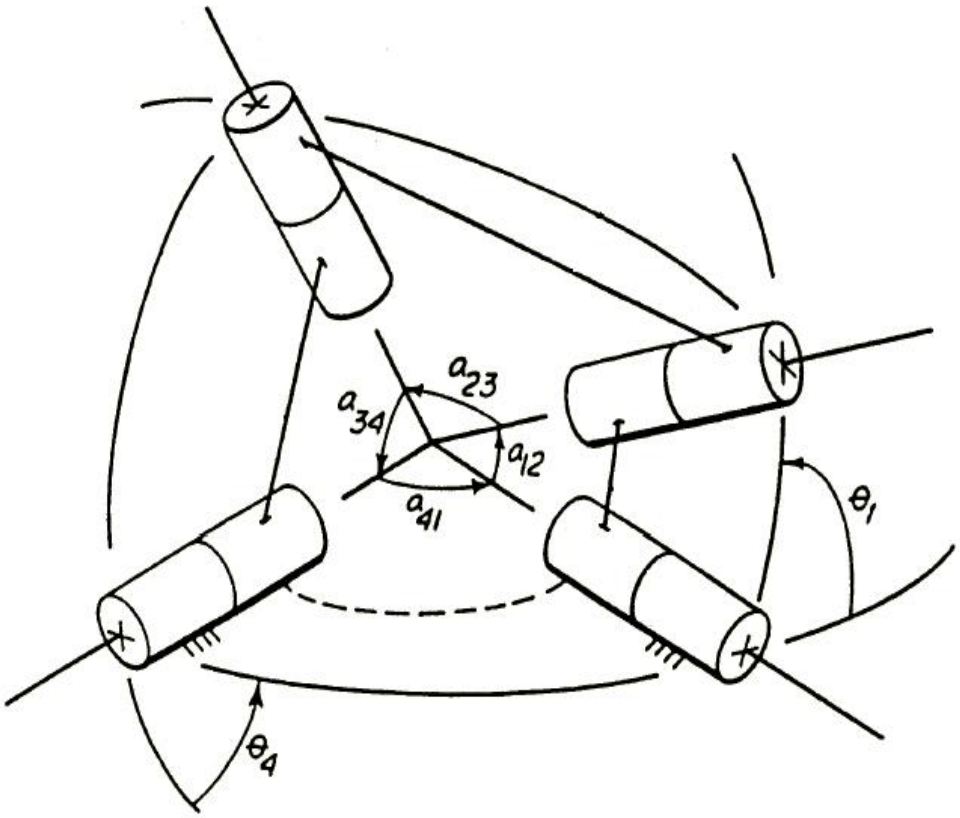

Figure 3.2a.4. A general spherical four-bar mechanism, Griffis [89]

Table 3.2a. 1. Mappings of angles of spherical four bar mechanism.

Origin	o	p	Q
Output: a_{12}	$\angle qor$	$\angle ops$	$\angle pqr$
Coupler: a_{23}	$\angle ros$	$\angle spt$	$\angle tqr$
Input: a_{34}	$\angle sop$	$\angle tpq$	$\angle rqo$
Ground: a_{41}	$\angle poq$	$\angle pqo$	$\angle oqp$

The resulting solution shown above is an eighth degree polynomial in the square of one variable which yields a maximum of sixteen solution poses for any given set of connector lengths and base-top triangles lengths. Eight solutions were reflected about the plane formed

by the base connector points. There can be up to 16 real solutions and therefore, there can be 0,2,4,6 or 8 pairs of real, reflected solutions.

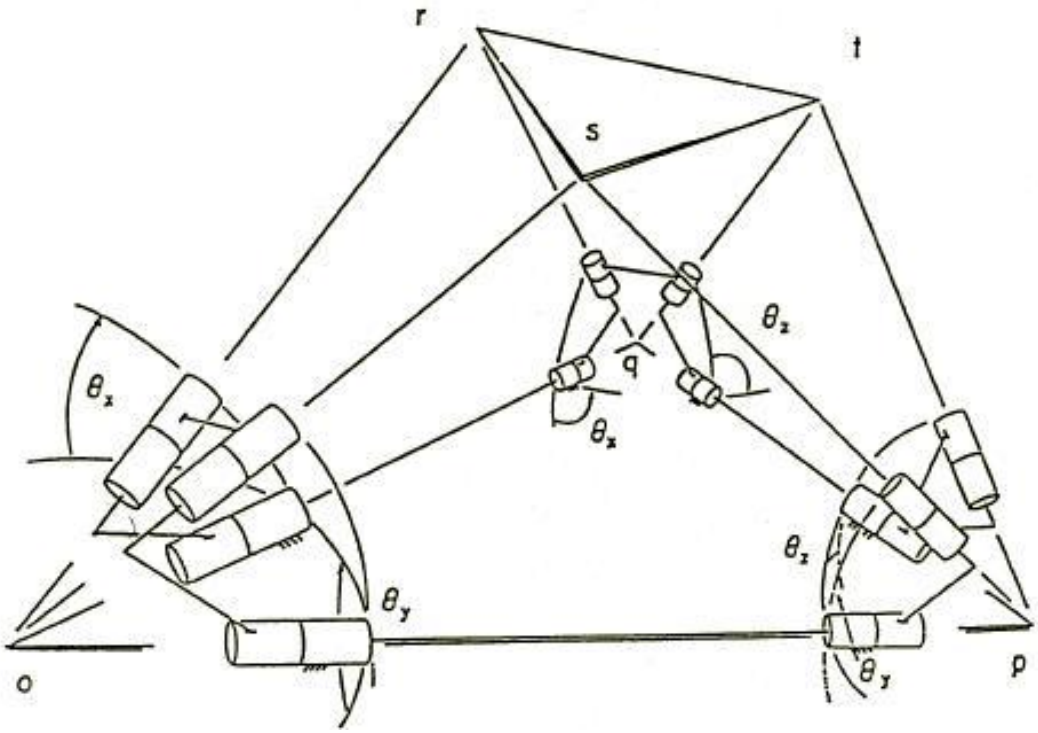

Figure 3.2a.5. 3-3 in-parallel mechanism with three spherical four-bar linkages, Griffis [89]

3.2a.8 Forward kinematic analysis for special 6-6 in-parallel platform

The configuration of the special 6-6 in-parallel platform is carefully chosen such that the forward kinematic analysis can use a method similar to the method for the 3-3 in-parallel platform. This section will show the geometric relationship between the special 6-6 in-parallel platform and an equivalent 3-3 platform and how to solve the direct kinematic analysis problem by using this conversion. The relationship between a Special 6-6 platform and its equivalent 3-3 platform was discovered by Griffis and Duffy [Gri93] and is presented here for completeness as the forward analysis is an important part of the control algorithm for the force control device developed in this dissertation.

A Special 6-6 platform is defined as one which is geometrically reducible to an equivalent 3-3 platform. Figure 3.2a.6-4 depicts a perspective and plan view of a 6-6 platform where the leg connector points R_0, S_0, and T_0 lie along the edges of the triangle defined by points O_0, P_0, and Q_0 and the leg connector points O_1, P_1, and Q_1 lie along the edges of the triangle defined by the points R_1, S_1, and T_1. The objective here is to determine the distance between the pairs of

points O_0 - R_1, O_0 - S_1, P_0 - S_1, P_0 -T_1 , Q_0 - T_1, and Q_0 - R_1. These distances represent the leg connector lengths for an equivalent 3-3 platform.

Throughout this analysis, the notation m_in_j will be used to represent the distance between the two points M_i and N_j and the notation minj will represent the vector from point M_i to N_j. Using this notation, the problem statement can be written as:

given: o_0o_1, p_0p_1, q_0q_1, r_0r_1, s_0s_1, t_0t_1 connector lengths for Special 6-6 platform

o_0p_0, p_0q_0, q_0o_0, o_0s_0, p_0t_0, q_0r_0 base triangle parameters

r_1s_1, s_1t_1, t_1r_1, r_1o_1, s_1p_1, t_1q_1 top triangle parameters

find: o_0r_1, o_0s_1, p_0s_1, p_0t_1, q_0t_1, q_0r_1 connector lengths for equivalent 3-3 platform

Obviously it is the case that

$$s_0p_0 = o_0p_0 - o_0s_0 \quad ; \quad t_0q_0 = p_0q_0 - p_0t_0 \quad ; \quad r_0o_0 = q_0o_0 - q_0r_0$$

$$o_1s_1 = r_1s_1 - r_1o_1 \quad ; \quad p_1t_1 = s_1t_1 - s_1p_1 \quad ; \quad q_1r_1 = t_1r_1 - t_1q_1 \,. \tag{32}$$

The six leg connectors of the equivalent 3-3 platform define an octahedron, i.e. there are eight triangular faces; the top and bottom platform triangles and six faces defined by two intersecting connectors and an edge of either the base or top platform. The solution begins by first defining angles β and γ which, for each of the six faces defined by intersecting connectors, defines the angle in the plane between a connector of the Special 6-6 platform and an edge of either the top or base platform as appropriate.

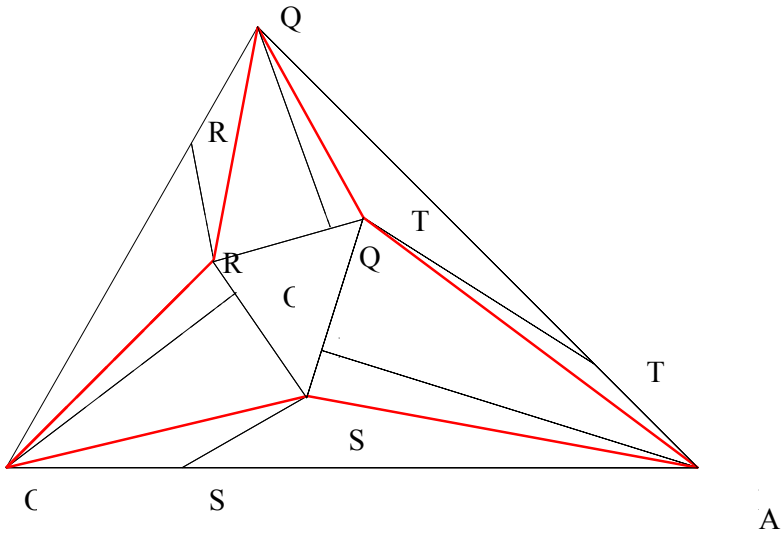

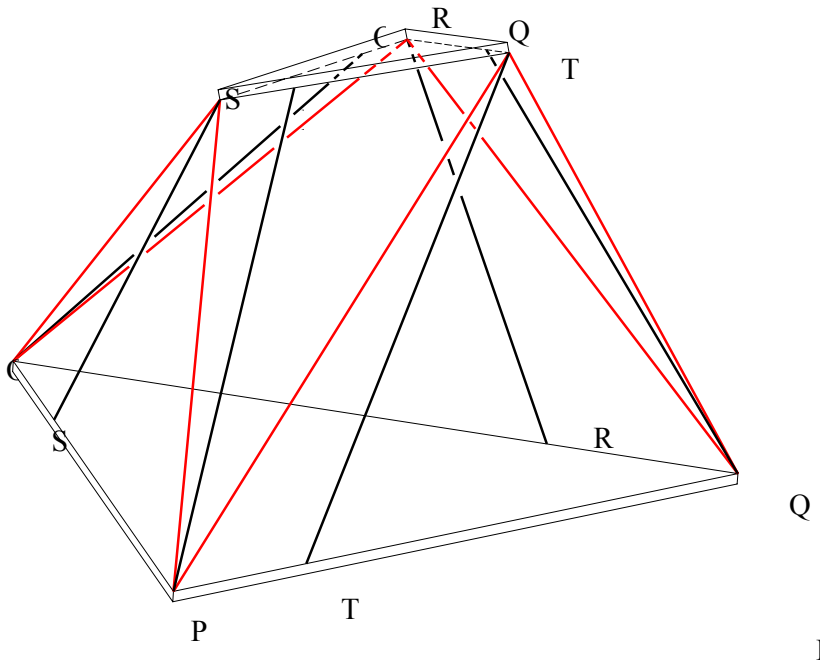

Figure 3.2a.6. Special 6-6 platform and equivalent 3-3 platform, A) Perspective view, B) Plan view

Figure 3.2a.6 shows the angles γ_1 and β_1. The angle γ_2 is defined as the angle between r0r1 and r0o0 and the angle γ_3 is defined as the angle between s0s1 and s0o0. Similarly, the angle β_2 is defined as the angle between q1t1 and q1q0 and the angle β_3 is defined as the angle between o1s1 and o1o0.

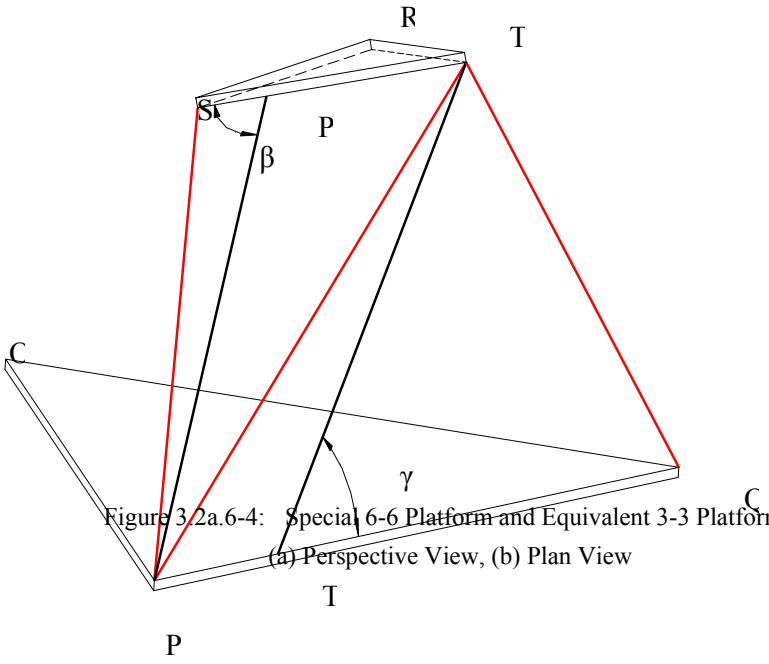

Figure 3.2a.6-4: Special 6-6 Platform and Equivalent 3-3 Platform ; (a) Perspective View, (b) Plan View

Figure 3.2a.7. Definition of angles β and γ

Figure 3.2a.6-6 shows a planar triangle that is defined by the vertex points G_1, G_2, and G_3. A point G_0 is defined as a point on the line defined by G_1 and G_2 and the angle φ is shown as the angle between g0g2 and g0g3. The cosine law for the triangle defined by points G_0, G_2, and G_3 yields

$$\cos\varphi = \frac{b^2 + c^2 - \ell_b{}^2}{2\,b\,c} \qquad (33)$$

Next consider that the triangle lies in a plane defined by u and v coordinate axes. The coordinates of any point G_i may then be written as (u_i, v_i). The distance ℓ_a may then be expressed as

$$\begin{aligned} \ell_a{}^2 &= (u_3 - u_1)^2 + (v_3 - v_1)^2 \\ &= (a + c\cos\varphi)^2 + (c\sin\varphi)^2 \\ &= c^2(\sin^2\varphi + \cos^2\varphi) + a^2 + 2\,a\,c\cos\varphi \\ &= a^2 + c^2 + 2\,a\,c\cos\varphi \end{aligned}$$

(34)

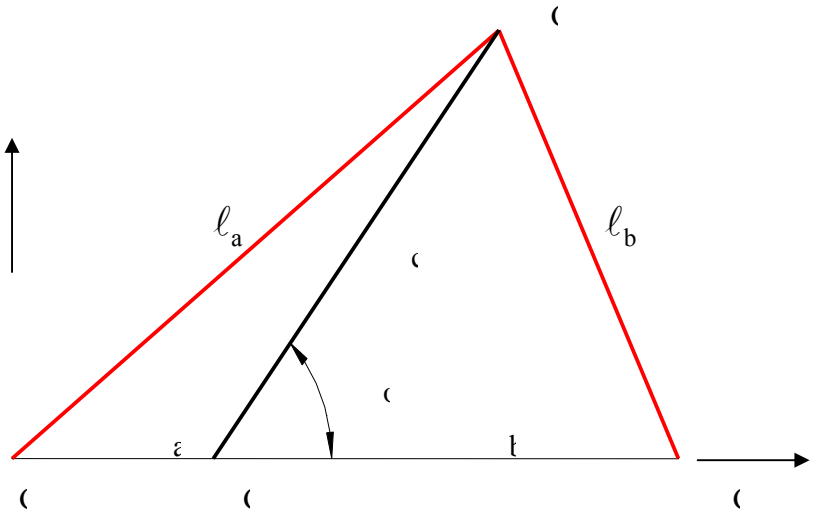

Figure 3.2a.8. Planar triangle

Substituting (6.3) into (6.4) and simplifying gives

$$\begin{aligned} \ell_a{}^2 &= a^2 + c^2 + \frac{a}{b}(b^2 + c^2 - \ell_b{}^2) \\ &= \frac{1}{b}(b\,a^2 + b\,c^2 + a\,b^2 + a\,c^2 - a\,\ell_b{}^2) \end{aligned} \qquad (35)$$

Regrouping this equation gives

$$b\,\ell_a^{\,2} + a\,\ell_b^{\,2} = (a+b)\,c^2 + a\,b^2 + a^2\,b = (a+b)(c^2+ab) \quad . \tag{36}$$

The result of equation (36) can be applied to each of the six side faces of the octahedron defined by the leg connectors of the equivalent 3-3 platform. The parameter substitutions are shown in Table 3.2a. 2.

Table 3.2a. 2: Parameter substitutions

Φ	G_0	G_1	G_2	G_3	a	b	c	ℓ_a	ℓ_b
β_1	P_1	T_1	S_1	P_0	p_1t_1	p_1s_1	p_0p_1	p_0t_1	p_0s_1
β_2	Q_1	R_1	T_1	Q_0	q_1r_1	t_1q_1	q_0q_1	q_0r_1	q_0t_1
β_3	O_1	S_1	R_1	O_0	s_1o_1	o_1r_1	o_0o_1	o_0s_1	o_0r_1
γ_1	T_0	P_0	Q_0	T_1	p_0t_0	t_0q_0	t_0t_1	p_0t_1	q_0t_1
γ_2	R_0	Q_0	O_0	R_1	q_0r_0	r_0o_0	r_0r_1	q_0r_1	o_0r_1
γ_3	S_0	O_0	P_0	S_1	o_0s_0	s_0p_0	s_0s_1	o_0s_1	p_0s_1

Using Table 3.2a. 2 to perform appropriate parameter substitutions in (A-5) will result in six equations that can be written in matrix form as

$$A\,q = M \quad , \tag{37}$$

where

$$\mathbf{A} = \begin{bmatrix} p_1s_1 & p_1t_1 & 0 & 0 & 0 & 0 \\ 0 & 0 & t_1q_1 & q_1r_1 & 0 & 0 \\ 0 & 0 & 0 & 0 & o_1r_1 & s_1o_1 \\ t_0q_0 & 0 & 0 & p_0t_0 & 0 & 0 \\ 0 & 0 & r_0o_0 & 0 & 0 & q_0r_0 \\ 0 & o_0s_0 & 0 & 0 & s_0p_0 & 0 \end{bmatrix} \quad \mathbf{q} = \begin{bmatrix} p_0t_1^{\,2} \\ p_0s_1^{\,2} \\ q_0r_1^{\,2} \\ q_0t_1^{\,2} \\ o_0s_1^{\,2} \\ o_0r_1^{\,2} \end{bmatrix} \quad \mathbf{M} = \begin{bmatrix} M_1 \\ M_2 \\ M_3 \\ M_4 \\ M_5 \\ M_6 \end{bmatrix} \tag{38}$$

where

M1 = (p1t1+p1s1) (p0p12 + p1t1 p1s1),
M2 = (q1r1+t1q1) (q0q12 + q1r1 t1q1),
M3 = (s1o1+o1r1) (o0o12 + s1o1 o1r1),
M4 = (p0t0+t0q0) (t0t12 + p0t0 t0q0), (39)
M5 = (q0r0+r0o0) (r0r12 + q0r0 r0o0),
M6 = (o0s0+s0p0) (s0s12 + o0s0 s0p0).

Then these equations are manipulated such that dividing the first rows of A and M by $p_1t_1+p_1s_1= s_1t_1$, the second rows by $q_1r_1+t_1q_1= r_1t_1$, and so on to obtain

$$A'q = M' \quad , \qquad (40)$$

where

$$\mathbf{A}' = \begin{bmatrix} p & 1-p & 0 & 0 & 0 & 0 \\ 0 & 0 & q & 1-q & 0 & 0 \\ 0 & 0 & 0 & 0 & w & 1-w \\ 1-t & 0 & 0 & t & 0 & 0 \\ 0 & 0 & 1-r & 0 & 0 & r \\ 0 & s & 0 & 0 & 1-s & 0 \end{bmatrix} \qquad \mathbf{M}' = \begin{bmatrix} p_0 p_1^{\,2} + p_1 t_1 p_1 s_1 \\ q_0 q_1^{\,2} + q_1 r_1 t_1 q_1 \\ o_0 o_1^{\,2} + s_1 o_1 o_1 r_1 \\ t_0 t_1^{\,2} + p_0 t_0 t_0 q_0 \\ r_0 r_1^{\,2} + q_0 r_0 r_0 o_0 \\ s_0 s_1^{\,2} + o_0 s_0 s_0 p_0 \end{bmatrix}$$

with

$$p = \frac{p_1 s_1}{p_1 s_1 + p_1 t_1} = \frac{p_1 s_1}{s_1 t_1} \qquad t = \frac{t_0 p_0}{t_0 p_0 + t_0 q_0} = \frac{t_0 p_0}{p_0 q_0}$$

$$q = \frac{q_1 t_1}{q_1 t_1 + q_1 r_1} = \frac{q_1 t_1}{r_1 t_1} \qquad r = \frac{r_0 q_0}{r_0 q_0 + r_0 o_0} = \frac{r_0 q_0}{q_0 o_0}$$

$$w = \frac{o_1 r_1}{o_1 r_1 + o_1 s_1} = \frac{o_1 r_1}{r_1 s_1} \qquad s = \frac{s_0 o_0}{s_0 o_0 + s_0 p_0} = \frac{s_0 o_0}{o_0 p_0}$$

Note that $0 \le p, q, w, t, r, s \le 1$.

The matrix $\mathbf{A}'$ is dimensionless and depends only on the ratios of where the connections occur along the sides of the upper and lower bases. Matrix $\mathbf{A}'$ is also independent of the shapes of the upper and lower triangles. Now all the terms in matrix $\mathbf{A}'$ are known as they are dimensionless ratios expressed in terms of given distances of the top and bottom platform. All the terms in vector M' are also known as they are expressed in terms of given dimensions as well as the square of the lengths of the six leg connectors of the Special 6-6 platform. Thus the square of the lengths of the connectors for the equivalent 3-3 platform may be determined as:

$$q = A^{-1}M' \qquad (41)$$

Further more, the determinant of $\mathbf{A}'$ is:

$$\det(\mathbf{A}) = (1-p)(1-q)(1-w)(1-t)(1-r)(1-s) - pqwtrs \qquad (42)$$

It is interesting to note that the matrix $\mathbf{A}'$ is singular if and only if the following condition is satisfied:

$$\frac{s_0p_0}{s_1p_1}\frac{t_0q_0}{t_1q_1}\frac{o_0r_0}{o_1r_1} = \frac{q_0r_0}{q_1r_1}\frac{o_0s_0}{o_1s_1}\frac{p_0t_0}{p_1t_1} \qquad (43)$$

One case where this could happen would be if all the middle connector pointes S_0, T_0, R_0, O_1, P_1, and Q_1 are located at the midpoints of the sides of the upper and lower triangles. We can also conclude that for $\mathbf{A}'$ to be singular, if some of the parameters p, q, w, t, r, s are less than ½ then some of the other parameters must be greater than ½. Thus we immediately conclude that if all of the parameters are less than ½ (as is the case in Figure 3.2a.A-1), then $\mathbf{A}'$ is non-singular. The same statement of course is true if all the parameters are greater than ½.Once the leg length dimensions of the equivalent 3-3 platform are determined, the forward analysis of the 3-3 device as described in previous section is used to determine the position and orientation of the top platform relative to the base platform.

3.2a.9 Experiment Analysis

Calibration experiment of the force sensor:

In order to get the force/ displacement relationship of the compliant connectors, the detected force signal and the corresponding displacement signal should be recorded simultaneously during the individual leg calibration experiment.

A load cell is used to measure the axial force applied on the individual leg. The rated capacity of the load cell is 5 lb, (22.246 N) and the output of the load cell is an analog voltage signal, ranging from -5~+5 Vdc. The rated output is 2mV/V ± 20%. It is necessary to calibrate the load cell first to ensure the validity and accuracy of the following experiments' results.

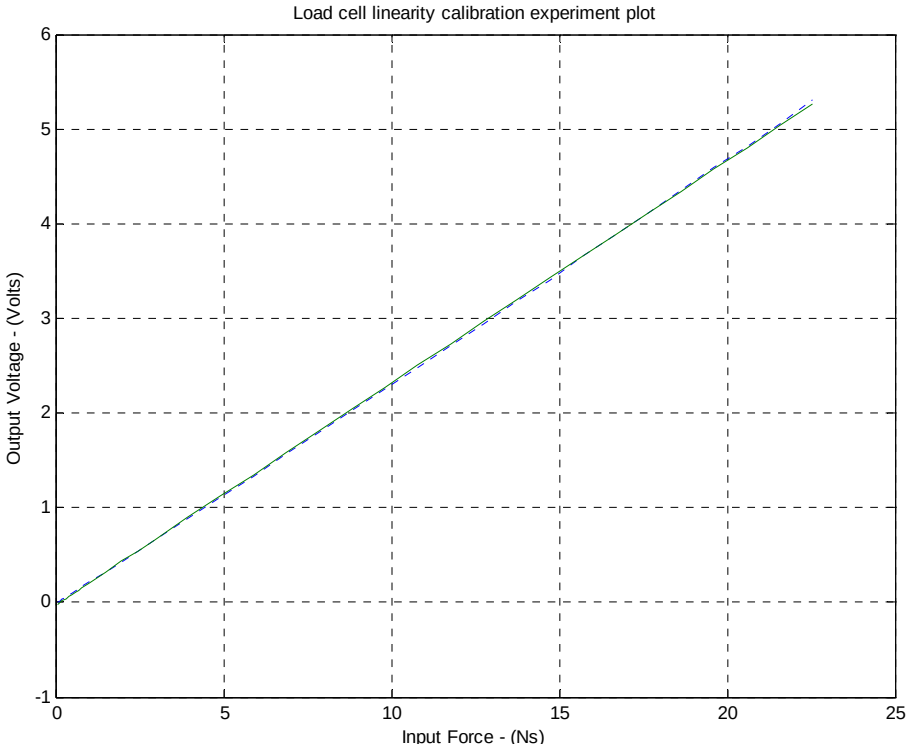

Figure 3.2a.9. Load cell calibration experiment

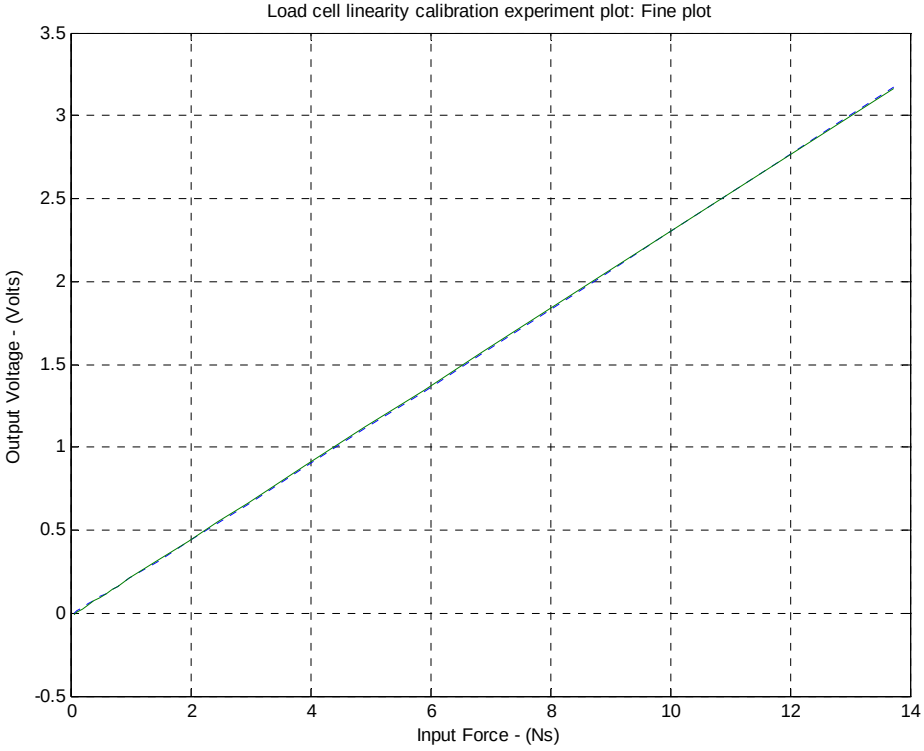

Figure 3.2a.10. Load cell calibration experiment - opposite direction

The load cell output analog signal is connected to an A/D port of a multi-functional I/O board and the value of the voltage is recorded with the corresponding known force, which is provided by a set of standard weights for accurate force calibration. The mapping of the force/voltage relationship is shown in Figure 3.2a.9 and Figure 3.2a.10.

Five sets of experimental data are analyzed and the plots are very similar, so only one plot is shown here. The linear equation that relates the applied force to the measured voltage can be written as

$$y = k_1 x, \tag{44}$$

where the coefficient k_1 is determined to equal 0.00225 Volt/gram.

The linear regression statistics are shown in Table 3.2a. 3.

Table 3.2a. 3 Load cell regression statistics

Regression Statistics	
Multiple R	0.999115584
R Square	0.998231949
Adjusted R Square	0.966981949
Standard Error	0.059572297(V)

From the Table 3.2a. and the Figure 3.2a.above, the load cell shows very high linearity and is adequate to be used in the following experiments.

3.2a.10 Individual leg calibration experiment

After calibrating the load cell, it is necessary to calibrate the compliant connectors and identify the stiffness property for each of them. During the experiment, the compliant connector is fixed vertically and is attached to the load cell in such a way that the applied external force causing either elongation or compression can be detected properly. The two physical quantities, force and displacement, are detected by the load cell and the optical encoder. The optical encoder is attached on the compliant leg both for the calibration experiment and for the designed operation.

Axial force is applied on the top of the compliant leg with variable magnitude and direction in order to get the stiffness mapping of the leg for both compression and elongation. The resolution of the optical encoder is 1000 counts/inch.

In the calibration plots, the displacement is measured in mm and force measured in Newtons. In the original data file, the displacement at each sample time is recorded as encoder counts and the force is recorded as digitized voltage value. Then the units are converted by the load cell calibration experiment results together with the following conversion equations:

$1\ in = 25.4\ mm$

$1\ lb = 453.6\ gram\ = 4.448\ \text{N}$

Then, the data in the plots is used to build six individual look-up Table 3.2a.s of displacement vs. force for each leg. During operation, the relative displacement is measured and the corresponding force value is obtained from the look-up Table 3.2a.. These calibration Table 3.2a.s can also be replaced by linear regression of the data for less-accurate operations, and thus a 'linear spring constant' is assigned to each leg.

The individual plot of the stiffness mapping is shown in Figures 11 through 16.

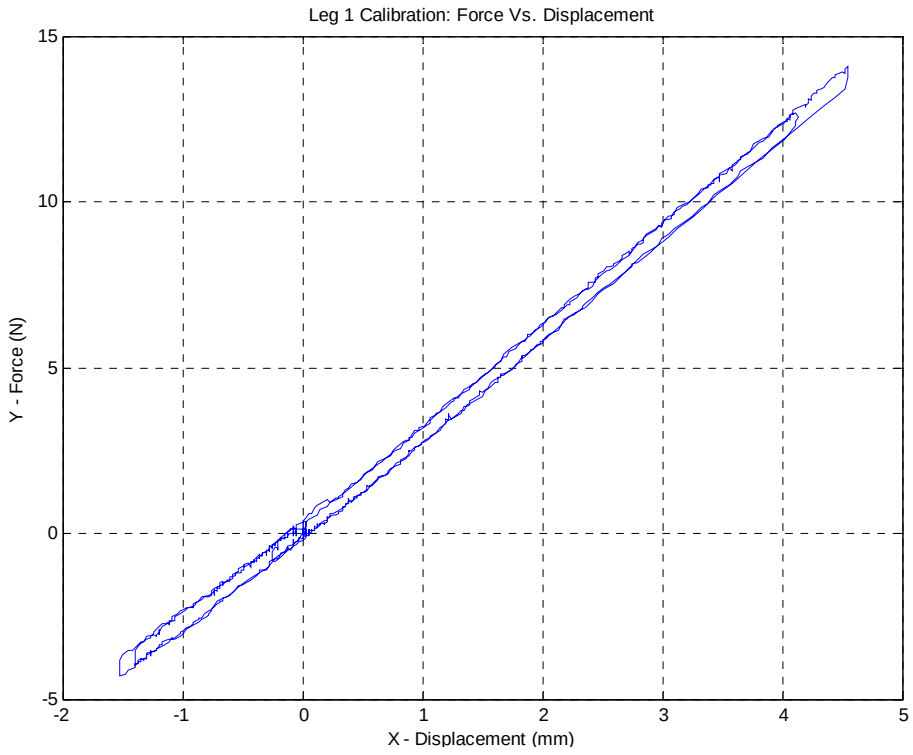

FFigure 3.2a.11. Calibration plot for leg 1.

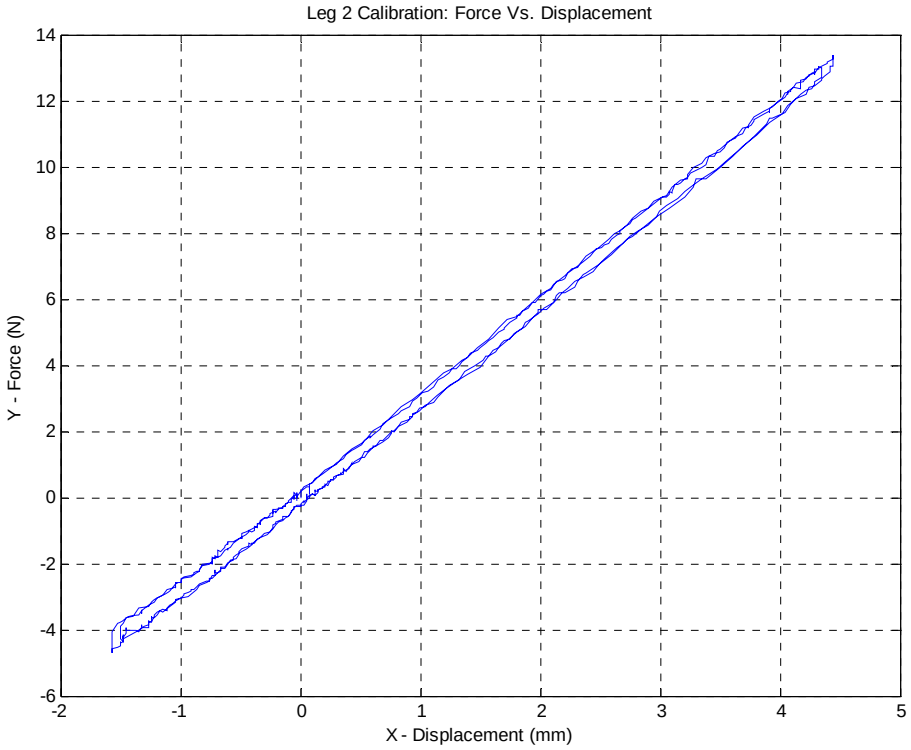

Figure 3.2a.12. Calibration plot for leg 2.

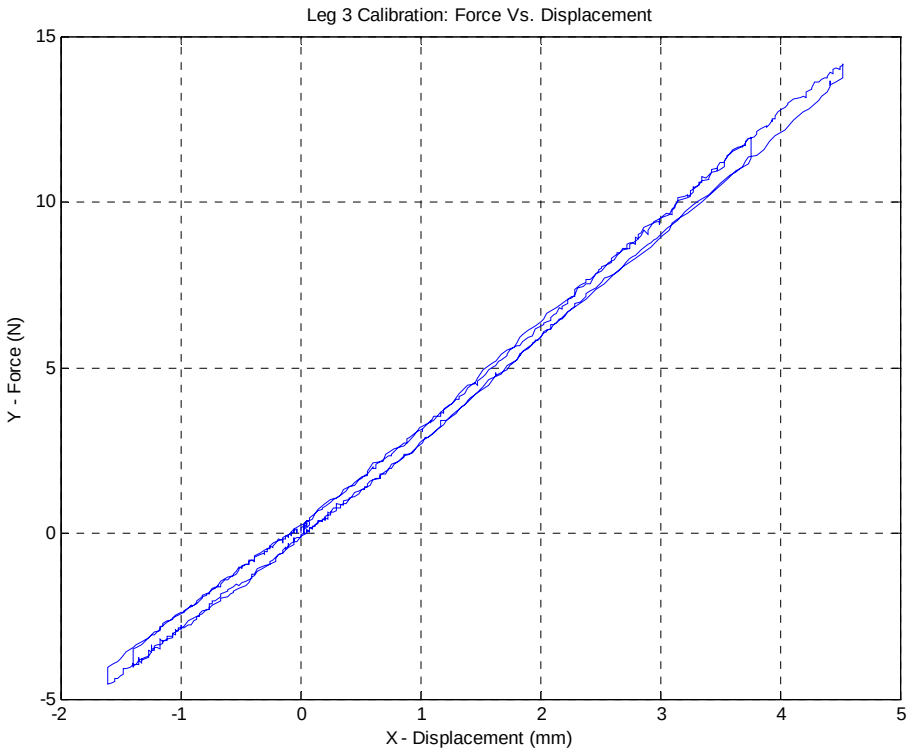

Figure 3.2a.13. Calibration plot for leg-3

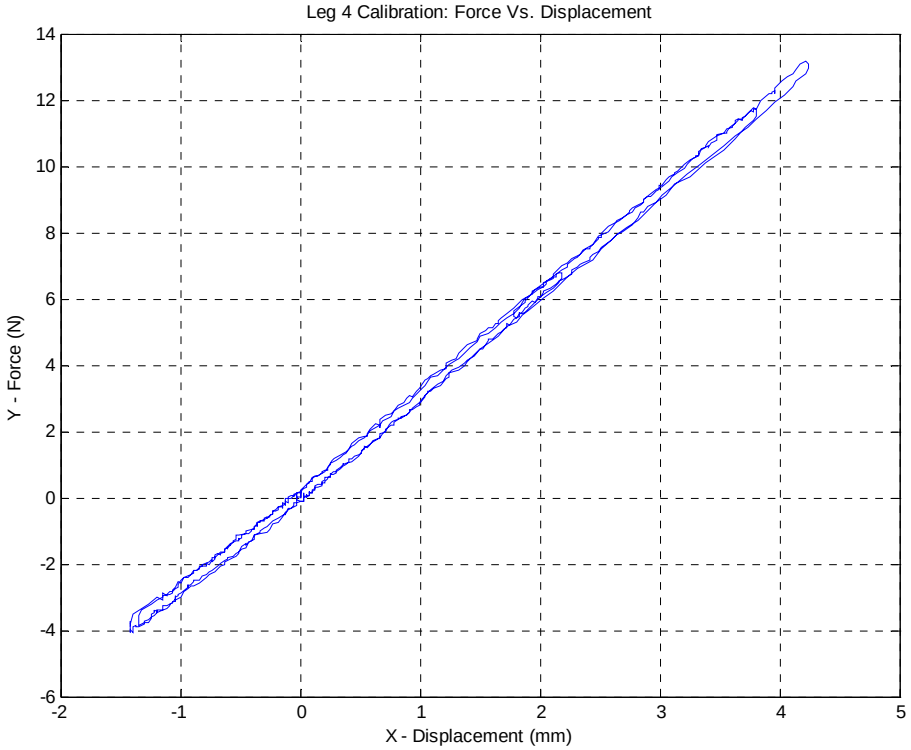

Figure 3.2a.14. Calibration plot for leg-4.

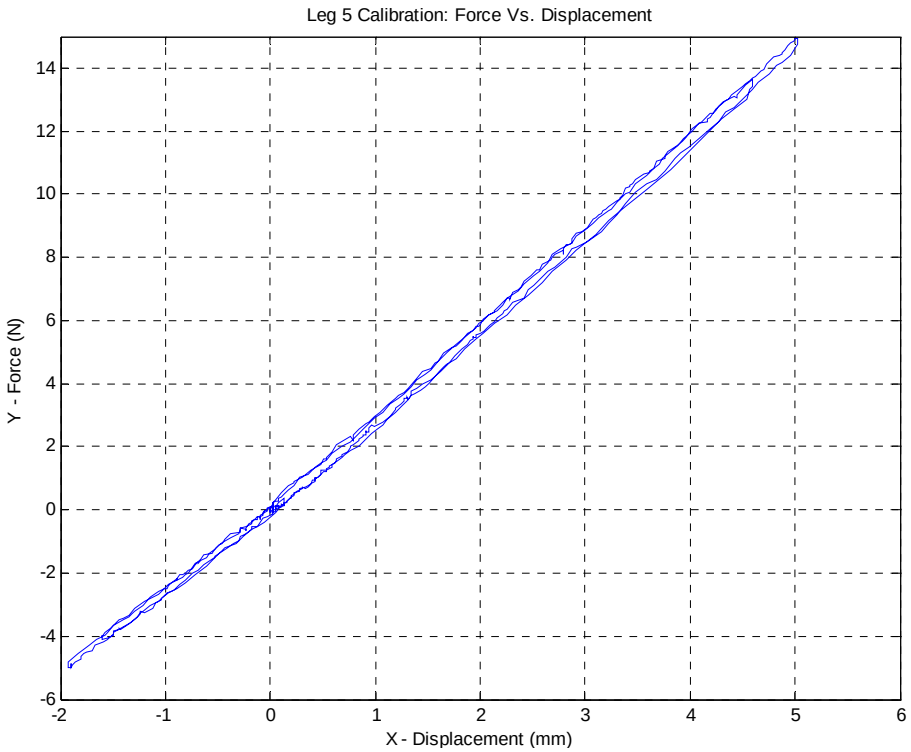

Figure 3.2a.15. Calibration plot for leg-5.

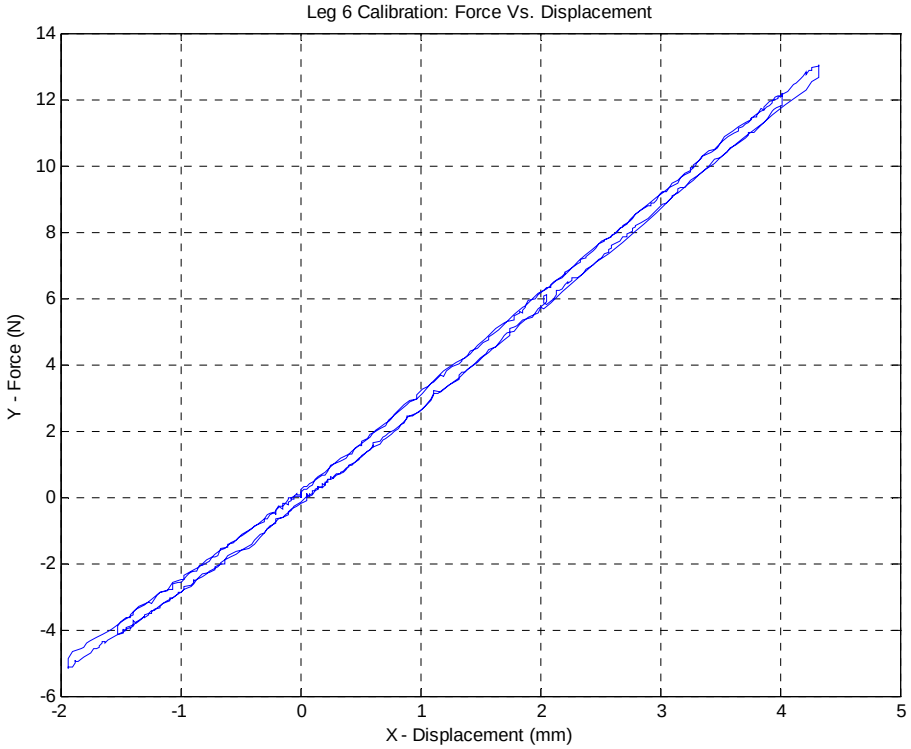

Figure 3.2a.16. Calibration plot for leg-6.

3.2a.11 Parallel platform force/wrench testing experiment

The force/torque sensor has been factory calibrated, so only the resolution is listed here. The resolutions for force and torque are shown in the Table 3.2a. below:

Table 3.2a. 4. Force-torque sensor Resolution

Fx	Fy	Fz	Tx	Ty	Tz
0.1 (N)	0.1 (N)	0.2 (N)	5 (N-mm)	5 (N-mm)	5 (N-mm)

The parallel platform is attached on the top of the force/torque sensor and its mass center is carefully balanced such that its weight is directly over the origin of the reference coordinate system. This coordinate system is based on the force/torque sensor, so there is no moment introduced. This z-direction bias force is easily eliminated in the sampling program, so it will not be discussed further.

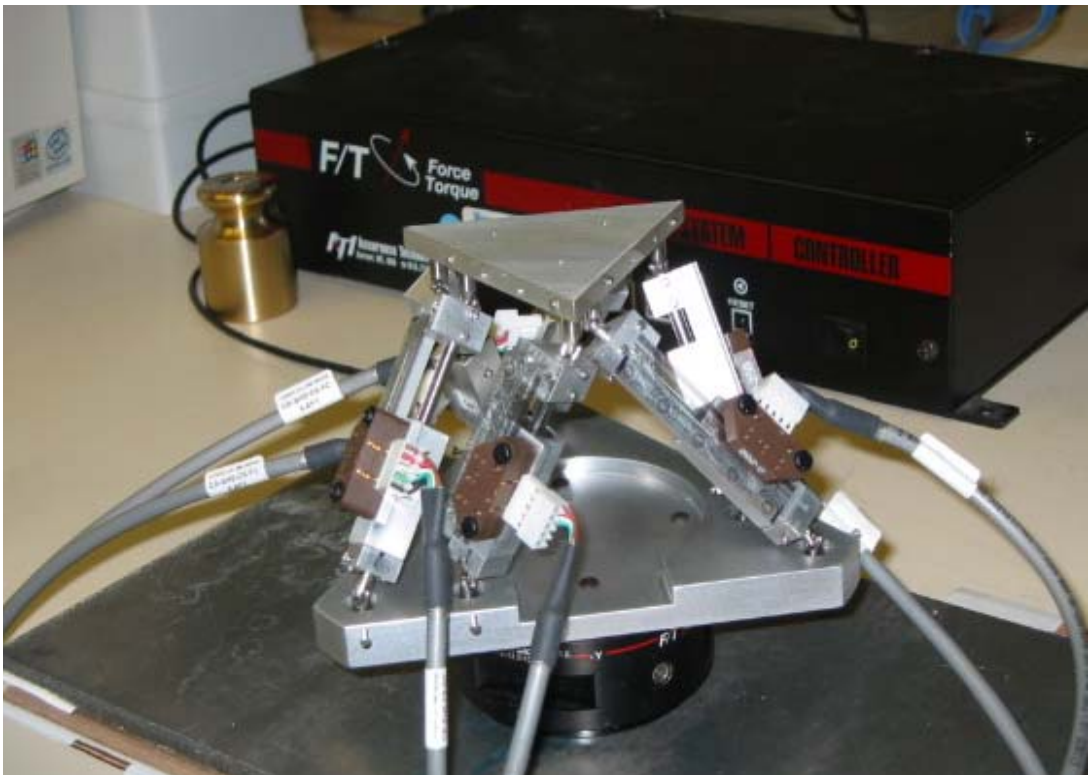

Figure 3.2a.17. Photo of the testing experiment for the parallel platform

The home position refers to the position of the platform when it is attached with the force/torque sensor and placed horizontally, with no other force applied on the top platform or any leg. The home position is also called initial position/ orientation, and it can be specified by its relative displacement from the encoder's indexed position. Before use, it is necessary to home the device. This is done by applying some small force/ wrench to the top platform, so each leg pass through its index position. Thus after homing, the current position and orientation can be accurately measured even when it is not in its home position.

3.2a.12 Repeatability Test

It is important to know the repeatability of the manipulator. The previous prototype, built by Tyler, did not have a good repeatability. Significant friction in the spherical joints was noted when an external force is applied and then removed. This friction impacted the ability of the top platform to return repeatedly to the same home position when external loading was removed.

In order to test its repeatability, two sets of experiment are performed.

Apply random force/wrench to the top plate and then remove it, measure the unloaded position/ orientation via the leg lengths measurements

Apply a weight of 500 grams on the top plate several times, and compare the measured leg lengths.

Table 3.2a.5. Repeatability experiment, method 1 (Encoder Counts)

Test Number	Leg 1	Leg 2	Leg 3	Leg 4	Leg 5	Leg 6
#1	-1	0	0	0	0	-1
#2	0	0	-1	1	2	-1
#3	-6	0	-4	-6	1	-3
#4	-5	2	0	-4	3	-1
#5	-3	-3	-1	-1	-2	-1
#6	-2	0	-1	0	2	2
Average	-2.83333	-0.16667	-1.16667	-1.66667	1	-0.83333
STD	2.316607	1.602082	1.47196	2.73252	1.788854	1.602082

Table 3.2a.6. Repeatability experiment, method 2 (Encoder Counts)

Test Number	Leg 1	Leg 2	Leg 3	Leg 4	Leg 5	Leg 6
#1	-200	-64	-5	-103	101	98
#2	-202	-65	-5	-104	101	100
#3	-207	-66	-5	-104	101	102
#4	-197	-63	-4	-100	100	97
#5	-203	-66	-5	-102	101	98
#6	-202	-65	-4	-103	100	101
Average	-201.833	-64.8333	-4.66667	-102.667	100.6667	99.33333
STD	3.311596	1.169045	0.516398	1.505545	0.516398	1.966384

The experiment results are shown in Table 3.2a.s 5 and 6. The numbers in the column shows the encoder counts when there is no external load applied (for method 1) and when the external load is applied on the platform (for method 2). The overall repeatability for the parallel platform is reasonable.

3.2a.13 Forward Analysis Verification

The forward kinematic analysis was presented in previous section. An experiment is shown here to validate the analysis result and also to provide for the static analysis process.

The parallel platform has some external force/ wrench applied on the top plate. The counts of the relative displacement for each leg is recorded

Table 3.2a.7, Forward analysis

	Leg 1	Leg 2	Leg 3	Leg 4	Leg 5	Leg 6
Encoder Counts	-15	-10	-2	-13	-26	-19

Leg length for special 6-6 (measured) (mm)	80.588	67.746	80.918	67.669	80.308	67.517
Leg length for the equivalent 3-3 platform (mm)	84.595	84.829	84.722	84.145	84.469	80.588
Leg length for the 6-6 platform (reverse analysis) (mm)	80.587	67.746	80.918	67.669	80.309	67.517

From the Table 3.2a.7, it is clear that the forward analysis is very accurate, the leg lengths calculated from the reverse analysis, which are also based on the results of the forward kinematic analysis, are very close to the leg length values measured by the optical encoder.

The coordinate systems of the parallel platform are shown in Figure 3.2a.18. The base points are $O_0, P_0,$ and Q_0, the origin of the 1st coordinate system is at point O_0, P_0 is on the X axis and Q_0 is on the XY plane. This coordinate system is fixed with the base and also called the base coordinate system. The top plate corner points are R_1, S_1, T_1, the origin of the 2nd coordinate system is at point R_1, S_1 is on the x axis, and T_1 is in the xy plane.

After finding the leg lengths of the equivalent 3-3 platform by the geometrical conversion, the position and orientation of the platform can be calculated by the forward kinematic analysis. For this specific configuration, the forward analysis has 8 solutions. Four are above the base and four are reflected through the base. The four configures above the base is discussed here. Each solution can be represented by a 4×4 transformation matrix. The first three elements in the fourth column have units of length (mm) and all other elements are dimensionless. From now on, the units for the element in the transformation matrices are omitted.

1.) $$\begin{bmatrix} 0.5105 & -0.1095 & 0.8529 & 29.2029 \\ -0.8598 & -0.0718 & 0.5055 & 52.4117 \\ 0.0059 & -0.9914 & -0.1308 & 59.4408 \\ 0 & 0 & 0 & 1 \end{bmatrix}$$

2.) $$\begin{bmatrix} 0.5021 & 0.8648 & 0.0007 & 29.7107 \\ -0.8648 & 0.5020 & 0.0007 & 52.1185 \\ 0.0058 & -0.0042 & 0.9999 & 59.4469 \\ 0 & 0 & 0 & 1 \end{bmatrix}$$

3.) $\begin{bmatrix} 0.4987 & 0.8668 & 0.0061 & 29.9149 \\ 0.1211 & -0.0627 & -0.9907 & 52.0006 \\ -0.8583 & 0.4947 & -0.1363 & 59.4478 \\ 0 & 0 & 0 & 1 \end{bmatrix}$

4.) $\begin{bmatrix} -0.3526 & 0.3757 & -0.8570 & 80.9928 \\ -0.3670 & 0.7869 & 0.4960 & 22.5108 \\ 0.8608 & 0.4894 & -0.1396 & 8.1510 \\ 0 & 0 & 0 & 1 \end{bmatrix}$

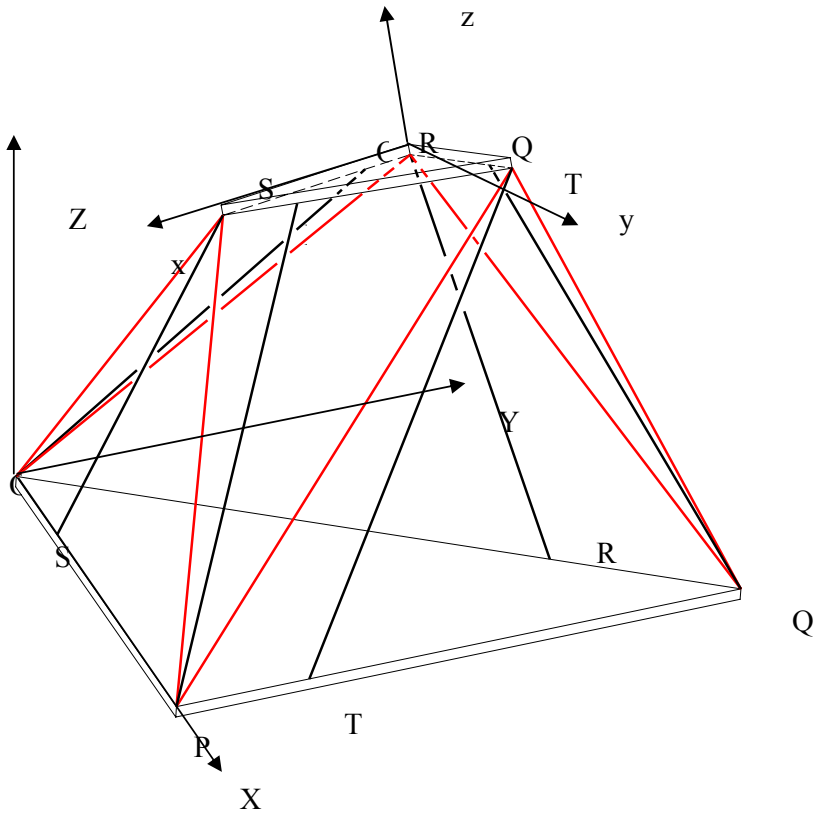

Figure 3.2a.18, Coordinate systems of the parallel platform

Although all four solutions are real and satisfy the geometrical conditions, there is only one solution that corresponds to the current configuration. With these transformation matrices, the coordinates of all points of the 3-3 structure can be determined. Then drawings of these configurations (or the numerical determination of the configuration closest to the most previous pose) can be used to choose the correct solution set.

Here the geometrical meanings of the 4×4 transformation matrices are used to make the selection. By using homogeneous coordinates, the 4×4 transformation matrix can be represented as

$$ {}^{A}_{B}\mathbf{T} = \begin{bmatrix} & {}^{A}_{B}\mathbf{R} & & {}^{A}\mathbf{P}_{B_0} \\ 0 & 0 & 0 & 1 \end{bmatrix}, \qquad (45) $$

where ${}^{A}\mathbf{P}_{B_0}$ is the location of the origin of the B coordinate system measured with respect to the A coordinate system, ${}^{A}_{B}\mathbf{R} = \begin{bmatrix} {}^{A}\mathbf{X}_B & {}^{A}\mathbf{Y}_B & {}^{A}\mathbf{Z}_B \end{bmatrix}$, its columns vectors are the orientation of the B coordinate system measured with respect to the A coordinate system. So by comparing the columns of the transformation matrices, the right solution can be properly selected.

The transformation matrix for the home position is given below as

$$ \begin{bmatrix} 0.5056 & 0.8628 & 0 & 29.6651 \\ -0.8628 & 0.5056 & 0 & 52.1547 \\ 0 & 0 & 1 & 59.9987 \\ 0 & 0 & 0 & 1 \end{bmatrix} $$

Clearly, the second solution is the correct one. For all other solutions, the coordinate systems have too much rotation relative to the base coordinates system. For example for solution 3, the third column vector is the homogeneous coordinates of the z axis with respect to the base coordinate. Its z axis is now almost parallel to the Y axis of the base coordinate system, which means a rotation of about 90 degree. This is not feasible according to the working space of the parallel platform and the physical restrictions.

The force/ wrench measurement test results are shown below. It should be pointed out that the F/T sensor has a left-hand reference system, while for the passive parallel platform system; a normal right-hand reference system is used. For the two reference systems, their X and Z directions are parallel but their Y axes are anti-parallel.

Table 3.2a. 8. Numerical example for force/wrench measurement.

	Fx(N)	Fy(N)	Fz(N)	Tx(Nmm)	Ty(Nmm)	Tz(Nmm)
F/T sensor	-0.1	0.2	-9.8	-59.0	-194.8	-8.5
PCCFC	-0.0408	-0.3928	-10.4423	-57.5069	193.4776	-14.0031

Table 3.2a. 9. Numerical example for force/wrench measurement.

	Fx(N)	Fy(N)	Fz(N)	Tx(Nmm)	Ty(Nmm)	Tz(Nmm)
F/T sensor	0.1	0	-9.8	-107.3	240.1	0
PCCFC	-0.0548	-0.0592	-10.6214	-130.2283	-257.7749	-3.1451

Table 3.2a.10. Numerical example for force/wrench measurement.

	Fx(N)	Fy(N)	Fz(N)	Tx(Nmm)	Ty(Nmm)	Tz(Nmm)
F/T sensor	-0.2	0.1	-9.9	237.3	-31.1	-5.7
PCCFC	-0.1837	-0.3545	-10.7676	247.0074	38.5972	-13.9355

Table 3.2a. 11. Numerical example for force/wrench measurement.

	Fx(N)	Fy(N)	Fz(N)	Tx(Nmm)	Ty(Nmm)	Tz(Nmm)
F/T sensor	3.3	-2.5	-10.5	-310.5	-401.1	-144.1
PCCFC	3.9684	2.8410	-10.7859	-289.6161	406.1201	-171.8185

Table 3.2a.12. Numerical example for force/wrench measurement.

	Fx(N)	Fy(N)	Fz(N)	Tx(Nmm)	Ty(Nmm)	Tz(Nmm)
F/T sensor	1.8	1.9	-9.2	420.8	-254.2	-276.8
PCCFC	2.0173	-2.3872	-9.9014	417.9422	258.8412	-332.5946

3.2a.14 References

- [Ciblak 99] Ciblak, N., and Lipkin, H., "Synthesis of Cartesian Stiffness for Robotic Applications," in Proc. IEEE Int. Conf. Robotics and Automation, pp. 2147–2151, 1999.
- [Crane 01] Crane, C.D., and Duffy, J., Class Notes: Screw Theory and its Application to Spatial Robot manipulators, CIMAR, MAE, University of Florida, Gainesville, FL, 2001
- [Dasgupta 2000] Dasgupta, B., Mruthyunjaya, T.S., "The Stewart Platform Manipulator: A Review", Mechanism and Machine Theory, Vol 35, pp. 15~40, 2000
- [Duffy 96] Duffy, Joseph, "Statics and Kinematics with Applications to Robotics", Cambridge University press, USA, 1996
- [Dwarakanath 2000]Dwarakanath, T., and Crane, C., "In-Parallel Passive Compliant Coupler for Robot Force Control", Proceedings of the ASME Mechanisms Conference, Baltimore, 2000
- [Gaillet 83] Gaillet, A and Reboulet, C., "An Isostatic Six Component Force and Torque Sensor", Proc. 13th Int. Symposium on Industrial Robotics. 1983
- [Griffis 89] Griffis, M., and Duffy, J., "A Forward Displacement Analysis of a Class of Stewart Platforms", Journal of Robotic Systems 6(6), pp. 703-720, 1989
- [Griffis 91a] Griffis, M., Kinestatic control: A Novel Theory for Simultaneously Regulating Force and Displacement, Ph.D. Dissertation, University of Florida, Gainesville, FL, 1991.
- [Griffis 91b] Griffis, M., and Duffy, J., "Kinestatic Control: A Novel Theory for Simultaneously Regulating Force and Displacement", Trans. ASME Journal of Mechanical Design, Vol. 113, No. 4, pp. 508-515 ,1991
- [Griffis 93] Griffis, M., and Duffy, J., "Method and Apparatus for Controlling Geometrically Simple Parallel Mechanisms with Distinctive Connections", United States Patent, Patent Number 5,179,525, Jan.12, 1993.
- [Huang 98] Huang, S., The Analysis and Synthesis of Spatial Compliance, PhD dissertation, Marquette Univ., Milwaukee, WI, 1998.
- [Hunt 93] Hunt K.H. and Primrose E.J.F., "Assembly Configurations of Some In-Parallel Actuated Manipulators", Mechanism and Machine Theory, 28(1), pp. 31-42, 1993.
- [Hunt 98] Hunt, K.H., and McAree, P. R., "The Octahedral Manipulator: Geometry and Mobility," The International Journal of Robotics Research, Vol. 17, No. 8, pp. 868-885, 1998.
- [Lee 94] Lee, J., "An Investigation of A Quality Index for The Stability of In-Parallel Planar Platform Devices," Master Dissertation, University of Florida, Gainesville, FL, 1996.
- [Lee 98] Lee, J., Duffy, J., and Hunt K., "A Practical Quality Index Based On The Octahedral Manipulator," International Journal of Robotic Research, Vol.17 (10), pp. 1081-1090, 1998.
- [Lee 2000] Lee, J., Investigation of Quality Indices of In-Parallel Platform Manipulators and Development of Web Based Analysis Tools, PhD Dissertation, University of Florida, Gainesville, FL, 2000.
- [Lin 90] Lin, W., Duffy, J., and Griffis, M., "Forward Displacement Analysis of the 4-4 Stewart Platforms", in Proc. 21st Biennial Mech. Conf. ASME, Chicago, Vol. DE-25, pp. 263-269, 1990.
- [Merlet 92] Merlet, Jean-Pierre, "Direct Kinematics and Assembly Models of Parallel Manipulators", International Journal of Robotics Research, 11(2), pp.150-162, 1992.
- [Merlet 2000] Merlet, Jean-Pierre, Parallel Robots, Kluwer Academic Publishers, Netherlands, 2000

- [Patterson 93] Patterson, T. and H. Lipkin, "Structure of Robot Compliance", ASME Journal of Mechanical Design, 115(3), pp. 315-322, 1993.
- [Pigoski 98] Pigoski, T., Griffis, M., and Duffy, J., "Stiffness Mappings Employing Different Frames of Reference", Mech. Mach. Theory Vol.33, No.6. pp. 825-838, 1998.
- [Raghavan 93] Raghavan, M., "The Stewart Platform of General Geometry has 40 Configurations", Trans ASME J Mech. Trans. Automat Des Vol. 115, pp. 277~282, 1993.
- [Roberts 2000] Roberts, R.G., "Minimal Realization of an Arbitrary Spatial Stiffness Matrix with a Parallel Connection of Simple and Complex Springs", IEEE Trans. on Robotics and Automation, Vol. 16(5), pp. 603-608, 2000.
- [Shannon 2002] Shannon Ridgeway, Research Proposal, University of Florida, Gainesville, FL, 2002.
- [Tasi 99] Tasi, Lung-Wen, Robot Analysis, the Mechanics of Serial and Parallel Manipulators, John Wiley& Sons, USA, 1999
- [Zhang 04] Zhang, Bo, Crane, Carl, 'Special Singularity Analysis for a 6-DOF Parallel Platform', 10th International conference on robotics & remote systems for hazardous environments, Gainesville, FL, USA, 2004.

3.2b Geometric Stability of Parallel Platform Based Manipulators

3.2b.1 Objective

This research concentrates on the geometric stability of parallel platform based manipulators. The aim is to develop a reconfigurable device that can attain any desired compliance matrix relationship (the compliance matrix relates the displacement of the top of the platform to the force/torque applied to the top of the platform). A variable-damping device will be designed and built to adjust the damping of the connectors in real-time. The best candidate device used to achieve variable-damping is the magnetorheological (MR) damper.

3.2b.2 Background

Parallel kinematic manipulators have received a lot of attention due to their distinct advantages over their serial counterparts. They have six serial kinematic chains (connectors) giving them greater load carrying capacity, higher stiffness, and redundancy in motion which make them more tolerant to individual actuator positioning errors. These advantages make them ideal for precision positioning applications. However, many of these applications are located in environments where certain degrees of disturbances exist. These disturbances in the form of vibrations degrade the performance of the sensitive instruments which are essential for precision positioning. Therefore, it is a priority to create a vibration-free environment to enable precision positioning. To design a whole system free of vibrations is not a viable solution as this will be extremely costly and is usually not feasible. Therefore, the disturbances need to be eliminated at the interfaces between either the vibration source and the main structure or the main structure and the sensitive equipment used for precision applications as shown in Figure 3.2b.1. From a design perspective, it would be logical to have a hexapod which is inherently an ideal mechanism for precise positioning provide vibration isolation at the same time.

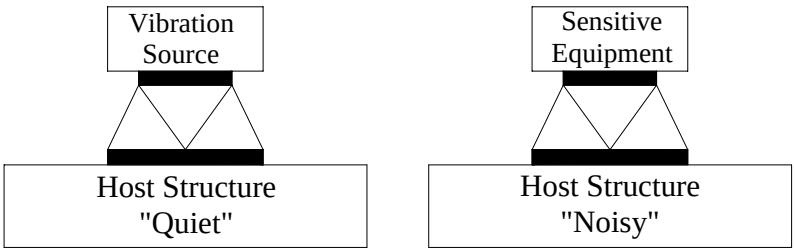

Figure 3.2b.1: Two possible cases of isolation

The proposed theoretical 6-axis hexapod model will use a combination of passive and semi-active control for vibration isolation. Here different models of the connector legs will be investigated.

3.2b.2.1 Basic Connector Model

In this simple model of the connector shown in Figure 3.2b.2, m_p is the payload mass and m_c is the lumped mass of the connector and the moving parts of the actuator. The deformation of the connector and the actuator friction are represented by the spring and dashpot, respectively. The parameters and variables used in this model are

x_p, the displacement of the payload;

x_c, the displacement of the moving part of the actuator;

k_1, the equivalent stiffness of the connector;

c_1, the actuator friction and damping, modeled as a viscous damper, and

F_A, the force generated by the actuator.

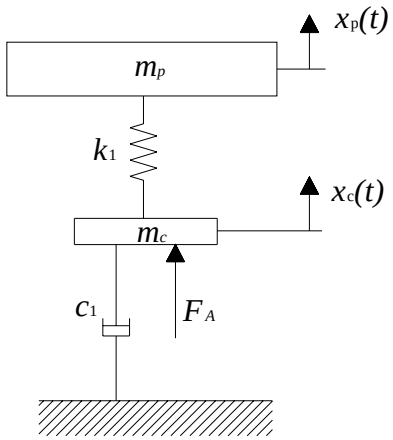

Figure 3.2b.2: Basic connector model

The force exerted by the connector to the payload is a function of the displacement and the stiffness of the connector

$$F = k_1 \cdot (x_p - x_c) \qquad (2.1)$$

When the actuator is rigidly coupled to the platform, in other words, when k_1 is very high, any damping required for vibration control must be provided by the active control of the actuator. The dynamic behavior of the system is then determined by the dynamic response of the actuator and controller. The main disadvantage of this is that the dynamic response of the

actuator may not match the desired dynamic performance of the system. Also, all the energy will be dissipated by the actuator. This can overheat the actuator. Furthermore, the power efficiency of the system is reduced when active devices (actuator) are used to simulate passive ones (spring, damper) (Baiges-Valentin, 1996).

3.2b.2.2 Connector Model with Coupling Stage

A coupling stage may be introduced to eliminate the problems of the first model described above. The coupling stage is shown in Figure 3.2b.3. The additional components are

k_2, the stiffness element in the coupling stage and

c_2, the viscous damping element in the coupling stage.

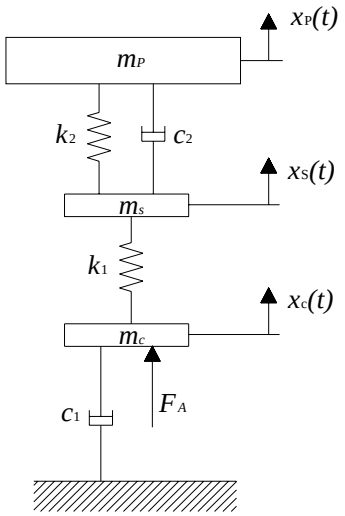

Figure 3.2b.3: Connector model with coupling stage

The displacement of the spring in the coupling stage can be controlled to generate a force. The force applied by the connector to the payload is a function of the coupling stage displacement and velocity, and also the coupling stage stiffness and damping coefficients:

$$F = k_2(x_p - x_s - x_c) + c_2(\dot{x}_p - \dot{x}_s - \dot{x}_c) \qquad (2.2)$$

The coupling spring stiffness is much lower than the connector stiffness. Therefore, most of the deflection occurs in the coupling stage. The main disadvantage of this model is that when the actuator applies a force, the coupling stage has to deform before this force can be transferred to the payload and this introduces a delay and degrades the dynamic performance. The damping element attenuates some of the high-frequency vibrations, but it also increases the reaction time

of the system. Also, some of the energy provided by the actuator is dissipated in the damper instead of being transmitted to the payload) (Baiges-Valentin, 1996).

3.2b.2.3 Connector Model with Decoupling Stage

In order to eliminate high-frequency vibrations which are transmitted to the actuator through the connector stiffness element, a decoupling stage is introduced to the model as shown in Figure 3.2b.4. Additional components are:

k_3, the stiffness element in the decoupling stage,

c_3, the viscous damping element in the decoupling stage, and

m_d, the mass of the decoupling stage.

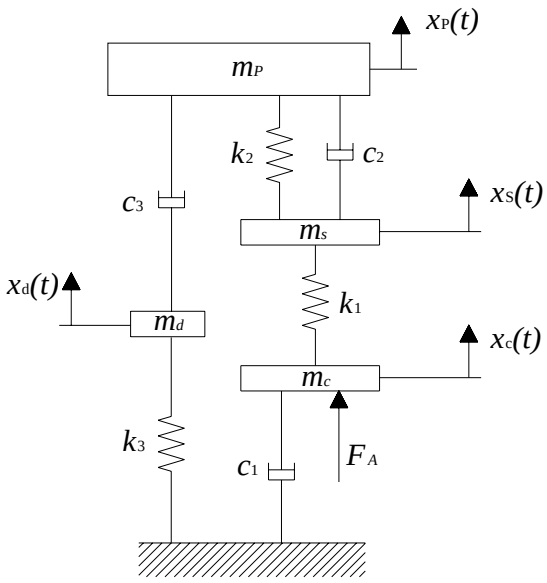

Figure 3.2b.4: Connector model with coupling stage

Unlike the coupling stage damper, the decoupling stage damper will not transmit the disturbances to the actuator and it will be used to attenuate high-frequency vibrations. The decoupling stage stiffness needs to be very high as it will be supporting the decoupling stage damper. If it is not stiff enough, the decoupling stage will deform the spring instead of the damper dissipating energy. The force applied by the connector to the payload is a combination

of the force generated in the coupling and decoupling stages. This force is a function the displacement and velocity of the coupling stage and the velocity of decoupling stage:

$$F = k_2(x_p - x_s - x_c) + c_2(\dot{x}_p - \dot{x}_s - \dot{x}_c) + c_3(\dot{x}_d) \qquad (2.3)$$

The problem with this model is that the decoupling stage damper will always be dissipating energy, both from the disturbance and from the actuator. In the latter case, some of the energy of the actuator which would normally be used to move the payload will be dissipated in the damper. The decoupling stage will also increase the overall mass and inertia of the connector (Baiges-Valentin, 1996; Hauge and Campbell, 2004).

3.2b.2.4 Semi-Active Connector Model with Decoupling Stage

It would be desirable to combine the advantages of the models above in one model. At low frequencies, the model with no decoupling stage provides minimum energy loss. However, at high frequencies, it does not provide enough energy dissipation and the decoupling stage is necessary. A connector with optimal performance at both low-frequencies and high-frequencies can be achieved by varying the amount of damping in both the coupling and decoupling stage dampers as shown in Figure 3.2b.5. A magnetorheological damper is an ideal candidate for this purpose. When maximum current is applied, the damping will be very high. The damper will be blocked and will behave essentially as a rigid element. When there is no magnetic field, the damper will act as a low energy dissipating device.

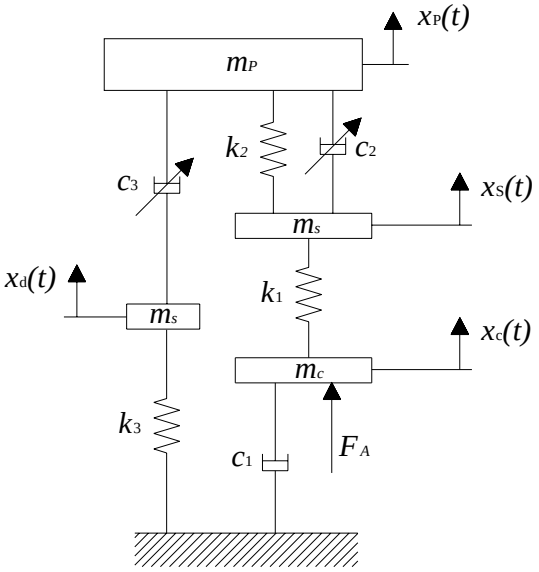

Figure 3.2b.5: Connector model with variable damping elements

For the low-frequency mode, the decoupling stage must be deactivated. Therefore, there will be no current being applied to the decoupling stage damper. Only a small amount of energy will be dissipated here. The current being applied to the coupling stage may be adjusted depending on the amount of damping desired here.

For the high-frequency mode, the coupling stage needs to be deactivated. The coupling stage damper will be blocked in this case and the coupling stage will behave essentially as a rigid element as shown in Figure 3.2b.6. The damping coefficient of the decoupling stage would be set to a desirable value.

When the connector is to be used only for positioning and no vibration isolation is required, both the coupling stage and decoupling stages may be deactivated by blocking the coupling stage damper and applying no current to the decoupling stage damper. In this case, the model would ideally look like the one shown in Figure 3.2b.2.

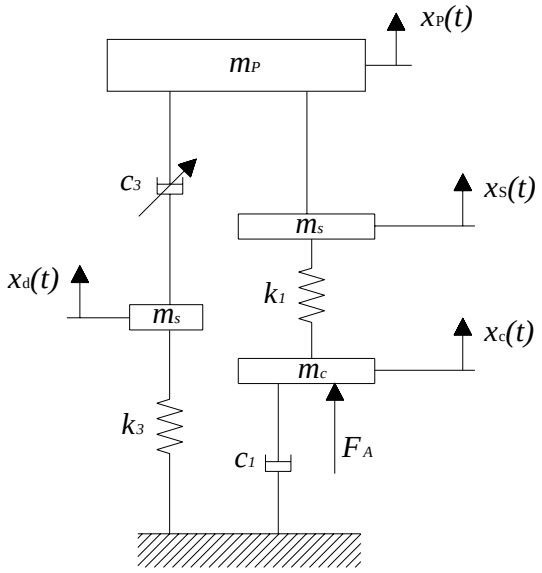

Figure 3.2b.6: High-frequency mode with the coupling stage damper blocked

3.2b.2.5 Magnetorheological (MR) Technology

Semi-active control has recently been an area of much interest because of its potential to provide the adaptability of active devices without requiring a significant external power supply for actuators. A semi-active control system cannot provide energy to a system comprising the structure and actuator, but by altering the properties of the system, such as stiffness and damping, it can achieve favorable results (Dyke *et al*, 1996). Unlike an active system, the control forces developed are related to the motion of the structure. Furthermore, the stability of the semi-active

system is guaranteed as the control forces typically oppose the motion of the structure (Scruggs and Lindner, 1999).

The robustness and the simple mechanical design of magnetorheological (MR) dampers make them a natural candidate for a semi-active control device. They require minimal power while delivering high forces suitable for full-scale applications. They are fail-safe since they behave as passive devices in case of a power loss (Symans and Constantinou, 1997). The focus of this report is to review models that effectively predict the behavior of magnetorheological devices while giving preliminary test results from an MR damper designed and built.

MR fluids are suspensions of small iron particles in a base fluid. They are able to reversibly change from free-flowing, linear viscous liquids to semi-solids having a controllable yield strength under a magnetic field. When the fluid is exposed to a magnetic field, the particles form linear chains parallel to the applied field as shown in Figure 3.2b.7. These chains impede the flow and solidify the fluid in a matter of milliseconds. This phenomenon develops a yield stress which increases as the magnitude of the applied magnetic field increases (Jolly *et al*, 1998).

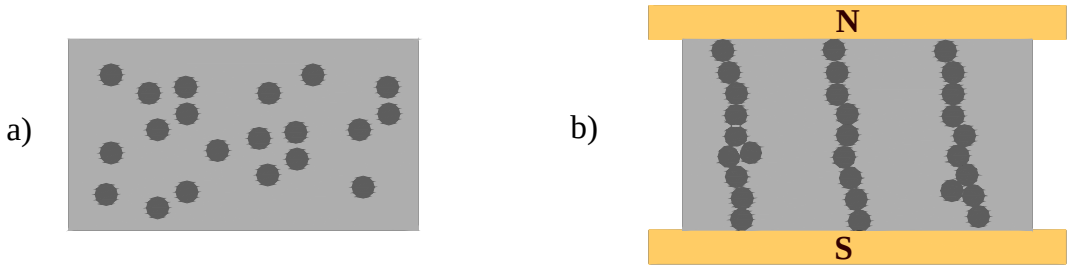

Figure 3.2b.7: Magnetorheological fluid: a) no magnetic field, b) with magnetic field

A magnetic circuit is necessary to induce the changes in the viscosity of the MR fluid. The magnetic circuit typically uses low carbon steel, which has a high magnetic permeability and saturation. This steel effectively directs magnetic flux into the fluid gap. In an optimal design, magnetic field energy in the fluid gap is kept at a maximum while the energy lost in steel flux conduit and regions of non-working areas is minimized. This requires the total amount of steel in the magnetic circuit to be minimized. However, sufficient cross-section of steel must be maintained such that the magnetic field intensity in the steel is very low.

Several different designs of MR dampers have been built and tested in the past. The first of these designs is the bypass damper where the bypass flow occurs outside the cylinder and an electromagnet applies a magnetic field to the bypass duct (Sunakoda *et al*, 2000 ; Sodeyama *et*

al, 2003). While this design has a clear advantage that the MR fluid is not directly affected by the heat build-up in the electromagnet, the presence of the bypass duct makes it a less compact design. In another design by the Lord Corporation, the electromagnet is inside the cylinder and the MR fluid passes through an annular gap around the electromagnet. This design uses an accumulator to make up for the volume of fluid displaced by the piston rod which is going into the damper (Snyder and Wereley, 1999; Snyder *et al*, 2001). A way to get rid of this accumulator and simplify the design is to build a double-shafted damper (Yang *et al*, 2002). However, all of these dampers were intended for large-scale applications, mostly for the vibration isolation of structures. A linear, double-shafted MR damper with a simple design which can be used for small-scale applications is the focus of this research.

3.2b.3. Approach

Three MR damper prototypes that were designed, built, and tested are described and the preliminary experiment results are presented. The designs of various MR dampers commercially available and in the literature are carefully studied as a starting point for the designs within this work. Changes and modifications are made in order to come up with a better design. The following parameters are considered during the process:

1. Ease of manufacturing and simplicity in design.
2. Friction. The major cause of friction in an MR damper is the contact between the seals and the housing or the shaft depending on the design. Also, in the case when the moving shaft is not properly aligned, there may be contact between the shaft and other metal surfaces.
3. Size and weight.
4. The placement of the coil and the wiring. Depending on the design, the coil may either be placed inside the housing where the only barrier separating it from the MR fluid is its coating or it may be outside the housing or the bypass duct if there exists one.

3.2b.3 MR Damper Prototypes

3.2b.3.1 Double-Shafted Damper with Aluminum Housing

This design is based on a commercial damper, SD-1000 MR damper by the Lord Corporation and is shown in Figure 3.3.1. The damper operates in a combination of valve and direct shear modes. The fluid passes through an annular orifice between the coil bobbin and an inner cylinder. A magnetic field is created along this gap through the use of the coil. When the magnetic field is applied, the viscosity of the magnetorheological fluid increases in a matter of milliseconds. The field causes a resistance to the flow of fluid between the two reservoirs. This way, the damping coefficient of the damper is adjusted. Therefore, the damping coefficient of the damper can be adjusted by feeding back a conditioned sensor signal to the coil.

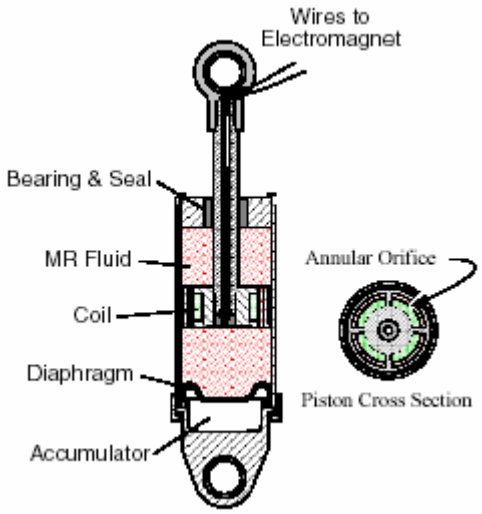

Figure 3.3.1: SD-1000 MR Fluid damper by the Lord Corporation

A Teflon seal around the inner cylinder as shown in Figure 3.3.2b prevents the flow of the fluid between the housing and the inner cylinder. A hollow shaft enables the wires to deliver current to the electromagnet. Since the flux lines do not pass through the outer housing, the housing may be built out of aluminum which makes a reduction in the overall weight of the damper possible. The original design was modified to have two shafts and therefore the accumulator which compensated for the volume of fluid displaced by the shaft going into the damper was no longer necessary.

This design had several disadvantages. First of all, the Teflon seal created a significant amount of additional friction. Secondly, it was observed that the magnetic body did not remain

centered during operation which caused sealing malfunction and leaking, scratching of the insulation of the coil, and asymmetry in the annular gap which may result in non-uniform temperature increases. Finally, since the coil was inside the fluid, the fluid was directly affected by the heat build-up in the coil. An increase in the temperature of the MR fluid causes its viscosity to drop and reduces the force capacity of the damper (Dogrouz *et al.*, 2003).

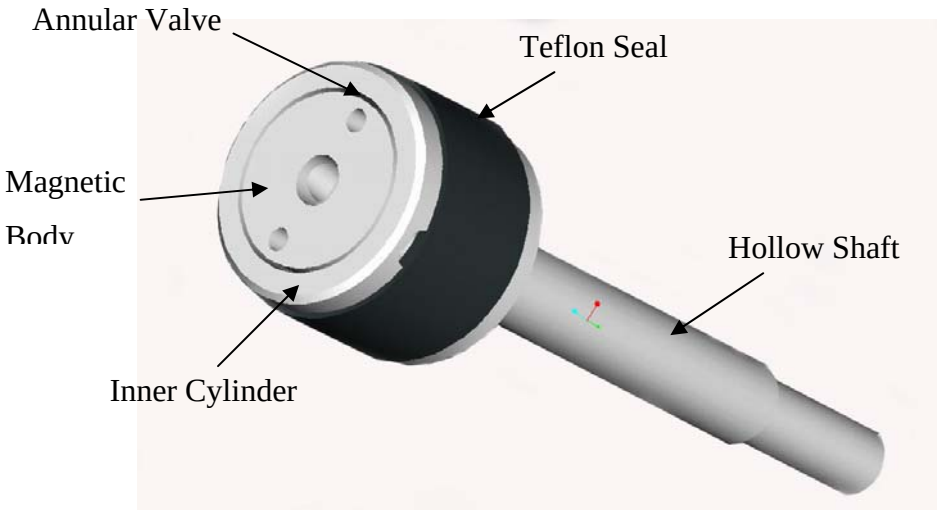

Figure 3.3.2b: Interior of damper with Teflon seal

3.2b.3.2b Double-Shafted Damper with Steel Housing

This damper is also double-shafted. However, in this design, unlike the previous one, there is no additional inner cylinder between the magnetic body and the outer housing as shown in Figure 3.3.3. The outer housing is made up of low carbon steel. Therefore the flux lines pass through the housing in their return path while the magnetorheological fluid flows through the annular gap between the housing and the magnetic body around which the coil is wound as seen in Figure 3.3.4.

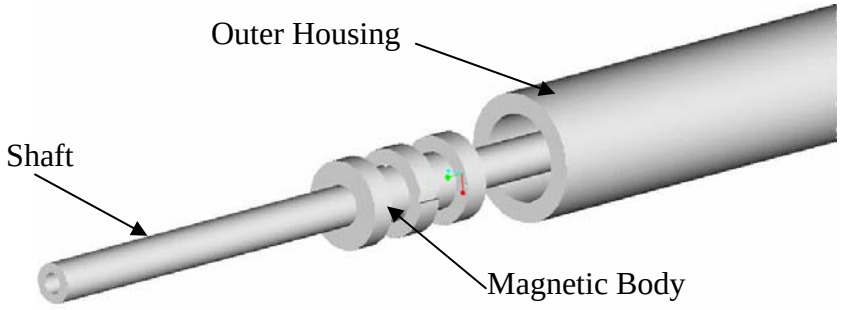

Figure 3.3.3: Schematic of the double-shafted damper with steel housing

The magnetic body was designed to divide the coil into two parts which creates three effective magnetic surfaces. The two coils were wound in directions opposite to each other so that the flux lines would add up in the middle, as shown in Figure 3.3.4.

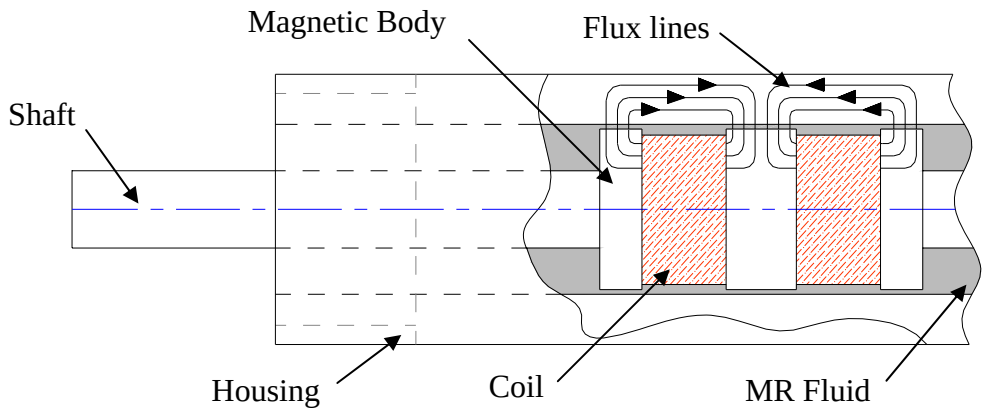

Figure 3.3.4: Schematic of the double-shafted MR damper

All the parts of this damper were manufactured from low-carbon steel which has a high magnetic permeability which is shown in Figure 3.3.5. This damper was heavier than the previous one since it was made out of steel and not aluminum. However, it has a simpler design as the inner cylinder and the Teflon seal is not used. Instead of the inner cylinder, the outer housing itself serves as the return path of the flux lines. It was observed that the overall friction in the damper was lower due to the fact that the Teflon seal was not used. The performance of this damper also suffered from heat build-up in the coil and the fact that the magnetic body did not remain centered during the operation.

Figure 3.3.5: Low-carbon steel housing of the double-shafted MR damper

3.2b.3.3 Syringe Type Damper with Parallel Rod

The idea of this design was born from a demonstration device by the Lord Corporation. This device is simply made of two syringes connected together by a plastic hollow cylinder through which the fluid flows from one syringe to the other. When a permanent magnet is attached onto the hollow cylinder, it causes the fluid in the cylinder to turn to semi-solid and therefore stops the flow which in turn blocks the motion of the syringes.

Several similar syringe devices were built, using two syringes and a hollow aluminum rod for the valve as displayed in Figure 3.3.6. Magnet wire was wrapped around the aluminum rod and differing valve and housing dimensions were tested.

Figure 3.3.6: Syringe dampers with varying housing and valve dimensions

An aluminum housing was built to resemble the two syringes connected with a hollow rod as shown in Figure 3.3.7. In this design, a parallel rod is connected to both of the shafts so that a vacuum will not be created when either one of the shafts is pulled back. The main advantage of this design is that the coil is not inside the housing which makes the wiring much simpler where as in the previous two designs, the wiring needed to be sealed against contact with the fluid. The MR fluid is also not affected as much from the heat build-up in the coil.

It is clear that the asymmetrical design of this prototype will induce bending moments on the shafts. Therefore, in the next design, the parallel rod was replaced by a hollow cylinder that encloses the entire damper.

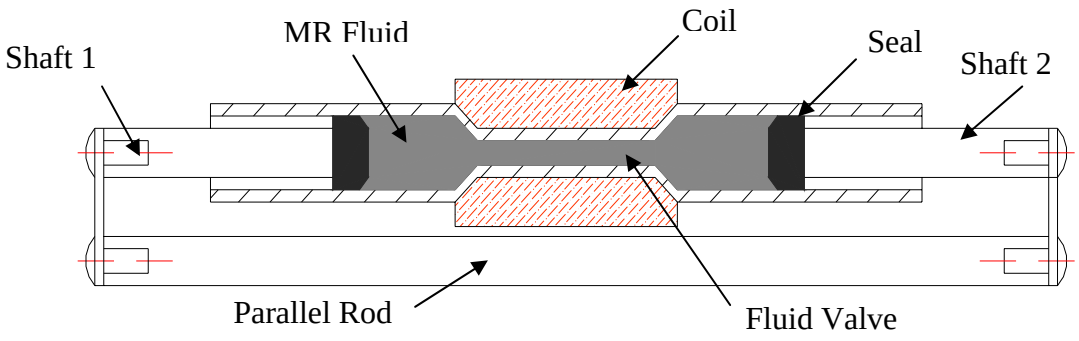

Figure 3.3.7: Syringe type damper with parallel rod

3.2b.3.4 Syringe Type Damper with Cylindrical Outer Housing

The difference between this design and the previous one is the addition of an aluminum hollow cylinder which serves the same purpose of the parallel rod in the previous design and connects the two shafts as shown in Figure 3.3.8.

On one side, the two base rods are connected to the extension rod. On the other side, shaft 1 is attached to the force transducer (PCB 208C02) which is connected to the shaker through the stinger. When the shaker is excited, shaft 1 moves. Shaft 2 moves with shaft 1 since they are connected together through the outer housing. Meanwhile, the inner housing is motionless as it is connected to the extension rod which is fixed. An accelerometer (PCB 333B4) is attached to the housing using wax.

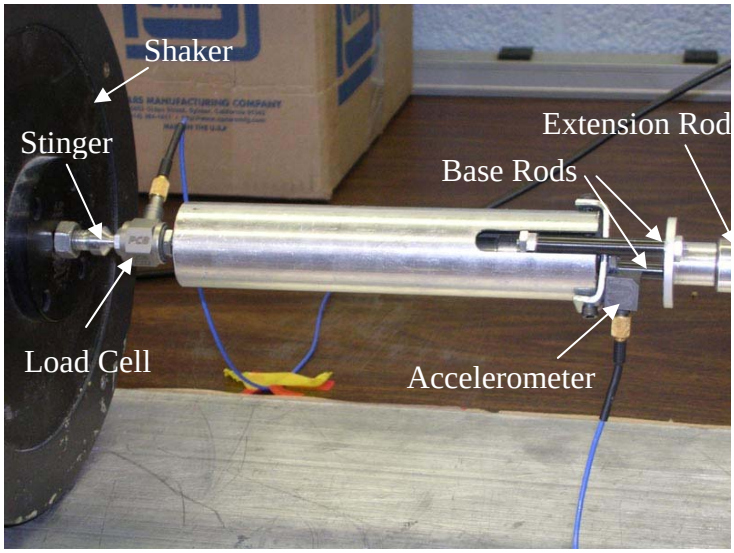

Figure 3.3.8: Syringe type damper with cylindrical outer housing with a) exploded view showing the inner housing and the coil; b) view of the fully assembled damper

3.2b.3.5 Results

3.2b.3.5.1 Shaker Tests

Preliminary tests were conducted on the vibration isolator setup described above. The syringe type damper was tested under varying shaker excitation amplitudes, frequencies and input current. The results show that there is only a slight increase in the damping force when a magnetic field is applied. In Figure 3.3.9, the increase in the damping force is shown when the input current is increased from 0 to 0.5A.

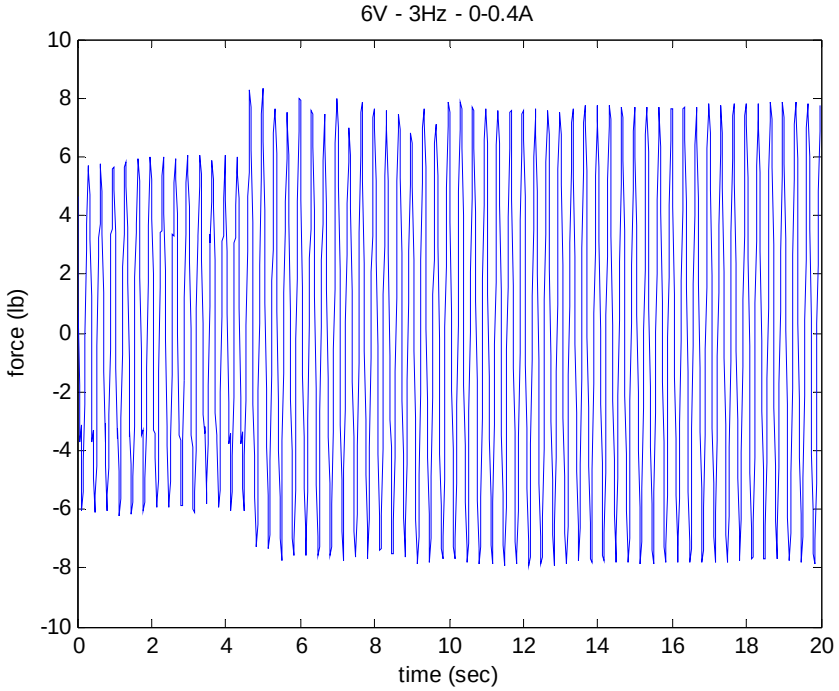

Figure 3.3.9: Increase in force for the syringe type damper when the input current is increased from 0 to 0.5 A at 3 seconds

3.2b.3.5.2 Tension Tests

Preliminary tests were conducted on an Instron universal tester to determine the force characteristics of the double-shafted damper with steel housing. Figures 3.10 and 3.11 show the results of tension tests carried out. The force versus displacement plot shown in Figure 3.3.10 was obtained from data at velocity 5 in/min for a 1.5 in. displacement of the stroke. For velocities 1, 2, 3, 4, and 5 in/min, the damping force generated by the damper was measured for varying magnitudes of the applied current and the results are displayed in Figure 3.3.11. It was noted that a significant increase in the damping force did not occur for currents above 0.4A due

to saturation of the coil. Therefore, the maximum damping force that can be generated by this damper is approximately 40 lb.

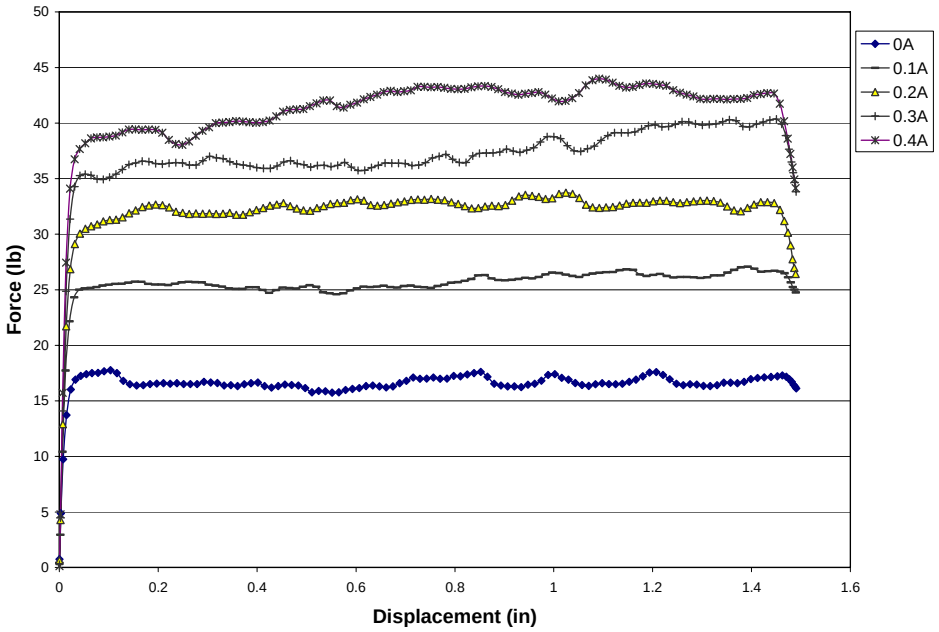

Figure 3.3.10: Force-displacement curves for varying current at 5 in/min

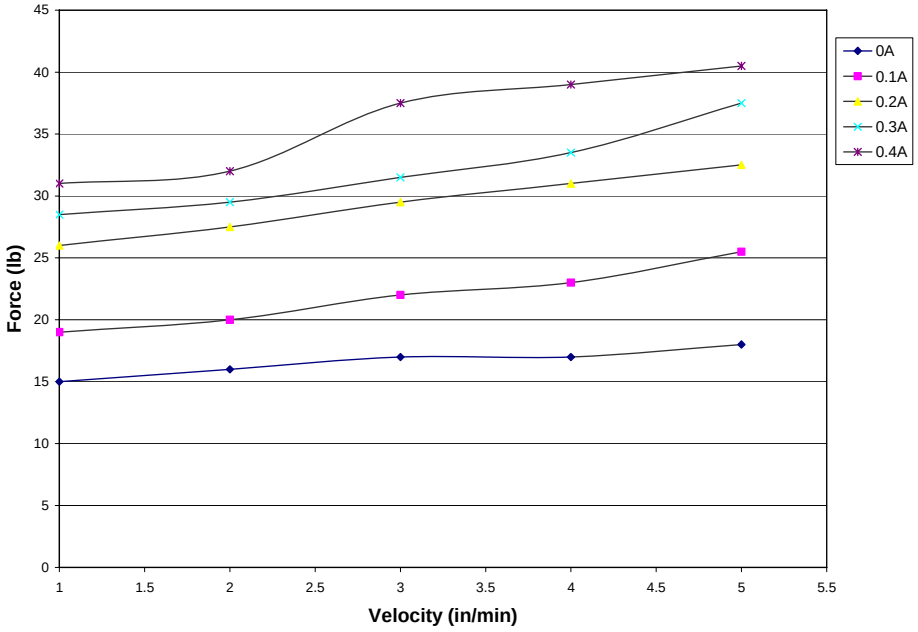

Figure 3.3.11: Force-velocity curves for varying current

3.2b.3.6 References:

- Baiges-Valentin, I., "Dynamic modeling of parallel manipulators," Ph.D. dissertation, University of Florida, Mechanical Engineering Department, Gainesville, Florida, 1996.
- Dogrouz, M. B., Wang, E. L., Gordaninejad, F., and Stipanovic, A. J., "Augmenting heat transfer from fail-safe magneto-rheological fluid dampers using fins," *Journal of Intelligent Material Systems and Structures*, v 14 n 2 February 2003 p 79-86, 2003.
- Dyke, S. J., Spencer, B. F., Sain, M. K., and Carlson, J. D., "Experimental Verification of Semi-Active Structural Control Strategies Using Acceleration Feedback", *Proceedings of the 3rd International Conference on Motion and Vibration Control*, September 1-6, Chiba, Japan, Vol. III, pp. 291-296, 1996.
- Hauge, G. S. and Campbell, M. E., "Sensors and control of a space-based six-axis vibration isolation system," *Journal of Sound and Vibration*, v 269 n 3-5 Jan 22 2004 p 913-931, 2004.
- Jolly, Mark R., Bender, Jonathan W., and Carlson, J. David, "Properties and Applications of Commercial Magnetorheological Fluids," *Proceedings of SPIE - The International Society for Optical Engineering*, Vol. 3327, pp. 262-275, 1998.
- Scruggs, J. and Lindner, D., "Active Energy Control in Civil Structures," *Proceedings of the SPIE - The International Society for Optical Engineering*, Newport Beach, CA, Vol. 3671, pp. 194-205, 1999.
- Snyder, R.A., and Wereley, N. M., "Characterization of a Magnetorheological Fluid Damper Using a Quasi-Steady Model," Proceedings *of the 1999 Smart Structures and Materials - Smart Structures and Integrated Systems* Newport Beach, CA, USA, 1999.
- Snyder, R. A., Kamath, G. M., and Wereley, N. M., "Characterization and Analysis of Magnetorheological Damper Behavior Under Sinusoidal Loading," *AIAA Journal* Vol. 39 n 7, pp. 1240-1253, July 2001.
- Sodeyama, H., Sunakoda, K., Fujitani, H., Soda, S., Iwata, N., and Hata, K., "Dynamic Tests and Simulation of Magneto-Rheological Dampers," *Computer-Aided Civil and Infrastructure Engineering* Vol. 18 n 1, pp. 45-57, January 2003.
- Sunakoda, K., Sodeyama, H., Iwata, N., Fujitani, H., and Soda, S., "Dynamic Characteristics of Magneto-Rheological Fluid Damper," *Proceedings of SPIE - The International Society for Optical Engineering* Vol. 3989 Society of Photo-Optical Instrumentation Engineers, USA, pp. 194-203, 2000.
- Symans, M.D. and M.C. Constantinou, "Experimental Testing and Analytical Modeling of Semi-Active Fluid Dampers for Seismic Protection," *Journal of Intelligent Material Systems and Structures*, Vol. 8, No. 8, pp. 644-657, August 1997.
- Yang, G., Spencer, Jr., Carlson, J. D., and Sain, M. K., "Large-Scale MR Fluid Dampers: Modeling and Dynamic Performance Considerations," *Engineering Structures* Vol. 24 n 3, pp. 309-323, March 2002.

3.2c Adaptive Compliant Force Control Mechanism Design

3.2c.1. Objective of Research

The objective of the research is to design a compliant mechanism that can be attached to the end of a robot manipulator where the device can be reconfigured to achieve any desired compliance matrix as specified by the user. The compliance matrix relates the change in contact force to the change in relative position of the top and bottom platforms of the device. An adaptive device, whose compliance matrix can be specified, will allow the device to be applied to a wide variety of manipulation tasks where the required compliance is different for each task. This adaptive device is in effect a 'multi-purpose' tool.

3.2c.2 Background

It is almost impossible to imagine the world without robots. Robots are in general fast, accurate, and robust. They have been employed successfully in arc welding, painting, and other applications which do not involve the interaction between the robot and the environment and require only position control schemes. There are many operations involving contacts of man and machine or the robot and its environment and a small amount of positional error of the robot system, which is almost inevitable, may cause serious damages to the robot or the object with which it is in contact. Compliant couplings which may be inserted between the end effecter and the last link of the robotic manipulator can be a solution to this problem. Compliant couplings can be employed for force control applications by using the theory of Kinestatic Control which was proposed by Griffis [1991]. A small twist applied to the compliant coupling generates a small change of the wrench which the compliant coupling exerts on the environment. This relation is well described by the stiffness matrix of the compliant coupling. Kinestatic control varies the position of the last link of the manipulator to control the position and contact force of the distal end of the robotic manipulator at the same time with the compliance of the coupling in mind.

Compliant couplings have been used to aid assembly tasks. RCC (Remote Center of Compliance) devices which typically have a diagonal stiffness matrix are one of the most successful compliant couplings and are mainly used to compensate positional errors during tasks such as inserting a peg into a chamfered hole (see Whitney [1982] and Figures 3.2c.1 and 2). Even assembly tasks such as inserting a peg into a chamfer-less hole may be carried out successfully with a compliant coupling which has a fixed appropriate stiffness matrix (see Peshkin [1990]).

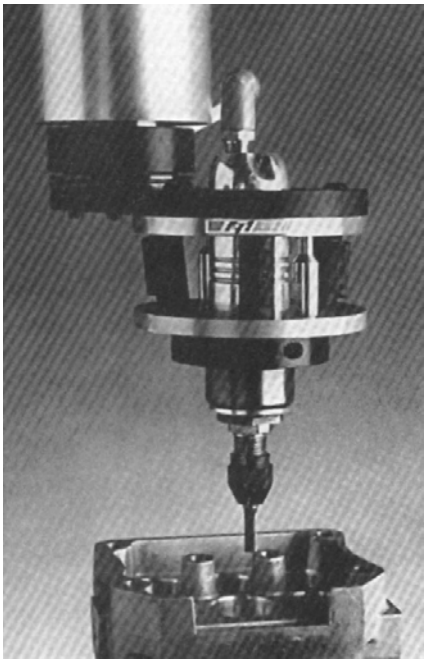

Figure 3.2c.1. Compliant coupling attached between the end effecter and the last link of robotic system.

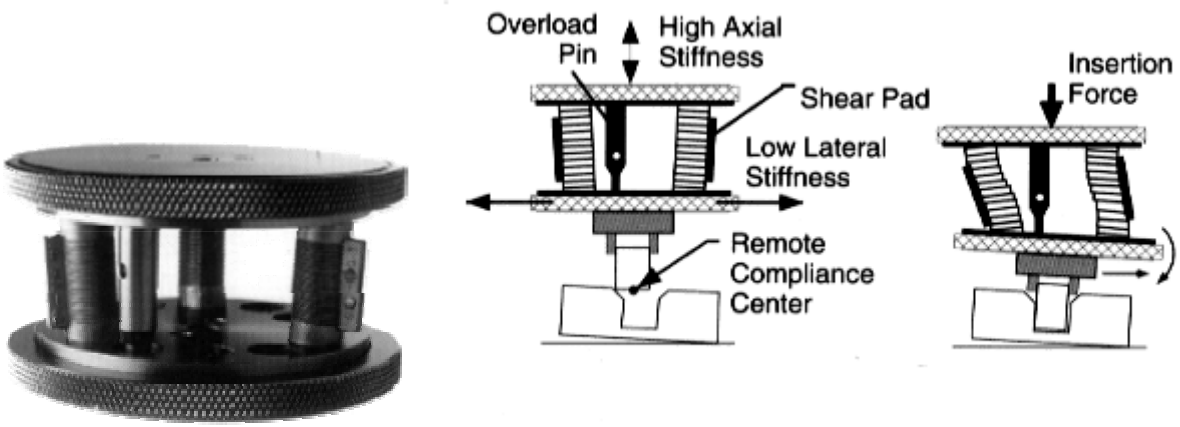

Figure 3.2c.2. RCC device and its working principle (from ATI Industrial Automation)

RCC devices typically have a specific operation point. If the length of the peg to be inserted is changed, a different RCC device should be employed to do insertion tasks unless the RCC device has variable compliance. Although not considered in the research of Peshkin [1990], a variable compliant coupling can make once impossible tasks possible. In addition, each force control task may have an optimal stiffness matrix. With variable compliant couplings, several different tasks involving different force ranges can be accomplished without having to physically change the compliant coupling. Variable compliant couplings also can improve the performance of humanoid robot parts such as ankles and wrists (see Figure 3.2c.3). With variable compliant mechanisms,

specific stiffness matrices can be implemented according to the humanoid robot's actions such as walking, running, or jumping.

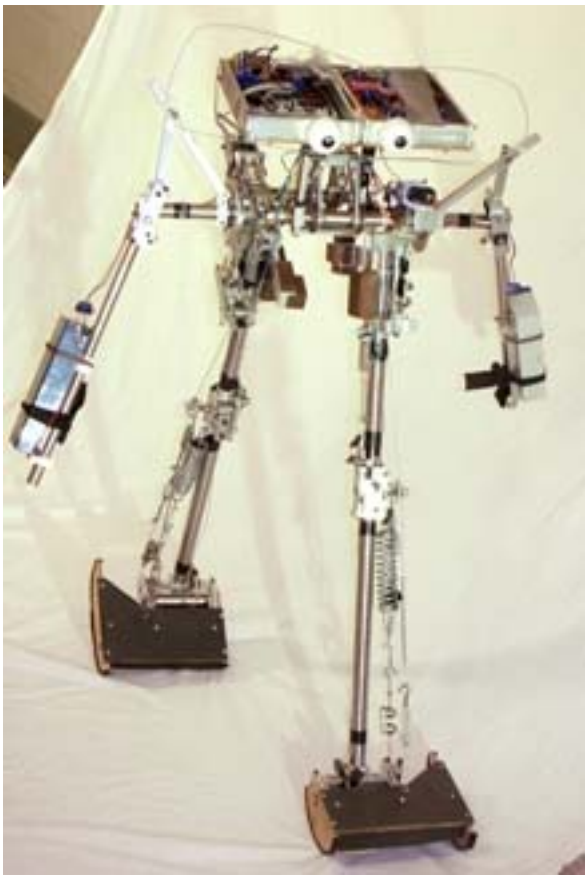

Figure 3.2c.3. Cornell passive-dynamic, powered robot (from Cornell University)

3.2c.3 Literature Review

3.2c.3.1 Stiffness Matrix

Screw theory, which was introduced by Ball [1900], is employed throughout this report to describe the motion of rigid bodies and the forces applied to rigid bodies. The compliance of a mechanism can be well described by a stiffness matrix which is 6 × 6 for a spatial mechanism and 3 × 3 for a planar mechanism. Using screw theory, Dimentberg [1965] studied properties of an elastically suspended body. Loncaric [1985] used Lie groups rather than screw theory to study symmetric spatial stiffness matrices of compliant mechanisms assuming that the springs are in an equilibrium position and derived a constraint that makes the number of independent elements of symmetric 6 × 6 stiffness matrices 20 rather than 21. Griffis [1991] obtained a global stiffness model for parallel mechanism-based compliant couplings where he used the term global to state

that the springs are not restricted to an unloaded equilibrium position. Griffis [1991] also showed that the stiffness matrix is not symmetric when the springs are deflected from the equilibrium positions due to an external wrench. Ciblak and Lipkin [1994] decomposed a stiffness matrix into a symmetric and a skew symmetric part and showed the skew symmetric part is negative one-half the externally applied load expressed as a spatial cross product operator. Parallel mechanism-based compliant couplings have been investigated by a number of researchers to realize a desired stiffness matrix because of its high stiffness, compactness, and small positional errors. Huang and Schimmels [1998] obtained the bounds of the stiffness matrix of parallel mechanism-based couplings which consist of simple elastic devices and proposed an algorithm for synthesizing a realizable stiffness matrix with at most seven simple elastic devices. Roberts [1999] and Ciblak and Lipkin [1999] independently developed algorithms for implementing a realizable stiffness matrix with r number of springs where r is the rank of the stiffness matrix. As for serial robot manipulators, Salisbury [1980] derived the stiffness mapping between the joint space and the Cartesian space. Chen and Kao [2000] showed that the formulation of Salisbury [1980] is only valid in the unloaded equilibrium pose and derived the conservative congruence transformation for stiffness mapping accounting for the effect of an external force.

3.2c.3.2 Variable Compliant Couplings

Planar/spatial compliant couplings are in general constructed with multiple simple springs. The stiffness matrix of the coupling depends on the geometry of the coupling and the stiffness constants and free lengths of the constituent springs. To realize variable compliant couplings, variable geometry or adjustable springs have been investigated. Simaan and Shoham [2002] studied the stiffness synthesis problem using a variable geometry planar mechanism. They changed the geometry of the base using sliding joints on the circular base (see Figure 3.2c.4). Ryan et al [1994] designed a variable spring by changing the effective number of coils of the spring for adaptive-passive vibration control (see Figure 3.2c.5).

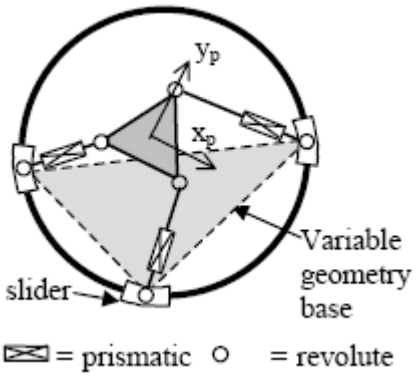

Figure 3.2c.4. Planar robot with variable geometry base platform (from Simaan and Shoham [2002])

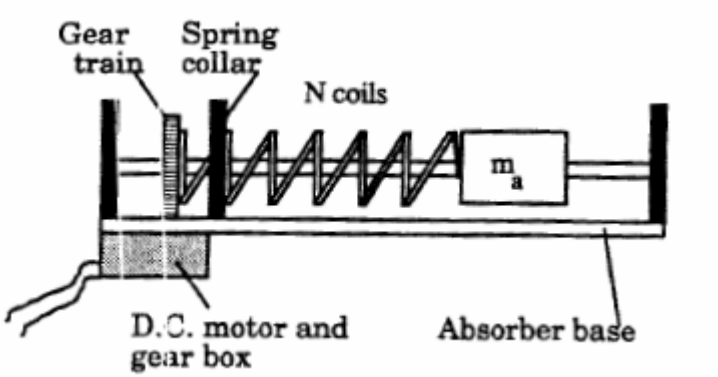

Figure 3.2c.5. Adaptive vibration absorber (from Ryan et al [1994])

Cantilever beam-based variable compliant devices have been studied by a few researchers. Under an external force, a cantilever beam deflects and its deflection depends on the length of the beam and the Young's modulus of the material. Henrie [1997] investigated a cantilever beam which is filled with magneto-rheological material and changed the Young's modulus by changing the magnetic field. McLachlan and Hall [1999] devised a programmable passive device by changing the length of the cantilever beam as shown in Figure 3.2c.6.

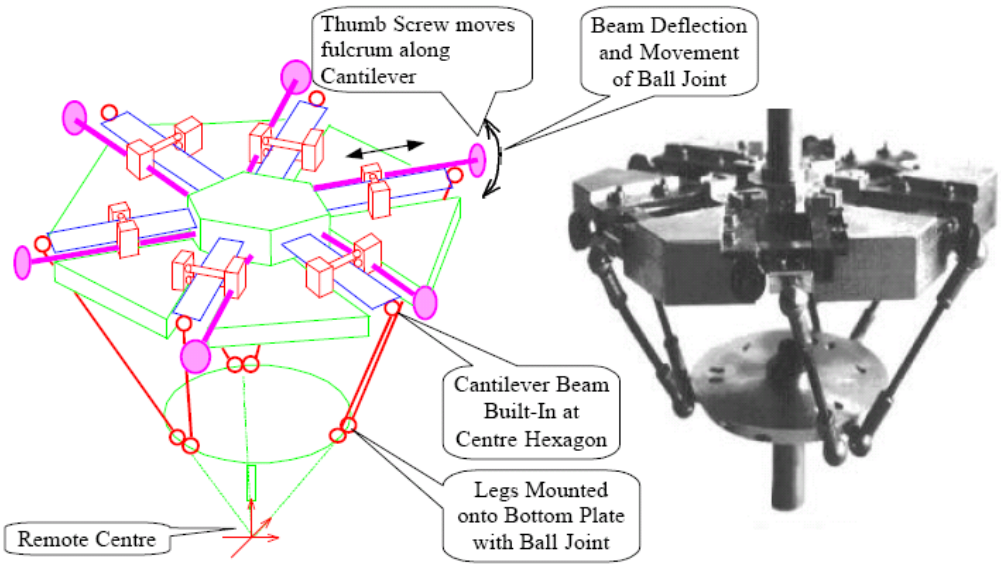

Figure 3.2c.6. Parallel topology 6DOF with adjustable compliance (from McLachlan and Hall [1999])

3.2c.4 Approach

Variable planar/spatial compliant mechanisms consisting of multiple simple adjustable springs will be investigated. Because parallel mechanism-based couplings can not realize arbitrary stiffness matrices, a more complicated mechanism which has multiple simple adjustable springs in serial and/or parallel arrangements will be investigated. An example of complicated planar compliant coupling is shown in Figure 3.2c.7. A stiffness mapping of a simple linear spring connecting two moving bodies will be derived for planar and spatial cases. This stiffness mapping will lead to the derivation of the stiffness matrix of complicated mechanisms. The compliant couplings will not be restricted to be in unloaded equilibrium configuration. The relation between the stiffness matrix and the constituent springs' stiffness constants and free lengths will be studied and will be applied to implement variable planar/spatial compliant couplings.

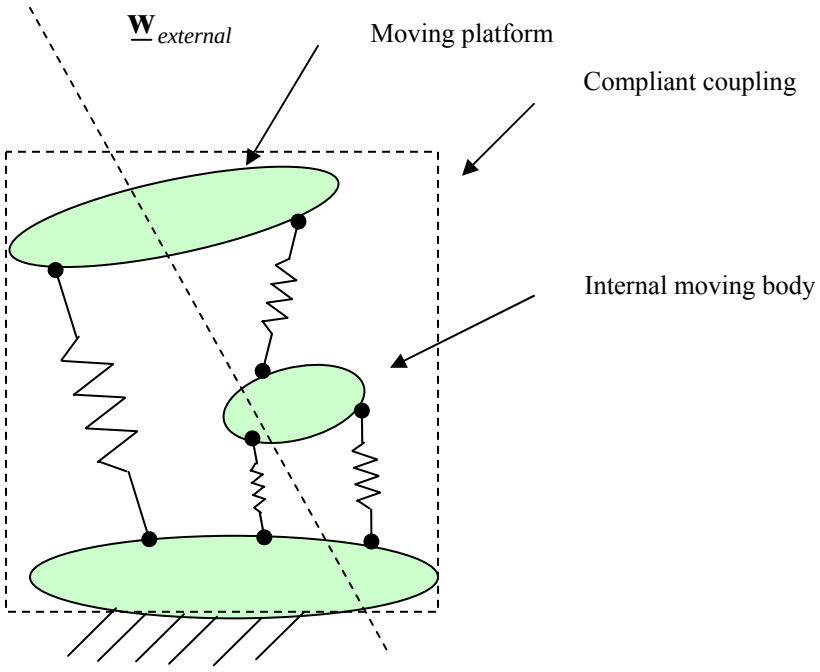

Figure 3.2c.7. A complicated compliant coupling and an external wrench.

When a rigid body supported by a compliant coupling moves, the deflection and the directional change of the coupling may lead to a change of the force. In this report, a stiffness mapping model which maps a small twist of the body into the corresponding wrench variation is studied. To describe a small (or instantaneous) displacement of a rigid body and a force/torque applied to a body, the concepts of *twist* and *wrench* from screw theory are used throughout this report (see Ball [1990] and Crane [2003]). Further, the notations of Kane and Levinson are also employed (see Kane and Levinson [1985]) to describe spatial motions of rigid bodies.

Specifically, as part of the notation, the position of a point P embedded in body B measured with respect to a reference system embedded in body A will be written as ${}^{A}r_{P}{}^{B}$. The derivative of the displacement of this point P (embedded in body B in terms of a reference coordinate system embedded in body A) is denoted as ${}^{A}\delta\underline{\mathbf{r}}_{P}^{B}$. The derivative of an angle of body B with respect to a body A is denoted by ${}^{A}\delta\underline{\boldsymbol{\theta}}^{B}$ and its magnitude is denoted by ${}_{A}\delta\theta_{B}$. The twist of a body B with respect to a body A will be denoted by ${}^{A}\delta\underline{\mathbf{D}}^{B}$.

3.2c.5 Spring in a Line Space

A simple linear spring is depicted in Figure 3.2c.8. Body A is allowed to move only on a line along the axis of the spring which is attached between body A and ground. The spring has a spring constant k and a free length x_o. The position of body A can be expressed by a scalar x and the force from the spring by a scalar f.

The spring force can be written by

Equation Chapter 1 Section 1 $f = k(x - x_o)$. (1)

The relation between a small change of the position of body A and the corresponding small force variation can be obtained by taking a derivative of Eq. (1) as

$\delta f = k\delta x$. (2)

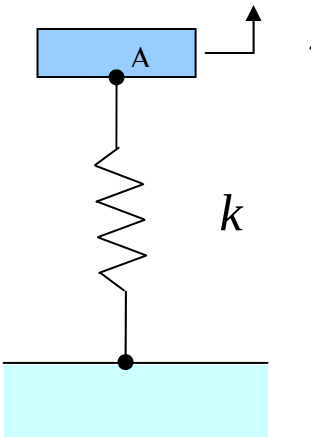

Figure 3.2c.8. Spring in a line space.

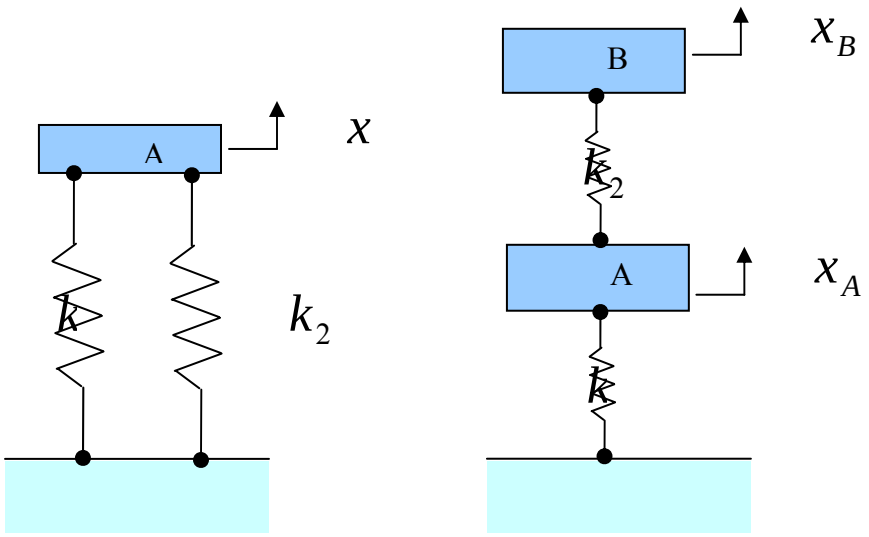

(a) (b)

Figure 3.2c.9. one-demensional spring arrangements. (a) parallel arrangement and (b) serial arrangement

When springs are attached in parallel as shown in Figure 3.2c.9 (a), the resultant spring constant k_R may be derived as Eq. (3).

$$\delta f = k_R \delta x = k_1 \delta x + k_2 \delta x$$

$$k_R = k_1 + k_2 \ . \quad (3)$$

For a serial arrangement as shown in Figure 3.2c.9 (b), the resultant spring constant k_R which maps a small change of position of body B into a small force variation upon body B may be written as Eq. (4).

$$\delta f = k_R \delta x_B = k_1 \delta x_A = k_2 \left(\delta x_B - \delta x_A \right)$$

$$\delta x_A = \frac{k_2}{k_1 + k_2} \delta x_B$$

$$k_R = \frac{k_1 k_2}{k_1 + k_2} \quad or \quad k_R^{-1} = k_1^{-1} + k_2^{-1} \ . \quad (4)$$

3.2c.6 Linear Planar Spring

In this section, a planar stiffness mapping is derived using the same method in Griffis [1991]. Figure 3.2c.10 depicts a rigid body and a linear compliant coupling connecting the body and the ground. The compliant coupling has a revolute joint at each end and a prismatic joint with a spring in the middle part. Body A can translate and rotate in a planar space.

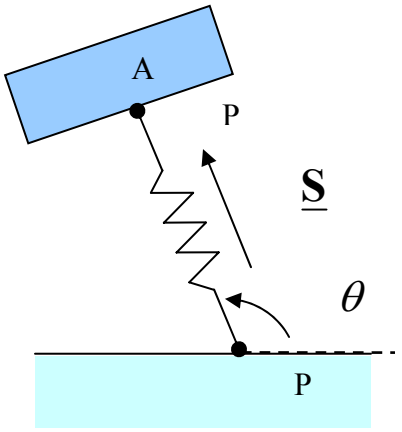

Figure 3.2c.10. Planar compliant coupling connecting body A and the ground

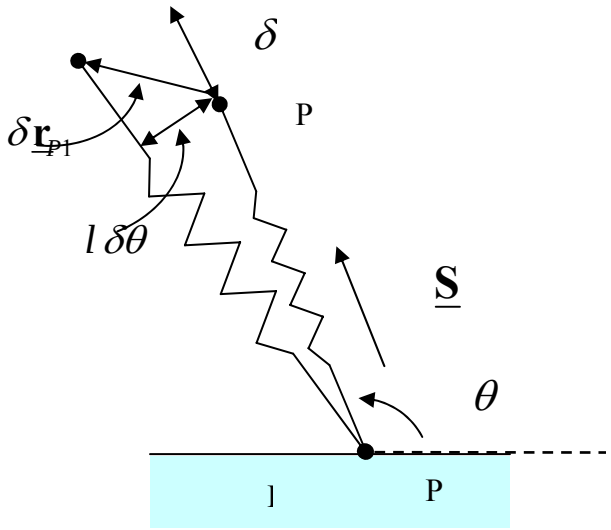

Figure 3.2c.11. Small change of position of P1 due to a small twist of body A

The force which the spring exerts on body A can be written as Eq. (5) and k, l, and l_o are the spring constant, current spring length, and spring free length of the compliant coupling, respectively.

$$\underline{\mathbf{f}} = k(l - l_o)\underline{\$} \quad (5)$$

where $\underline{\$}$ represents the unitized Plücker coordinates of the line along the compliant coupling which may be written by

$$\underline{\$} = \begin{bmatrix} \underline{\mathbf{S}} \\ {}^{E}\underline{\mathbf{r}}_{P0}^{E} \times \underline{\mathbf{S}} \end{bmatrix} = \begin{bmatrix} \underline{\mathbf{S}} \\ {}^{E}\underline{\mathbf{r}}_{P1}^{A} \times \underline{\mathbf{S}} \end{bmatrix} \quad (6)$$

where $\underline{\mathbf{S}}$ is the unit vector along the compliant coupling and ${}^{E}\underline{\mathbf{r}}_{P0}^{E}$ and ${}^{E}\underline{\mathbf{r}}_{P1}^{A}$ are the position of the pivot point PO in the ground body and that of P1 in body A, respectively, measured with respect to a reference coordinate system attached to ground. To obtain the stiffness mapping, a small twist ${}^{E}\delta\underline{\mathbf{D}}^{A}$ is applied to body A and the corresponding change of the spring force will be obtained. The twist ${}^{E}\delta\underline{\mathbf{D}}^{A}$ may be written by

$${}^{E}\delta\underline{\mathbf{D}}^{A} = \begin{bmatrix} {}^{E}\delta\underline{\mathbf{r}}_{0}^{A} \\ {}^{E}\delta\underline{\boldsymbol{\varphi}}^{A} \end{bmatrix} \qquad (7)$$

where ${}^{E}\delta\underline{\mathbf{r}}_{o}^{A}$ is the differential of the position of point O in body A which is coincident with the origin of the inertial frame E measured with respect to the inertial frame. ${}^{E}\delta\underline{\boldsymbol{\varphi}}^{A}$ is the differential of the angle of body A with respect to the inertial frame.

Taking a derivative of Eq. (5) with the consideration that $\underline{\$}$ is a function of θ in planar cases yields

$$\begin{aligned} \delta\underline{\mathbf{f}} &= k\delta l\underline{\$} + k(l - l_o)\delta\underline{\$} \\ &= k\delta l\underline{\$} + k(1 - \frac{l_o}{l})\frac{\partial\underline{\$}}{\partial\theta} l\,\delta\theta \end{aligned} \qquad (8)$$

where

$$\frac{\partial\underline{\$}}{\partial\theta} = \begin{bmatrix} \frac{\partial\underline{\mathbf{S}}}{\partial\theta} \\ {}^{E}\underline{\mathbf{r}}_{P0}^{E} \times \frac{\partial\underline{\mathbf{S}}}{\partial\theta} \end{bmatrix} \qquad (9)$$

and where $\frac{\partial\underline{\mathbf{S}}}{\partial\theta}$ is a unit vector perpendicular to $\underline{\mathbf{S}}$.

Using screw theory, the variation of position P1 can be written as

$${}^{E}\delta\underline{\mathbf{r}}_{P1}^{A} = {}^{E}\delta\underline{\mathbf{r}}_{o}^{A} + {}^{E}\delta\underline{\boldsymbol{\varphi}}^{A} \times {}^{E}\underline{\mathbf{r}}_{P1}^{A} \quad .(10)$$

It may be decomposed into two perpendicular vectors, one along $\underline{\mathbf{S}}$ and one along $\frac{\partial\underline{\mathbf{S}}}{\partial\theta}$. These vectors correspond to the change of the spring length δl and the change of the direction of the spring $l\delta\theta$ as shown in Figure 3.2c.11. The change in the position of point P1 may thus also be written as

$$
\begin{aligned}
{}^{E}\delta\underline{\mathbf{r}}_{P1}^{A} &= \left({}^{E}\delta\underline{\mathbf{r}}_{P1}^{A}\cdot\underline{\mathbf{S}}\right)\underline{\mathbf{S}} + \left({}^{E}\delta\underline{\mathbf{r}}_{P1}^{A}\cdot\frac{\partial\underline{\mathbf{S}}}{\partial\theta}\right)\frac{\partial\underline{\mathbf{S}}}{\partial\theta} \\
&= \delta l\,\underline{\mathbf{S}} + l\delta\theta\frac{\partial\underline{\mathbf{S}}}{\partial\theta}
\end{aligned}
\quad . \qquad (11)
$$

From Eqs. (10), (11), (6), and (7) expressions for δl and $l\delta\theta$ may be obtained as

$$
\begin{aligned}
\delta l &= {}^{E}\delta\underline{\mathbf{r}}_{P1}^{A}\cdot\underline{\mathbf{S}} = {}^{E}\delta\underline{\mathbf{r}}_{o}^{A}\cdot\underline{\mathbf{S}} + {}^{E}\delta\underline{\boldsymbol{\varphi}}^{A}\times{}^{E}\underline{\mathbf{r}}_{P1}^{A}\cdot\underline{\mathbf{S}} \\
&= {}^{E}\delta\underline{\mathbf{r}}_{o}^{A}\cdot\underline{\mathbf{S}} + {}^{E}\delta\underline{\boldsymbol{\varphi}}^{A}\cdot{}^{E}\underline{\mathbf{r}}_{P1}^{A}\times\underline{\mathbf{S}} \qquad (12) \\
&= \underline{\$}^{T}\,{}^{E}\delta\underline{\mathbf{D}}^{A}
\end{aligned}
$$

$$
\begin{aligned}
l\delta\theta &= {}^{E}\delta\underline{\mathbf{r}}_{P1}^{A}\cdot\frac{\partial\underline{\mathbf{S}}}{\partial\theta} = {}^{E}\delta\underline{\mathbf{r}}_{o}^{A}\cdot\frac{\partial\underline{\mathbf{S}}}{\partial\theta} + {}^{E}\delta\underline{\boldsymbol{\varphi}}^{A}\times{}^{E}\underline{\mathbf{r}}_{P1}^{A}\cdot\frac{\partial\underline{\mathbf{S}}}{\partial\theta} \\
&= {}^{E}\delta\underline{\mathbf{r}}_{o}^{A}\cdot\frac{\partial\underline{\mathbf{S}}}{\partial\theta} + {}^{E}\delta\underline{\boldsymbol{\varphi}}\cdot{}^{E}\underline{\mathbf{r}}_{P1}^{A}\times\frac{\partial\underline{\mathbf{S}}}{\partial\theta} \qquad (13) \\
&= \frac{\partial\underline{\$}'^{T}}{\partial\theta}\,{}^{E}\delta\underline{\mathbf{D}}^{A}
\end{aligned}
$$

and where,

$$
\frac{\partial\underline{\$}'}{\partial\theta} = \begin{bmatrix} \dfrac{\partial\underline{\mathbf{S}}}{\partial\theta} \\ {}^{E}\underline{\mathbf{r}}_{P1}^{A}\times\dfrac{\partial\underline{\mathbf{S}}}{\partial\theta} \end{bmatrix}. \qquad (14)
$$

All terms of Eq. (14) are known.

From Eqs. (8), (12), and (13),

$$
\begin{aligned}
\delta\,\underline{\mathbf{f}} &= k\delta\,l\underline{\$} + k(1-\frac{l_o}{l})\frac{\partial\underline{\$}}{\partial\theta}\,l\,\delta\,\theta \\
&= k\underline{\$}\underline{\$}^{T}\,{}^{E}\delta\underline{\mathbf{D}}^{A} + k(1-\frac{l_o}{l})\frac{\partial\underline{\$}}{\partial\theta}\frac{\partial\underline{\$}'^{T}}{\partial\theta}\,{}^{E}\delta\underline{\mathbf{D}}^{A} \qquad (15) \\
&= \left[K_F\right]{}^{E}\delta\underline{\mathbf{D}}^{A}
\end{aligned}
$$

where,

$$
\left[K_F\right] = k\underline{\$}\underline{\$}^{T} + k(1-\frac{l_o}{l})\frac{\partial\underline{\$}}{\partial\theta}\frac{\partial\underline{\$}'^{T}}{\partial\theta}. \qquad (16)
$$

$\left[K_F\right]$ is the stiffness matrix of a planar compliant coupling and maps a small twist of body A into the corresponding variation of the wrench. The first term of Eq. (16) is always symmetric and the second term is not. When the spring deviates from its equilibrium position due to an external wrench, the second term of Eq. (16) doesn't vanish and it makes the stiffness matrix asymmetric.

3.3 Linear planar springs in parallel arrangement

Figure 3.2c.12 depicts a body A supported by two compliant couplings in parallel and in equilibrium with an external wrench $\underline{\mathbf{w}}_{ext}$.

From the static equilibrium condition,

$$\underline{\mathbf{w}}_{ext} = \underline{\mathbf{f}}_1 + \underline{\mathbf{f}}_2 \quad (17)$$

where $\underline{\mathbf{f}}_1$ and $\underline{\mathbf{f}}_2$ are the forces from the springs.

By taking a derivative of Eq. (17) and using Eq. (16), the stiffness matrix of the two springs in parallel $\left[K_F\right]_R$ can be written by

$$\begin{aligned}\delta \underline{\mathbf{w}}_{ext} &= \delta \underline{\mathbf{f}}_1 + \delta \underline{\mathbf{f}}_2 \\ &= \left[K_F\right]_1 {}^E\delta \underline{\mathbf{D}}^A + \left[K_F\right]_2 {}^E\delta \underline{\mathbf{D}}^A \\ &= \left[K_F\right]_R {}^E\delta \underline{\mathbf{D}}^A\end{aligned}$$

$$\left[K_F\right]_R = \left[K_F\right]_1 + \left[K_F\right]_2 . \quad (18)$$

In the same way, the stiffness matrix of an arbitrary number of springs in parallel is obtained by the sum of stiffness matrix of each spring. This formula is analogous to that of springs in a line space shown in Eq. (3). Since $\left[K_F\right]_R$ is the sum of asymmetric matrices with an external wrench, it is also asymmetric.

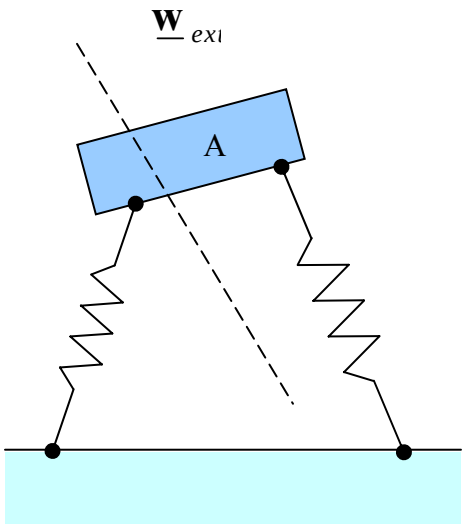

Figure 3.2c.12. Planar springs in parallel arrangement

3.2c.6 Linear Planar Springs In Serial Arrangement

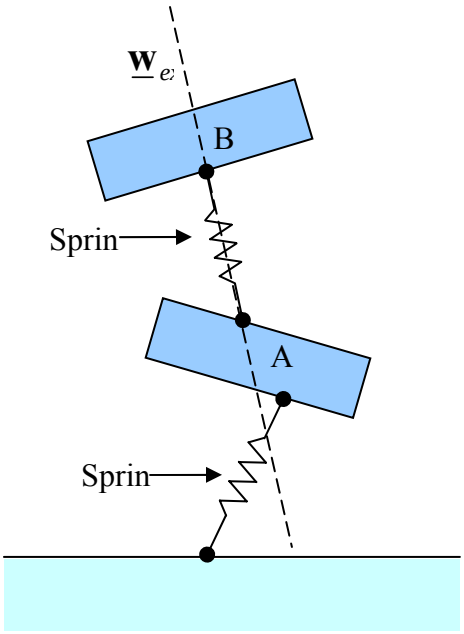

Figure 3.2c.13. Planar springs in parallel arrangement

Figure 3.2c.13 depicts two rigid bodies. Body B is connected to body A by a compliant coupling and body A is connected to the ground in the same way and they are in equilibrium. It is desired to obtain the stiffness matrix $[K]_R$ mapping a small twist of body B in terms of the ground ${}^E\delta\underline{\mathbf{D}}^B$ into the corresponding wrench variation $\delta\underline{\mathbf{w}}_{ext}$ as of Eq. (19).

$$\delta\underline{\mathbf{w}}_{ext} = [K]_R \, {}^E\delta\underline{\mathbf{D}}^B \quad . \quad (19)$$

From screw theory and static equilibrium condition,

$${}^E\delta\underline{\mathbf{D}}^B = {}^E\delta\underline{\mathbf{D}}^A + {}^A\delta\underline{\mathbf{D}}^B \qquad (20)$$

$$\underline{\mathbf{w}}_{ext} = \underline{\mathbf{f}}_2 = \underline{\mathbf{f}}_1 \quad (21)$$

where ${}^E\delta\underline{\mathbf{D}}^A$ and ${}^A\delta\underline{\mathbf{D}}^B$ are a small twist of body A in terms of the ground and that of body B in terms of body A, respectively. $\underline{\mathbf{f}}_1$ and $\underline{\mathbf{f}}_2$ are the forces from spring 1 and spring 2, respectively.

By taking a derivative of Eq. (21), a small variation of the wrench can be written by

$$\delta\underline{\mathbf{w}}_{ext} = \delta\underline{\mathbf{f}}_2 = \delta\underline{\mathbf{f}}_1 . \qquad (22)$$

It looks reasonable to infer that $\delta \underline{\mathbf{f}}_2$ is the stiffness matrix of spring 2 $\left[K_F\right]_2$ times the relative twist of body B with respect to body A ${}^A\delta \underline{\mathbf{D}}^B$ ignoring a small twist of body A and that $\delta \underline{\mathbf{f}}_2$ can be written by

$$\delta \underline{\mathbf{f}}_2 = \left[K_F\right]_2 {}^A\delta \underline{\mathbf{D}}^B . \quad (23)$$

Then from Eqs. (19), (22), and (23), Eq. (22) can be rewritten by

$$\begin{aligned} \delta \underline{\mathbf{w}}_{ext} &= \left[K\right]_R {}^E\delta \underline{\mathbf{D}}^B \\ &= \left[K_F\right]_2 {}^A\delta \underline{\mathbf{D}}^B . \quad (24) \\ &= \left[K_F\right]_1 {}^E\delta \underline{\mathbf{D}}^A \end{aligned}$$

Finally the stiffness matrix $\left[K\right]_R$ can be express as Eq. (25) by combining Eqs. (20) and (24). It is stated in Griffis [1991].

$$\left[K\right]_R = \left[K_F\right]_1 \left(\left[K_F\right]_1 + \left[K_F\right]_2\right)^{-1} \left[K_F\right]_2 \quad or \quad \left[K\right]_R^{-1} = \left[K_F\right]_1^{-1} + \left[K_F\right]_2^{-1} \qquad (25)$$

However the numerical example shown in the following section indicates that Eq. (25) is not correct. Since body B is supported by spring 2 and spring 2 is attached to body A which is not stationary, the derivative of the force from spring 2 $\delta \underline{\mathbf{f}}_2$ is affected by a small twist of body A as well as a relative twist of body B in terms of body A. To obtain a stiffness matrix of springs in a serial arrangement, a derivative of spring force joining two moving bodies is obtained in the next section.

3.2c.7 Derivative of Spring Force Joining Two Moving Bodies

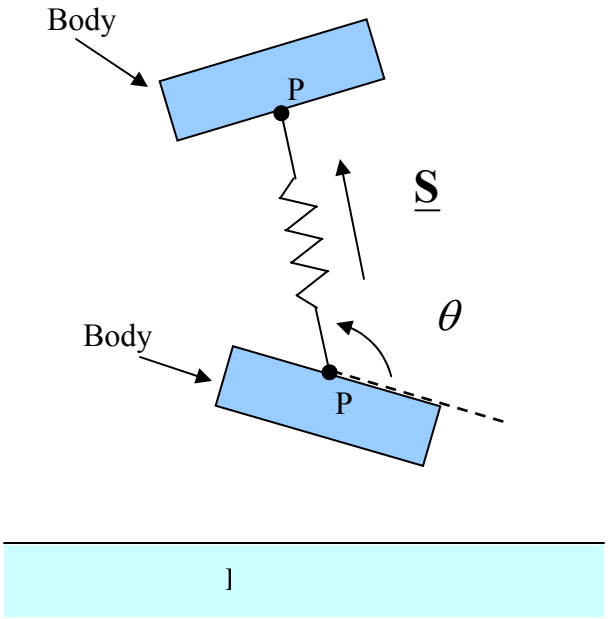

Figure 3.2c.14. Simple spring joining two moving bodies

Figure 3.2c.14 depicts two rigid bodies connected to each other by a compliant coupling with a spring constant k, a free length l_o, and a current length l. Body A can move in a planar space and the compliant coupling exerts a force $\underline{\mathbf{f}}$ to body B which is in equilibrium. The spring force may be written by

$$\underline{\mathbf{f}} = k(l - l_o)\underline{\$} \quad (26)$$

where

$$\underline{\$} = \begin{bmatrix} \underline{\mathbf{S}} \\ {}^{E}\underline{\mathbf{r}}^{A}_{P1} \times \underline{\mathbf{S}} \end{bmatrix} = \begin{bmatrix} \underline{\mathbf{S}} \\ {}^{E}\underline{\mathbf{r}}^{B}_{P2} \times \underline{\mathbf{S}} \end{bmatrix} \quad (27)$$

and where, $\underline{\mathbf{S}}$ is a unit vector along the compliant coupling and ${}^{E}\underline{\mathbf{r}}^{A}_{P1}$ and ${}^{E}\underline{\mathbf{r}}^{B}_{P2}$ are the position vector of the point P1 in body A and that of point P2 in body B, respectively, measured with respect to the reference system embedded in ground (body E). A small twist of body B with respect to an inertial frame E, ${}^{E}\delta\underline{\mathbf{D}}^{B}$, is applied and it is desired to find the corresponding change of the spring force. The twist ${}^{E}\delta\underline{\mathbf{D}}^{B}$ may be expressed as Eq. (20) and each term may be written by

$$ {}^{E}\delta\underline{\mathbf{D}}^{B} = \begin{bmatrix} {}^{E}\delta\underline{\mathbf{r}}_{o}^{B} \\ {}^{E}\delta\underline{\boldsymbol{\varphi}}^{B} \end{bmatrix} \qquad (28) $$

$$ {}^{E}\delta\underline{\mathbf{D}}^{A} = \begin{bmatrix} {}^{E}\delta\underline{\mathbf{r}}_{o}^{A} \\ {}^{E}\delta\underline{\boldsymbol{\varphi}}^{A} \end{bmatrix} \qquad (29) $$

$$ {}^{A}\delta\underline{\mathbf{D}}^{B} = \begin{bmatrix} {}^{A}\delta\underline{\mathbf{r}}_{o}^{B} \\ {}^{A}\delta\underline{\boldsymbol{\varphi}}^{B} \end{bmatrix} \qquad (30) $$

where the notation from Kane and Levinson is employed as stated in the beginning of this chapter. For example, ${}^{E}\delta\underline{\mathbf{r}}_{o}^{B}$ is the differential of point O, which is in body B and coincident with the origin of the inertial frame, measured with respect to the inertial frame and ${}^{E}\delta\underline{\boldsymbol{\varphi}}^{A}$ is the differential of angle of body A with respect to the inertial frame.

The derivative of the spring force as in Eq. (26) can be written by

$$ {}^{E}\delta\underline{\mathbf{f}} = k\,\delta l\,\underline{\$} + k\,(l - l_o)\,{}^{E}\delta\underline{\$}. \quad (31) $$

From the twist equation, the variation of position of point P2 in body B with respect to body A can be expressed as

$$ {}^{A}\delta\underline{\mathbf{r}}_{P2}^{B} = {}^{A}\delta\underline{\mathbf{r}}_{o}^{B} + {}^{A}\delta\underline{\boldsymbol{\varphi}}^{B} \times {}^{A}\underline{\mathbf{r}}_{P2}^{B} \quad (32) $$

where ${}^{A}\underline{\mathbf{r}}_{P2}^{B}$ is the position of P2, which is embedded in body B, measured with respect to a coordinate system embedded in body A which at this instant is coincident and aligned with the reference system attached to ground. It can also be decomposed into two perpendicular vectors along $\underline{\mathbf{S}}$ and $\frac{{}^{A}\partial\underline{\mathbf{S}}}{\partial\theta}$ which is a known unit vector perpendicular to $\underline{\mathbf{S}}$. These two vectors correspond to the change of the spring length δl and the directional change of the spring $l\delta\theta$ in terms of body A in a way that is analogous to that shown in Figure 3.2c.11. Thus the variation of position of point P2 in body B in terms of body A can be written as

$$ \begin{aligned} {}^{A}\delta\underline{\mathbf{r}}_{P2}^{B} &= \left({}^{A}\delta\underline{\mathbf{r}}_{P2}^{B} \cdot \underline{\mathbf{S}} \right)\underline{\mathbf{S}} + \left({}^{A}\delta\underline{\mathbf{r}}_{P2}^{B} \cdot \frac{{}^{A}\partial\underline{\mathbf{S}}}{\partial\theta} \right)\frac{{}^{A}\partial\underline{\mathbf{S}}}{\partial\theta} \\ &= \delta l\,\underline{\mathbf{S}} + l\delta\theta\frac{{}^{A}\partial\underline{\mathbf{S}}}{\partial\theta} \end{aligned} \qquad (33) $$

where

$$ {}^{A}\frac{\partial \underline{\$}}{\partial \theta} = \begin{bmatrix} {}^{A}\frac{\partial \underline{\mathbf{S}}}{\partial \theta} \\ {}^{A}\underline{\mathbf{r}}_{P1}^{A} \times {}^{A}\frac{\partial \underline{\mathbf{S}}}{\partial \theta} \end{bmatrix}. \quad (34) $$

From Eqs. (32) and (33), δl and $l\delta\theta$ can be obtained as Eqs. (35) and (36).

$$ \begin{aligned} \delta l &= {}^{A}\delta \underline{\mathbf{r}}_{P2}^{B} \cdot \underline{\mathbf{S}} = {}^{A}\delta \underline{\mathbf{r}}_{o}^{B} \cdot \underline{\mathbf{S}} + {}^{A}\delta \underline{\boldsymbol{\varphi}}^{B} \times {}^{A}\underline{\mathbf{r}}_{P2}^{B} \cdot \underline{\mathbf{S}} \\ &= {}^{A}\delta \underline{\mathbf{r}}_{o}^{B} \cdot \underline{\mathbf{S}} + {}^{A}\delta \underline{\boldsymbol{\varphi}}^{B} \cdot {}^{A}\underline{\mathbf{r}}_{P2}^{B} \times \underline{\mathbf{S}} \qquad (35) \\ &= \underline{\$}^{T}\, {}^{A}\delta \underline{\mathbf{D}}^{B} \end{aligned} $$

$$ \begin{aligned} l\delta\theta &= {}^{A}\delta \underline{\mathbf{r}}_{P2}^{B} \cdot \frac{{}^{A}\partial \underline{\mathbf{S}}}{\partial \theta} = {}^{A}\delta \underline{\mathbf{r}}_{o}^{B} \cdot \frac{{}^{A}\partial \underline{\mathbf{S}}}{\partial \theta} + {}^{A}\delta \underline{\boldsymbol{\varphi}}^{B} \times {}^{A}\underline{\mathbf{r}}_{P2}^{B} \cdot \frac{{}^{A}\partial \underline{\mathbf{S}}}{\partial \theta} \\ &= {}^{A}\delta \underline{\mathbf{r}}_{o}^{B} \cdot \frac{{}^{A}\partial \underline{\mathbf{S}}}{\partial \theta} + {}^{A}\delta \underline{\boldsymbol{\varphi}}^{B} \cdot {}^{A}\underline{\mathbf{r}}_{P2}^{B} \times \frac{{}^{A}\partial \underline{\mathbf{S}}}{\partial \theta} \qquad (36) \\ &= \frac{{}^{A}\partial \underline{\$}'^{T}}{\partial \theta}\, {}^{A}\delta \underline{\mathbf{D}}^{B} \end{aligned} $$

where

$$ {}^{A}\frac{\partial \underline{\$}'}{\partial \theta} = \begin{bmatrix} {}^{A}\frac{\partial \underline{\mathbf{S}}}{\partial \theta} \\ {}^{A}\underline{\mathbf{r}}_{P2}^{B} \times {}^{A}\frac{\partial \underline{\mathbf{S}}}{\partial \theta} \end{bmatrix}. \qquad (37) $$

It is important to note that screw ${}^{A}\frac{\partial \underline{\$}'}{\partial \theta}$ has the same direction as ${}^{A}\frac{\partial \underline{\$}}{\partial \theta}$ but has a different moment term.

Now among Eq. (31), only ${}^{E}\delta \underline{\$}$ is unknown. It is a derivative of the unit screw along the spring in terms of the inertial frame and may be written as

$$ {}^{E}\delta \underline{\$} = \begin{bmatrix} {}^{E}\delta \underline{\mathbf{S}} \\ {}^{E}\delta \underline{\mathbf{r}}_{P1}^{A} \times \underline{\mathbf{S}} + {}^{E}\underline{\mathbf{r}}_{P1}^{A} \times {}^{E}\delta \underline{\mathbf{S}} \end{bmatrix}. \qquad (38) $$

Using an intermediate frame attached to body A,

$$ {}^{E}\delta \underline{\mathbf{S}} = {}^{A}\delta \underline{\mathbf{S}} + {}^{E}\delta \underline{\boldsymbol{\varphi}}^{A} \times \underline{\mathbf{S}}. \qquad (39) $$

Then, ${}^{E}\delta \underline{\$}$ may be decomposed into three screws as follows

$$
\begin{aligned}
{}^{E}\delta\underline{\$} &= \begin{bmatrix} {}^{E}\delta\underline{\mathbf{S}} \\ {}^{E}\delta\underline{\mathbf{r}}_{P1}^{A}\times\underline{\mathbf{S}} + {}^{E}\underline{\mathbf{r}}_{P1}^{A}\times{}^{E}\delta\underline{\mathbf{S}} \end{bmatrix} \\
&= \begin{bmatrix} {}^{A}\delta\underline{\mathbf{S}} + {}^{E}\delta\underline{\boldsymbol{\varphi}}^{A}\times\underline{\mathbf{S}} \\ {}^{E}\delta\underline{\mathbf{r}}_{P1}^{A}\times\underline{\mathbf{S}} + {}^{E}\underline{\mathbf{r}}_{P1}^{A}\times\left({}^{A}\delta\underline{\mathbf{S}} + {}^{E}\delta\underline{\boldsymbol{\varphi}}^{A}\times\underline{\mathbf{S}}\right) \end{bmatrix} \\
&= \begin{bmatrix} {}^{A}\delta\underline{\mathbf{S}} \\ {}^{E}\underline{\mathbf{r}}_{P1}^{A}\times{}^{A}\delta\underline{\mathbf{S}} \end{bmatrix} + \begin{bmatrix} {}^{E}\delta\underline{\boldsymbol{\varphi}}^{A}\times\underline{\mathbf{S}} \\ {}^{E}\underline{\mathbf{r}}_{P1}^{A}\times\left({}^{E}\delta\underline{\boldsymbol{\varphi}}^{A}\times\underline{\mathbf{S}}\right) \end{bmatrix} + \begin{bmatrix} \underline{\mathbf{0}} \\ {}^{E}\delta\underline{\mathbf{r}}_{P1}^{A}\times\underline{\mathbf{S}} \end{bmatrix}
\end{aligned} \quad . \qquad (40)
$$

Since $\underline{\mathbf{S}}$ is a function of θ alone from the vantage of body A and $l\delta\theta$ is already described in Eq. (36), the first screw in Eq. (40) can be written as Eq. (41).

$$
\begin{bmatrix} {}^{A}\delta\underline{\mathbf{S}} \\ {}^{E}\underline{\mathbf{r}}_{P1}^{A}\times{}^{A}\delta\underline{\mathbf{S}} \end{bmatrix} = \begin{bmatrix} \dfrac{{}^{A}\partial\underline{\mathbf{S}}}{\partial\theta}\delta\theta \\ {}^{E}\underline{\mathbf{r}}_{P1}^{A}\times\dfrac{{}^{A}\partial\underline{\mathbf{S}}}{\partial\theta}\delta\theta \end{bmatrix} = \frac{{}^{A}\partial\underline{\$}}{\partial\theta}\frac{1}{l}l\delta\theta = \frac{1}{l}\frac{{}^{A}\partial\underline{\$}}{\partial\theta}\frac{{}^{A}\partial\underline{\$}'^{T}}{\partial\theta}\,{}^{A}\delta\underline{\mathbf{D}}^{B}. \qquad (41)
$$

As to the second screw in Eq. (40), ${}^{E}\delta\underline{\boldsymbol{\varphi}}^{A}\times\underline{\mathbf{S}}$ has the same direction with $\dfrac{{}^{A}\partial\underline{\mathbf{S}}}{\partial\theta}$ and the magnitude of ${}_{E}\delta\phi_{A}$ and thus may be written as

$$
{}^{E}\delta\underline{\boldsymbol{\varphi}}^{A}\times\underline{\mathbf{S}} = {}_{E}\delta\phi_{A}\frac{{}^{A}\partial\underline{\mathbf{S}}}{\partial\theta}. \qquad (42)
$$

Then the second screw in Eq. (40) can be expressed as

$$
\begin{aligned}
\begin{bmatrix} {}^{E}\delta\underline{\boldsymbol{\varphi}}^{A}\times\underline{\mathbf{S}} \\ {}^{E}\underline{\mathbf{r}}_{P1}^{A}\times\left({}^{E}\delta\underline{\boldsymbol{\varphi}}^{A}\times\underline{\mathbf{S}}\right) \end{bmatrix} &= \begin{bmatrix} \dfrac{{}^{A}\partial\underline{\mathbf{S}}}{\partial\theta}\,{}_{E}\delta\phi_{A} \\ {}^{E}\underline{\mathbf{r}}_{P1}^{A}\times\dfrac{{}^{A}\partial\underline{\mathbf{S}}}{\partial\theta}\,{}_{E}\delta\phi_{A} \end{bmatrix} \quad . \qquad (43) \\
&= \frac{{}^{A}\partial\underline{\$}}{\partial\theta}\,{}_{E}\delta\phi_{A} = \frac{{}^{A}\partial\underline{\$}}{\partial\theta}\begin{bmatrix} 0 & 0 & 1 \end{bmatrix}{}^{E}\delta\underline{\mathbf{D}}^{A}
\end{aligned}
$$

As to the third screw in Eq. (40), ${}^{E}\delta\underline{\mathbf{r}}_{P1}^{A}$ can be decomposed into two perpendicular vectors along $\underline{\mathbf{S}}$ and $\dfrac{{}^{A}\partial\underline{\mathbf{S}}}{\partial\theta}$, respectively. Further

$$
\begin{aligned}
{}^{E}\delta\underline{\mathbf{r}}_{P1}^{A} &= {}^{E}\delta\underline{\mathbf{r}}_{o}^{A} + {}^{E}\delta\underline{\boldsymbol{\varphi}}^{A} \times {}^{E}\underline{\mathbf{r}}_{P1}^{A} \\
&= \left({}^{E}\delta\underline{\mathbf{r}}_{P1}^{A} \cdot \underline{\mathbf{S}} \right)\underline{\mathbf{S}} + \left({}^{E}\delta\underline{\mathbf{r}}_{P1}^{A} \cdot \frac{{}^{A}\partial\underline{\mathbf{S}}}{\partial\theta} \right)\frac{{}^{A}\partial\underline{\mathbf{S}}}{\partial\theta} \\
&= \left({}^{E}\delta\underline{\mathbf{r}}_{o}^{A} \cdot \underline{\mathbf{S}} + {}^{E}\delta\underline{\boldsymbol{\varphi}}^{A} \times \underline{\mathbf{r}}_{P1}^{A} \cdot \underline{\mathbf{S}} \right)\underline{\mathbf{S}} + \left({}^{E}\delta\underline{\mathbf{r}}_{o}^{A} \cdot \frac{{}^{A}\partial\underline{\mathbf{S}}}{\partial\theta} + {}^{E}\delta\underline{\boldsymbol{\varphi}}^{A} \times \underline{\mathbf{r}}_{P1}^{A} \cdot \frac{{}^{A}\partial\underline{\mathbf{S}}}{\partial\theta} \right)\frac{{}^{A}\partial\underline{\mathbf{S}}}{\partial\theta} \\
&= \left({}^{E}\delta\underline{\mathbf{r}}_{o}^{A} \cdot \underline{\mathbf{S}} + {}^{E}\delta\underline{\boldsymbol{\varphi}}^{A} \cdot \underline{\mathbf{r}}_{P1}^{A} \times \underline{\mathbf{S}} \right)\underline{\mathbf{S}} + \left({}^{E}\delta\underline{\mathbf{r}}_{o}^{A} \cdot \frac{{}^{A}\partial\underline{\mathbf{S}}}{\partial\theta} + {}^{E}\delta\underline{\boldsymbol{\varphi}}^{A} \cdot \underline{\mathbf{r}}_{P1}^{A} \times \frac{{}^{A}\partial\underline{\mathbf{S}}}{\partial\theta} \right)\frac{{}^{A}\partial\underline{\mathbf{S}}}{\partial\theta} \\
&= \left(\underline{\$}^{T}\, {}^{E}\delta\underline{\mathbf{D}}^{A} \right)\underline{\mathbf{S}} + \left(\frac{{}^{A}\partial\underline{\$}^{T}}{\partial\theta}\, {}^{E}\delta\underline{\mathbf{D}}^{A} \right)\frac{{}^{A}\partial\underline{\mathbf{S}}}{\partial\theta}
\end{aligned}
\tag{44}
$$

Then the third screw in Eq. (40) can be written as

$$
\begin{aligned}
\begin{bmatrix} \underline{\mathbf{0}} \\ {}^{E}\delta\underline{\mathbf{r}}_{P1}^{A} \times \underline{\mathbf{S}} \end{bmatrix} &= \begin{bmatrix} \underline{\mathbf{0}} \\ \left\{ \left(\underline{\$}^{T}\, {}^{E}\delta\underline{\mathbf{D}}^{A} \right)\underline{\mathbf{S}} + \left(\frac{{}^{A}\partial\underline{\$}^{T}}{\partial\theta}\, {}^{E}\delta\underline{\mathbf{D}}^{A} \right)\frac{{}^{A}\partial\underline{\mathbf{S}}}{\partial\theta} \right\} \times \underline{\mathbf{S}} \end{bmatrix} \\
&= \begin{bmatrix} \underline{\mathbf{0}} \\ \left(\frac{{}^{A}\partial\underline{\$}^{T}}{\partial\theta}\, {}^{E}\delta\underline{\mathbf{D}}^{A} \right)\frac{{}^{A}\partial\underline{\mathbf{S}}}{\partial\theta} \times \underline{\mathbf{S}} \end{bmatrix} \\
&= \begin{bmatrix} \underline{\mathbf{0}} \\ -\frac{{}^{A}\partial\underline{\$}^{T}}{\partial\theta}\, {}^{E}\delta\underline{\mathbf{D}}^{A} \end{bmatrix} \\
&= \begin{bmatrix} 0 \\ 0 \\ -1 \end{bmatrix} \frac{{}^{A}\partial\underline{\$}^{T}}{\partial\theta}\, {}^{E}\delta\underline{\mathbf{D}}^{A}
\end{aligned}
\tag{45}
$$

because $\dfrac{{}^{A}\partial\underline{\mathbf{S}}}{\partial\theta} \times \underline{\mathbf{S}} = -1\left(\underline{\mathbf{k}}\right)$.

Among all unknowns of Eq. (31), δl was obtained in Eq. (35) and all the terms of ${}^{E}\delta\underline{\$}$ were obtained through Eqs. (41), (43), and (45).

Hence the derivative of the spring force can be rewritten by

$$
\begin{aligned}
{}^{E}\delta\underline{\mathbf{f}} &= k\delta l\underline{\$} + k(l-l_o)\,{}^{E}\delta\underline{\$} \\
&= k\underline{\$}\underline{\$}^{T}\,{}^{A}\delta\underline{\mathbf{D}}^{B} + k(l-l_o)\left(\frac{1}{l}\frac{{}^{A}\partial\underline{\$}}{\partial\theta}\frac{{}^{A}\partial\underline{\$}'^{T}}{\partial\theta}\,{}^{A}\delta\underline{\mathbf{D}}^{B} + \frac{{}^{A}\partial\underline{\$}}{\partial\theta}\begin{bmatrix}0 & 0 & 1\end{bmatrix}{}^{E}\delta\underline{\mathbf{D}}^{A} + \begin{bmatrix}0\\0\\-1\end{bmatrix}\frac{{}^{A}\partial\underline{\$}^{T}}{\partial\theta}\,{}^{E}\delta\underline{\mathbf{D}}^{A}\right) \\
&= \left(k\underline{\$}\underline{\$}^{T} + k(1-\frac{l_o}{l})\frac{{}^{A}\partial\underline{\$}}{\partial\theta}\frac{{}^{A}\partial\underline{\$}'^{T}}{\partial\theta}\right){}^{A}\delta\underline{\mathbf{D}}^{B} + k(l-l_o)\left(\frac{{}^{A}\partial\underline{\$}}{\partial\theta}\begin{bmatrix}0 & 0 & 1\end{bmatrix} + \begin{bmatrix}0\\0\\-1\end{bmatrix}\frac{{}^{A}\partial\underline{\$}^{T}}{\partial\theta}\right){}^{E}\delta\underline{\mathbf{D}}^{A} \\
&= \left[K_F\right]{}^{A}\delta\underline{\mathbf{D}}^{B} + \left[K_M\right]{}^{E}\delta\underline{\mathbf{D}}^{A}
\end{aligned}
\tag{46}
$$

where

$$
\left[K_F\right] = k\underline{\$}\underline{\$}^{T} + k(1-\frac{l_o}{l})\frac{{}^{A}\partial\underline{\$}}{\partial\theta}\frac{{}^{A}\partial\underline{\$}'^{T}}{\partial\theta} \tag{47}
$$

$$
\left[K_M\right] = k(l-l_o)\left(\frac{{}^{A}\partial\underline{\$}}{\partial\theta}\begin{bmatrix}0 & 0 & 1\end{bmatrix} + \begin{bmatrix}0\\0\\-1\end{bmatrix}\frac{{}^{A}\partial\underline{\$}^{T}}{\partial\theta}\right). \tag{48}
$$

As shown in Eq. (46), the derivative of the spring force joining two rigid bodies depends not only on a relative twist between two bodies but also on the twist of the intermediate body, in this case body A, in terms of the inertial frame. $\left[K_F\right]$ which maps a small twist of body B in terms of body A into the corresponding change of wrench upon body B is identical to a stiffness matrix of the spring assuming the body A is stationary. $\left[K_M\right]$ is newly introduced from this research and results from the motion of the base frame, in this case body A. $\left[K_M\right]$ takes a skew symmetric form in general.

3.2c.8 Stiffness Matrix of Compliant Couplings Having Serially Arranged Springs

The stiffness matrix of the compliant coupling shown in Figure 3.2c.13 is derived. The stiffness matrix maps a small twist of body B in terms of the inertial frame into the corresponding change of the wrench on body B. The same procedure for deriving Eq. (25) is employed except for the description of $\delta\underline{\mathbf{f}}_2$ because $\underline{\mathbf{f}}_2$ is spring force connecting two moving bodies. Eq. (24) can be rewritten by

$$\begin{aligned}\delta \underline{\mathbf{w}}_{ext} &= [K]_R \; {}^E\delta \underline{\mathbf{D}}^B \\ &= [K_F]_1 \; {}^E\delta \underline{\mathbf{D}}^A \\ &= [K_F]_2 \; {}^A\delta \underline{\mathbf{D}}^B + [K_M]_2 \; {}^E\delta \underline{\mathbf{D}}^A\end{aligned} \tag{49}$$

where $[K]_R$ is the resultant stiffness matrix of the coupling and $[K_F]_1$ is the stiffness matrix of spring 1. $[K_F]_2$ and $[K_M]_2$ are the stiffness mapping of spring 2 as defined in Eqs. (47) and (48).

By eliminating ${}^A\delta \underline{\mathbf{D}}^B$ in Eq. (49) using Eq. (20) and with a proper arrangement of the terms, the stiffness matrix can be obtained as Eq. (50)

$$\begin{aligned}[K_F]_1 \; {}^E\delta \underline{\mathbf{D}}^A &= [K_F]_2 \; {}^A\delta \underline{\mathbf{D}}^B + [K_M]_2 \; {}^E\delta \underline{\mathbf{D}}^A \\ &= [K_F]_2 \left({}^E\delta \underline{\mathbf{D}}^B - {}^E\delta \underline{\mathbf{D}}^A \right) + [K_M]_2 \; {}^E\delta \underline{\mathbf{D}}^A\end{aligned}$$

$${}^E\delta \underline{\mathbf{D}}^A = \left([K_F]_1 + [K_F]_2 - [K_M]_2 \right)^{-1} [K_F]_2 \; {}^E\delta \underline{\mathbf{D}}^B$$

$$\begin{aligned}[K]_R \; {}^E\delta \underline{\mathbf{D}}^B &= [K_F]_1 \; {}^E\delta \underline{\mathbf{D}}^A \\ &= [K_F]_1 \left([K_F]_1 + [K_F]_2 - [K_M]_2 \right)^{-1} [K_F]_2 \; {}^E\delta \underline{\mathbf{D}}^B\end{aligned}$$

$$[K]_R = [K_F]_1 \left([K_F]_1 + [K_F]_2 - [K_M]_2 \right)^{-1} [K_F]_2 \tag{50}$$

$$[K]_R^{-1} = [K_F]_1^{-1} + [K_F]_2^{-1} - [K_F]_2^{-1} [K_M]_2 [K_F]_1^{-1} \tag{51}$$

To compare the result with that of Griffis [1991], an inverse of $[K]_R$ is obtained as Eq. (51). The first two terms of Eq. (51) are identical to those of Griffis [1991] and the third term is newly introduced from this research.

3.2c.9 Numerical Example

The mechanism in Figure 3.2c.15 has two moving platforms. Body A is connected to ground by three compliant couplings and body B is connected to body A in the same way. Each compliant coupling has a revolute joint at each end and a prismatic joint with a spring in the middle part. It is assumed that an external wrench $\underline{\mathbf{w}}_{ext}$ is applied to body B and that both body B and body A are in static equilibrium. The positions and orientations of bodies A and B and the spring constants and free lengths of all constituent springs are given. The stiffness matrix $[K]$ which maps a small twist of body B with respect to the ground ${}^E\delta \underline{\mathbf{D}}^B$ into a small wrench variation $\delta \underline{\mathbf{w}}_{ext}$ is written below in a similar way shown in the previous section.

$$\begin{aligned}\delta \underline{\mathbf{w}}_{ext} &= [K]\,{}^{E}\delta \underline{\mathbf{D}}^{B} \\ &= \delta \underline{\mathbf{f}}_4 + \delta \underline{\mathbf{f}}_5 + \delta \underline{\mathbf{f}}_6 \\ &= \delta \underline{\mathbf{f}}_1 + \delta \underline{\mathbf{f}}_2 + \delta \underline{\mathbf{f}}_3\end{aligned}$$

$$\begin{aligned}\delta \underline{\mathbf{f}}_4 + \delta \underline{\mathbf{f}}_5 + \delta \underline{\mathbf{f}}_6 &= [K_F]_4\,{}^{E}\delta \underline{\mathbf{D}}^{A} + [K_F]_5\,{}^{E}\delta \underline{\mathbf{D}}^{A} + [K_F]_6\,{}^{E}\delta \underline{\mathbf{D}}^{A} \\ &= [K_F]_{R,L}\,{}^{E}\delta \underline{\mathbf{D}}^{A}\end{aligned}$$

$$\begin{aligned}\delta \underline{\mathbf{f}}_1 + \delta \underline{\mathbf{f}}_2 + \delta \underline{\mathbf{f}}_3 &= [K_F]_1\,{}^{A}\delta \underline{\mathbf{D}}^{B} + [K_F]_2\,{}^{A}\delta \underline{\mathbf{D}}^{B} + [K_F]_3\,{}^{A}\delta \underline{\mathbf{D}}^{B} \\ &\quad + [K_M]_1\,{}^{E}\delta \underline{\mathbf{D}}^{A} + [K_M]_2\,{}^{E}\delta \underline{\mathbf{D}}^{A} + [K_M]_3\,{}^{E}\delta \underline{\mathbf{D}}^{A} \\ &= [K_F]_{R,U}\,{}^{A}\delta \underline{\mathbf{D}}^{B} + [K_M]_{R,U}\,{}^{E}\delta \underline{\mathbf{D}}^{A}\end{aligned}$$

$$\begin{aligned}\delta \underline{\mathbf{w}}_{ext} &= [K]\,{}^{E}\delta \underline{\mathbf{D}}^{B} \\ &= [K_F]_{R,L}\,{}^{E}\delta \underline{\mathbf{D}}^{A} \\ &= [K_F]_{R,U}\,{}^{A}\delta \underline{\mathbf{D}}^{B} + [K_M]_{R,U}\,{}^{E}\delta \underline{\mathbf{D}}^{A}\end{aligned}$$

$$[K] = [K_F]_{R,L}\left([K_F]_{R,L} + [K_F]_{R,U} - [K_M]_{R,U}\right)^{-1}[K_F]_{R,U} \qquad (52)$$

where

$$[K_F]_{R,L} = \sum_{i=4}^{6}[K_F]_i$$

$$[K_F]_{R,U} = \sum_{i=1}^{3}[K_F]_i$$

$$[K_M]_{R,U} = \sum_{i=1}^{3}[K_M]_i$$

$$[K_F]_i = k_i \underline{\$}_i \underline{\$}_i^{T} + k_i\left(1 - \frac{l_{oi}}{l_i}\right)\frac{{}^{A}\partial \underline{\$}_i}{\partial \theta_i}\frac{{}^{A}\partial \underline{\$}_i'^{T}}{\partial \theta_i}, \quad i = 1\ldots 6$$

$$[K_M]_i = k_i(l_i - l_{oi})\left(\frac{{}^{A}\partial \underline{\$}_i}{\partial \theta_i}[0 \quad 0 \quad 1] + \begin{bmatrix}0\\0\\-1\end{bmatrix}\frac{{}^{A}\partial \underline{\$}_i^{T}}{\partial \theta_i}\right), \quad i = 1\ldots 3.$$

Now the geometry information, spring properties, and the external wrench are given below.

$${}^{E}\underline{\mathbf{r}}_{E1}^{E} = \begin{bmatrix}0.0\\0.0\end{bmatrix}, \quad {}^{E}\underline{\mathbf{r}}_{E2}^{E} = \begin{bmatrix}1.5\\1.2\end{bmatrix}, \quad {}^{E}\underline{\mathbf{r}}_{E3}^{E} = \begin{bmatrix}3.0\\0.5\end{bmatrix} \quad (cm)$$

$${}^{A}\underline{\mathbf{r}}_{a1}^{A} = \begin{bmatrix}0.0\\0.0\end{bmatrix}, \quad {}^{A}\underline{\mathbf{r}}_{a2}^{A} = \begin{bmatrix}1.0\\-1.7321\end{bmatrix}, \quad {}^{A}\underline{\mathbf{r}}_{a3}^{A} = \begin{bmatrix}2.0\\0.0\end{bmatrix}, \quad {}^{A}\underline{\mathbf{r}}_{a4}^{A} = \begin{bmatrix}1.0\\0.5\end{bmatrix} \quad (cm)$$

$$ {}^{B}\underline{\mathbf{r}}_{b1}^{B} = \begin{bmatrix} 0.0 \\ 0.0 \end{bmatrix}, \quad {}^{B}\underline{\mathbf{r}}_{b2}^{B} = \begin{bmatrix} 1.0 \\ -1.7321 \end{bmatrix}, \quad {}^{B}\underline{\mathbf{r}}_{b3}^{B} = \begin{bmatrix} 2.0 \\ 0.0 \end{bmatrix} \quad (cm) $$

$$ {}^{E}\underline{\mathbf{r}}_{Ao}^{A} = \begin{bmatrix} 0.9036 \\ 4.5962 \end{bmatrix}, \quad {}^{E}\underline{\mathbf{r}}_{Bo}^{B} = \begin{bmatrix} 0.0903 \\ 9.8612 \end{bmatrix} \quad (cm) $$

$$ \phi 1 = 0.4275, \quad \phi 2 = 0.4175 \quad (radian) $$

$$ \underline{\mathbf{w}}_{ext} = \begin{bmatrix} 0.01 & N \\ -0.02 & N \\ 0.03 & Ncm \end{bmatrix} $$

$$ k_1 = 0.2, \quad k_2 = 0.3, \quad k_3 = 0.4, \quad k_4 = 0.5, \quad k_5 = 0.6, \quad k_6 = 0.7 \left(N/cm \right) $$

$$ l_{o1}=5.0040,\ l_{o2}=2.2860,\ l_{o3}=4.9458,\ l_{o4}=5.5145,\ l_{o5}=3.1573,\ l_{o6}=5.2568 \quad (\mathrm{cm}) $$

Where ${}^{E}\underline{\mathbf{r}}_{Ei}^{E}$ is the position of the i-th fixed pivot point in terms of the inertial frame. ${}^{B}\underline{\mathbf{r}}_{bi}^{B}$ is the position of i-th vertex of body B in terms of a coordinates system B attached to body B and ${}^{A}\underline{\mathbf{r}}_{ai}^{A}$ is that of body A in terms of a coordinates system A attached to body A, respectively. ${}^{E}\underline{\mathbf{r}}_{Ao}^{A}$ and ${}^{E}\underline{\mathbf{r}}_{Bo}^{B}$ are the position of the origin of coordinates system A and B, measured in the fixed frame, respectively. Two stiffness matrices are obtained. $[K_1]$ is from Eq. (52) and $[K_2]$ from the same equation ignoring $\left[K_M\right]_{R,U}$ as that of Griffis [1991].

$$ [K_1] = \begin{bmatrix} 0.0108 & N/cm & -0.0172 & N/cm & -0.0797 & N \\ -0.0172 & N/cm & 0.3447 & N/cm & 0.8351 & N \\ -0.0997 & N & 0.8251 & N & 2.6567 & Ncm \end{bmatrix} $$

$$ [K_2] = \begin{bmatrix} 0.0111 & N/cm & -0.0157 & N/cm & -0.0874 & N \\ -0.0162 & N/cm & 0.3462 & N/cm & 0.8124 & N \\ -0.0969 & N & 0.8150 & N & 2.6129 & Ncm \end{bmatrix} $$

To evaluate the result, a small wrench $\delta \underline{\mathbf{w}}$ is applied to body B and the static equilibrium pose of the mechanism is obtained by a numerically iterative method. From the equilibrium pose of the mechanism, the twist of body B with respect to ground ${}^{E}\delta\underline{\mathbf{D}}^{B}$ is obtained as shown below.

$$ \delta \underline{\mathbf{w}} = 10^{-4} \times \begin{bmatrix} 0.5 & N \\ 0.2 & N \\ 0.4 & Ncm \end{bmatrix} $$

$$ {}^{E}\delta\underline{\mathbf{D}}^{B} = \begin{bmatrix} 0.0077 & cm \\ -0.0012 & cm \\ 0.0007 & rad \end{bmatrix} $$

Then the twist ${}^{E}\delta\underline{\mathbf{D}}^{B}$ is multiplied by both of the stiffness matrices to see if the given small wrench $\delta\underline{\mathbf{w}}$ results.

$$ \delta\underline{\mathbf{w}}_1 = [K_1]\,{}^{E}\delta\underline{\mathbf{D}}^{B} = 10^{-4} \times \begin{bmatrix} 0.4991 & N \\ 0.1988 & N \\ 0.4016 & Ncm \end{bmatrix} $$

$$ \delta\underline{\mathbf{w}}_2 = [K_2]\,{}^{E}\delta\underline{\mathbf{D}}^{B} = 10^{-4} \times \begin{bmatrix} 0.4515 & N \\ 0.1071 & N \\ 0.4491 & Ncm \end{bmatrix} $$

The numerical example indicates that $[K_1]$ produces the given wrench $\delta\underline{\mathbf{w}}$ with high accuracy and that $[K_2]$ involves some significant errors.

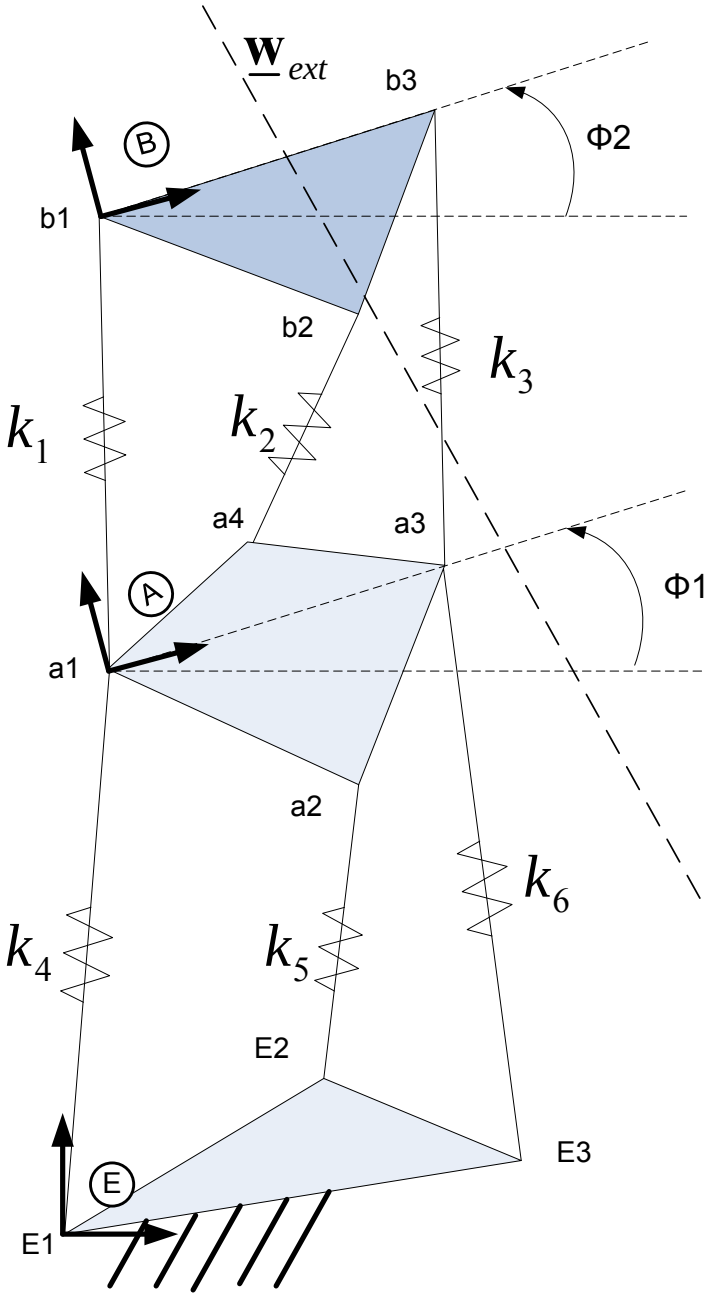

Figure 3.2c.15. Example compliant mechanism

3.2c.10 Stiffness Matrix Of Linear Planar Springs In Hybrid Arrangement

Figure 3.2c.16 depicts a compliant mechanism having a serial/parallel arrangement of compliant couplings. Each compliant coupling has a revolute joint at each end and a prismatic joint with a spring in the middle part. An external wrench is applied to body T and body T is separately connected to body B, body C, and body D by three compliant springs. Body B, body C, and body D are connected to ground by two compliant springs. It is assumed that all bodies are in static equilibrium. It is desired to find the stiffness matrix mapping a small twist of body T in terms of ground ${}^{E}\delta\underline{\mathbf{D}}^{T}$ to the corresponding wrench variation $\delta\,\underline{\mathbf{w}}_{ext}$. The stiffness constants and free lengths of all constituent springs and the geometry of the mechanism are assumed to be known.

The stiffness matrix of the mechanism can be derived by taking a derivative of the static equilibrium equations. The static equilibrium equations may be written as

$$\underline{\mathbf{w}}_{ext} = \underline{\mathbf{f}}_7 + \underline{\mathbf{f}}_8 + \underline{\mathbf{f}}_9 \qquad (53)$$

$$\underline{\mathbf{f}}_7 = \underline{\mathbf{f}}_1 + \underline{\mathbf{f}}_2 \qquad (54)$$

$$\underline{\mathbf{f}}_8 = \underline{\mathbf{f}}_3 + \underline{\mathbf{f}}_4 \qquad (55)$$

$$\underline{\mathbf{f}}_9 = \underline{\mathbf{f}}_5 + \underline{\mathbf{f}}_6 \qquad (56)$$

where $\underline{\mathbf{w}}_{ext}$ is the external wrench and $\underline{\mathbf{f}}_i$ is the force of i-th spring.

Derivatives of Eqs. (53)-(56) can be written as

$$\begin{aligned}\delta\,\underline{\mathbf{w}}_{ext} &= \delta\,\underline{\mathbf{f}}_7 + \delta\,\underline{\mathbf{f}}_8 + \delta\,\underline{\mathbf{f}}_9 \\ &= \left[K\right]_R\ {}^{E}\delta\underline{\mathbf{D}}^{T}\end{aligned} \qquad (57)$$

$$\delta\,\underline{\mathbf{f}}_7 = \delta\,\underline{\mathbf{f}}_1 + \delta\,\underline{\mathbf{f}}_2 \qquad (58)$$

$$\delta\,\underline{\mathbf{f}}_8 = \delta\,\underline{\mathbf{f}}_3 + \delta\,\underline{\mathbf{f}}_4 \qquad (59)$$

$$\delta\,\underline{\mathbf{f}}_9 = \delta\,\underline{\mathbf{f}}_5 + \delta\,\underline{\mathbf{f}}_6 \qquad (60)$$

where $\left[K\right]_R$ is the stiffness matrix and ${}^{E}\delta\underline{\mathbf{D}}^{T}$ is a small twist of body T in terms of the inertial frame attached to the ground.

Using Eqs. (15) and (46), Eq. (58) can be rewritten by

$$\begin{aligned}\delta\,\underline{\mathbf{f}}_7 &= \left[K_F\right]_7\ {}^{B}\delta\underline{\mathbf{D}}^{T} + \left[K_M\right]_7\ {}^{E}\delta\underline{\mathbf{D}}^{B} \\ &= \left[K_F\right]_1\ {}^{E}\delta\underline{\mathbf{D}}^{B} + \left[K_F\right]_2\ {}^{E}\delta\underline{\mathbf{D}}^{B} = \left(\left[K_F\right]_1 + \left[K_F\right]_2\right)\ {}^{E}\delta\underline{\mathbf{D}}^{B}.\end{aligned} \qquad (61)$$

where ${}^{B}\delta\underline{\mathbf{D}}^{T}$ is a small twist of body T in terms of body B and ${}^{E}\delta\underline{\mathbf{D}}^{B}$ is that of body B in terms of the inertial frame. $[K_F]_i$ and $[K_M]_i$ are the matrices for i-th spring defined in Eqs. (47) and (48), respectively.

The twist of body T can be decomposed as

$${}^{E}\delta\underline{\mathbf{D}}^{T} = {}^{E}\delta\underline{\mathbf{D}}^{B} + {}^{B}\delta\underline{\mathbf{D}}^{T} . \qquad (62)$$

From Eqs. (61) and (62), ${}^{E}\delta\underline{\mathbf{D}}^{B}$ can be expressed in terms of ${}^{E}\delta\underline{\mathbf{D}}^{T}$ as Eq. (63).

$$[K_F]_7\left({}^{E}\delta\underline{\mathbf{D}}^{T} - {}^{E}\delta\underline{\mathbf{D}}^{B}\right) + [K_M]_7\,{}^{E}\delta\underline{\mathbf{D}}^{B} = \left([K_F]_1 + [K_F]_2\right){}^{E}\delta\underline{\mathbf{D}}^{B}$$

$${}^{E}\delta\underline{\mathbf{D}}^{B} = \left([K_F]_1 + [K_F]_2 + [K_F]_7 - [K_M]_7\right)^{-1}[K_F]_7\,{}^{E}\delta\underline{\mathbf{D}}^{T} \qquad (63)$$

By substituting Eq. (63) for ${}^{E}\delta\underline{\mathbf{D}}^{B}$ in Eq. (61), $\delta\underline{\mathbf{f}}_7$ can be expressed in terms of ${}^{E}\delta\underline{\mathbf{D}}^{T}$ as Eq. (64).

$$\delta\underline{\mathbf{f}}_7 = \left([K_F]_1 + [K_F]_2\right)\left([K_F]_1 + [K_F]_2 + [K_F]_7 - [K_M]_7\right)^{-1}[K_F]_7\,{}^{E}\delta\underline{\mathbf{D}}^{T} \qquad (64)$$

Analogously, $\delta\underline{\mathbf{f}}_8$ and $\delta\underline{\mathbf{f}}_9$ can be written as Eqs. (65) and (66), respectively.

$$\delta\underline{\mathbf{f}}_8 = \left([K_F]_3 + [K_F]_4\right)\left([K_F]_3 + [K_F]_4 + [K_F]_8 - [K_M]_8\right)^{-1}[K_F]_8\,{}^{E}\delta\underline{\mathbf{D}}^{T} \qquad (65)$$

$$\delta\underline{\mathbf{f}}_9 = \left([K_F]_5 + [K_F]_6\right)\left([K_F]_5 + [K_F]_6 + [K_F]_9 - [K_M]_9\right)^{-1}[K_F]_9\,{}^{E}\delta\underline{\mathbf{D}}^{T} \qquad (66)$$

Then from Eq. (57) and Eqs. (64)-(66), the stiffness matrix is obtained as Eq. (67).

$$\begin{aligned}[K]_R = &\left([K_F]_1 + [K_F]_2\right)\left([K_F]_1 + [K_F]_2 + [K_F]_7 - [K_M]_7\right)^{-1}[K_F]_7 \\ &+ \left([K_F]_3 + [K_F]_4\right)\left([K_F]_3 + [K_F]_4 + [K_F]_8 - [K_M]_8\right)^{-1}[K_F]_8 . \\ &+ \left([K_F]_5 + [K_F]_6\right)\left([K_F]_5 + [K_F]_6 + [K_F]_9 - [K_M]_9\right)^{-1}[K_F]_9\end{aligned} \qquad (67)$$

3.2c.11 Numerical Example

A numerical example of the compliant mechanism depicted in Figure 3.2c.16 is given. The four bodies are identical equilateral triangles whose edge length is 2 cm. Four coordinate systems, B, C, D, and T are attached to body B, C, D, and T, respectively and their positions of origin and orientations in terms of the inertial frame are given in Table 3. The spring properties and the positions of fixed pivot points are given in Table 1 and Table 2, respectively. The external wrench is given below.

$$\underline{\mathbf{w}}_{ext} = \begin{bmatrix} 0.1 & N \\ 0.1 & N \\ 0.2 & Ncm \end{bmatrix}$$

Table 1. Spring properties of the compliant coupling in Figure 3.2c.16

Spring No.	1	2	3	4	5	6	7	8	9
Stiffness constant k	0.40	0.43	0.49	0.52	0.58	0.61	0.46	0.55	0.64
Free length l_o	2.2547	2.4014	1.5910	1.8450	1.7077	2.2695	2.3924	2.2200	1.8711

(Unit: N/cm for k and cm for l_o)

Table 2. Positions of fixed pivot points of the compliant coupling in Figure 3.2c.16

	A1	A2	A3	A4	A5	A6
X	1.6700	4.4600	13.3449	14.6731	8.2300	4.9400
Y	4.4333	1.3964	3.2500	6.8400	14.1400	13.4943

(Unit: cm)

Table 3. Positions and orientations of coordinates systems in Figure 3.2c.16

	Bo	Co	Do	To
x	4.0746	12.2367	7.2479	8.3174
y	5.1447	4.4972	12.7430	6.9958
Φ	-0.8112	1.2283	3.8876	0.5818

(Unit: cm for x, y and radians for Φ)

Two stiffness matrices are obtained. $[K_1]$ is from Eq. (67) and $[K_2]$ from the same equation ignoring all $[K_M]$'s which are newly introduced in this research.

$$[K_1] = \begin{bmatrix} 0.2501 & N/cm & 0.0216 & N/cm & -1.7651 & N \\ 0.0216 & N/cm & 0.2910 & N/cm & 2.6661 & N \\ -1.6651 & N & 2.5661 & N & 38.5180 & Ncm \end{bmatrix}$$

$$[K_2] = \begin{bmatrix} 0.2463 & N/cm & 0.0172 & N/cm & -1.7844 & N \\ 0.0315 & N/cm & 0.2888 & N/cm & 2.5749 & N \\ -1.6139 & N & 2.5730 & N & 38.2221 & Ncm \end{bmatrix}$$

To evaluate the result, a small wrench $\delta \underline{\mathbf{w}}$ is applied to body T and the static equilibrium pose of the mechanism is obtained by a numerically iterative method. From the equilibrium pose of the mechanism, the twist of body T with respect to ground ${}^{E}\delta \underline{\mathbf{D}}^{T}$ is obtained as below.

$$\delta \underline{\mathbf{w}} = 10^{-4} \times \begin{bmatrix} 0.5 & N \\ 0.2 & N \\ 0.3 & Ncm \end{bmatrix}$$

$${}^{E}\delta \underline{\mathbf{D}}^{T} = \begin{bmatrix} 0.0050 & cm \\ -0.0058 & cm \\ 0.0006 & rad \end{bmatrix}$$

Then the twist ${}^{E}\delta \underline{\mathbf{D}}^{T}$ is multiplied by both of the stiffness matrices to see if they result in the given small wrench $\delta \underline{\mathbf{w}}$.

$$\delta \underline{\mathbf{w}}_1 = [K_1]\, {}^{E}\delta \underline{\mathbf{D}}^{T} = 10^{-4} \times \begin{bmatrix} 0.4997 & N \\ 0.2000 & N \\ 0.3020 & Ncm \end{bmatrix}$$

$$\delta \underline{\mathbf{w}}_2 = [K_2]\, {}^{E}\delta \underline{\mathbf{D}}^{T} = 10^{-4} \times \begin{bmatrix} 0.4502 & N \\ 0.2726 & N \\ 0.6622 & Ncm \end{bmatrix}$$

The numerical example indicates that $[K_1]$ produces the given wrench $\delta \underline{\mathbf{w}}$ with high accuracy and that $[K_2]$ involves significant errors.

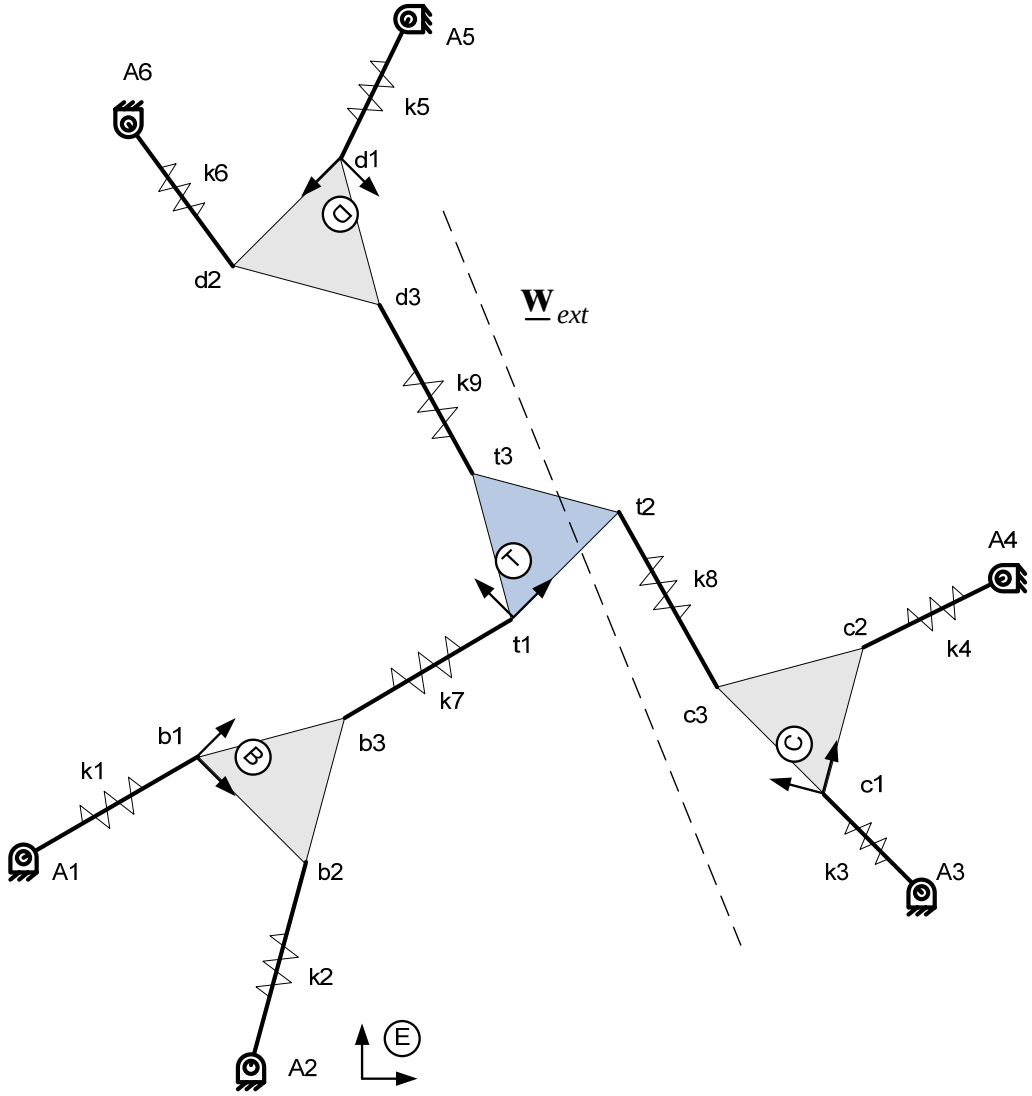

Figure 3.2c.16. Compliant mechanism with hybrid arrangement of springs

3.2c.12 References

- Ball, R. S., 1990. A Treatise on the Theory of Screws. Cambridge University Press, London.
- Chen, S. and Kao, I., 2000. Conservative Congruence Transformation for Joint and Cartesian Stiffness matrices of Robotic Hands and Fingers, International Journal of Robotic Research, Vol. 19 No. 9.
- Ciblak, N. and Lipkin, H., 1994. Asymmetric Cartesian Stiffness for the Modeling of Compliant Robotic Systems. Proc. ASME 23rd Biennial Mech. Conf., Des. Eng. Div., New York, NY, Vol.72.
- Ciblak, N. and Lipkin, H., 1999. Synthesis of Cartesian Stiffness for Robotic Applications. Proceedings of the IEEE International Conference on Robotics and Automation, pp. 2147–2152, Detroit, MI, May.
- Crane, C. D. and Duffy, J., 1998. Kinematic Analysis of Robot Manipulators. Cambridge University Press.
- Crane, C. D., 2003. Class notes from Robot Geometry II. University of Florida, Gainesville.
- Craig, J. J., 1989. Introduction to Robotics: Mechanics and Control. Addison Wesley, Reading, MA.
- Dimentberg, F. M., 1965. The Screw Calculus and its Applications in Mechanics. Foreign Technology Division, Wright-Patterson Air Force Base, Ohio. Document No. FTD-HT-23-1632-67.
- Duffy, J., 1996. Statics and Kinematics with Applications to Robotics. Cambridge University Press.
- Featherstone, J., 1985. Robot Dynamics Algorithms. Kluwer Academic Publishers.
- Griffis, M., 1991. A Novel Theory for Simultaneously Regulating Force and Displacement. PhD dissertation, University of Florida, Gainesville.
- Henrie, A. M., 1997. Variable Compliance via Magneto-Rheological Materials. M.S. Thesis, Brigham Young University.
- Huang, S. and Schimmels, J. M., 1998a. The Bounds and Realization of Spatial Stiffness Achieved with Simple Springs Connected in Parallel. IEEE Transactions on Robotics and Automation, Vol.14 No.3, pp. 466-475.
- Huang, S., 1998b. The Analysis and Synthesis of Spatial Compliance," PhD dissertation, Marquette University, Milwaukee, WI.
- Kane, T. R. and Levinson, D. A., 1985. Dynamics: Theory and Applications. McGraw, New York.
- Loncaric, J., 1985, Geometrical Analysis of Compliant Mechanisms in Robotics. PhD thesis, Harvard University, Cambridge, MA.
- Loncaric, J., 1987. Normal Forms of Stiffness and Compliance Matrices. IEEE Journal of Robotics and Automation, Vol.3, pp. 567–572.
- McCarthy, J. M., 1990. Introduction to Theoretical Kinematics. MIT Press.
- McLachlan, S. and Hall, T., 1999. Robust Forward Kinematic Solution for Parallel Topology Robotic Manipulator. 32nd ISATA Conference – Track : Simulation, Virtual Reality and Supercomputing Automotive Applications, pp 381-388, Vienna, Austria.
- Peshkin, M., 1990. Programmed Compliance for Error Corrective Assembly. IEEE Transactions on Robotics and Automation, Vol.6 No.4.
- Pigoski, T., 1993. An Introductory Theoretical Analysis of Planar Compliant Couplings. M.S Thesis, University of Florida, Gainesville.

- Ryan, M.W., Franchek, M.A., and Bernhard, R., 1994. Adaptive-Passive Vibration Control of Single Frequency Excitation Applied to Noise Control. Noise-Con Proceedings, 461-466, Fort Lauderdale, Florida.
- Roberts, G. R., 1999. Minimal Realization of a Spatial Stiffness Matrix with Simple Springs Connected in Parallel. IEEE Transactions on Robotics and Automation, Vol.15 No.5.
- Salisbury, J. K., 1980. Active Stiffness Control of a Manipulator in Cartesian Coordinates. Proc. 19th IEEE Conference on Decision and Control, Albuquerque, NM, pp.87-97.
- Simaan, N. and Shoham, M., 2002. Stiffness Synthesis of a Variable Geometry Planar Robots. Advances in Robot Kinematics, 8th ARK, Kluwer Academic Publisher, Spain.
- Whitney, D. E., 1982. Quasi-static assembly of compliantly supported rigid parts. ASME Journal of Dynamic Systems, Measurement, and Control, Vol.104, pp. 65-77.

3.2d Optimized Dense Packing of Waste Containers

3.2d.1 Objective

The objective of this subtask is to develop algorithms to allow the dense packing of containers by using robotics and robot mechanisms. The algorithm will consider geometric, as well as radiation properties, in order to maximize the amount of materials that can be safely stored in a designated storage container. The research can aid NNSA and DOE in short- or long-term storage of radioactive materials regardless of their shapes. The dense packing of containers also will be a valuable tool to assist in repackaging mixed waste materials currently in storage. The result will allow for current materials to be sorted and then packed into a smaller volume.

3.2d.2 Background

This algorithm would assist a human operator by developing a systematic packing scheme that would result in a much more densely packed container subject to several side constraints. The algorithm can also be integrated with object recognition and classification processes being developed at the University of Tennessee, manipulation systems being developed at the University of Texas, and process control software being developed at the University of New Mexico to result in an automated sorting and packing system.

3.2d.3 Approach to Three Dimensional Placement Heuristic

The three dimensional heuristic must be modular (object oriented), have the same inputs as the two dimensional heuristic to be able to be coupled into the main structure of the algorithm, and they should be fast.

3.2d.4 Two vs. Three Dimensional Cases

The reasoning behind implementing a two-dimensional bin packing was to ensure a smoother transition to the complex three-dimensional case. Several parallels can be drawn from one case to another thus making the tractability of the problem less intense. Presented below are the parameters that are extended to the three-dimensional case and the impact of their implementation.

3.2d.4.1 Problem Statement

2D:

The two-dimensional case considered densely packing two dimensional polygons into a rectangular container with infinite height.

3D:

The three-dimensional case must densely pack three dimensional arbitrary shapes into a three dimensional container with infinite height. The shape of the container will be assumed to be a box with infinite height. Figure 3.2d.1 shows the two overall cases and their differences.

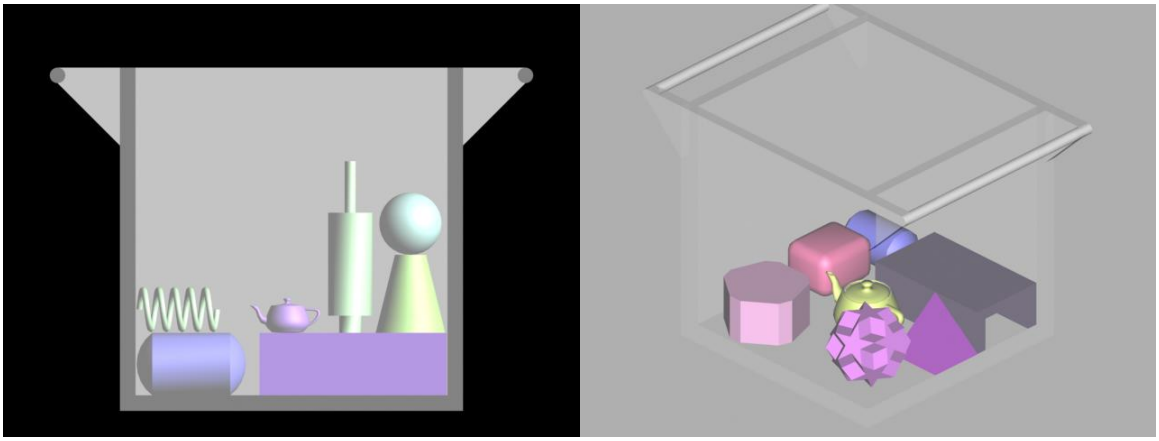

Figure 3.2d.1: Two and Three Dimensional Bin Packing

3.2d.4.2 Profile

In general terms the profile is the shape of the top layer in a packing configuration where the next object to be packed will be placed.

2D:

The two dimensional case considered a non-decreasing piecewise linear function as the profile.

3D:

The three-dimensional problem translates the two dimensional piecewise linear function into a three dimensional "blanket." Figure 3.2d.2 shows the translation between the two cases.

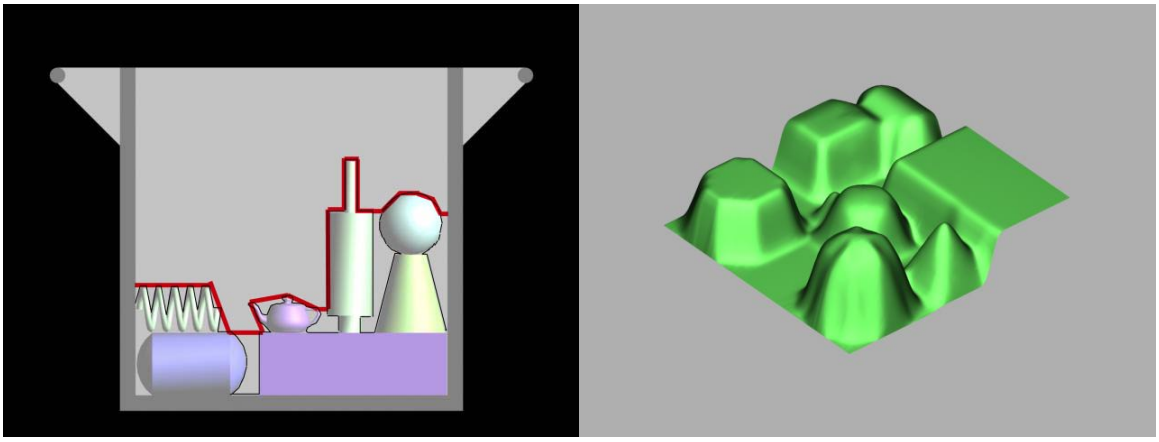

Figure 3.2d.2: Two and Three Dimensional Profiles

3.2d.4.3 Objective Function

Although the problem considers the dense packing of objects into a container it must also take into account feasible placements of the incoming parts. For this reason the problem must take into account stable placements as part of the objective function.

2D:

The two-dimensional case considered a "Potential Energy" function which took into account not only the void or unused area when packing but also the height of the packed objects as well. The potential energy was defined as follows:

$$PE = (P_a + P_v) * Pc_y$$

Where P_a represents the current part's area, P_v is the current part's contribution to the overall void area and Pc_y is the current part's centroid. The reasoning behind minimizing the overall height is to avoid a tower of placed objects that although might have low void space, are not stable and can topple over.

3D:

The three-dimensional case also utilizes the same formula as its two-dimensional counterpart but reflecting the three dimensional nature of the problem. In the "Potential Energy" formula P_a is the current part volume, P_v is the current part contribution to the overall void space and Pc_y is the current part centroid height.

3.2d.5 Placement Heuristic

2D:

On the two-dimensional case the placement heuristic aligned all the profile edges with all the part edges by following the following process:

Align vertex of the part j with a vertex of a profile i. Since each vertex shares two edges there are two alignments to be made, first the part edge composed of vertices j-1 and j with the profile edge composed of vertices i-1 and i. Once an alignment has been made the part is "dropped" and the "Potential Energy" calculated. The following Pseudo-Code 1 and Figure 3.2d.3 illustrate this process.

```
Begin
{
   Do for all vertices in profile i
   {
         Do for all vertices in part j
         {
                  alignPart( part vertex j, profile Vertex i)
                  alignPart( part edge (j-1, j), profile edge ( i-1,i))
                  currentPE=place(part)
                  if(currentPE<bestPE)
                           bestPE=currentPE
                  alignPart( part edge (j, j+1), profile edge ( i,i+1))
                  currentPE=place(part)
                  if(currentPE<bestPE)
                           bestPE=currentPE
         }
   }
}
```

Pseudo-Code 1: 2D Online Placement Heuristic

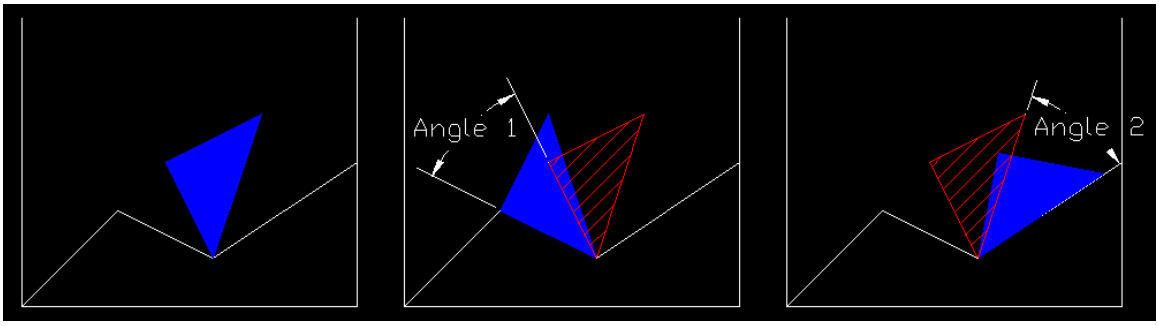

Figure 3.2d.3: a) Align Vertices, b) Align edges to the left, c) Align edges to the right.

3D:

The main idea behind aligning edges from the part and the profile in the two dimensional case was based on the assumption that a good placement must have at least one sharing edge between the part and the profile. The problem will be extended to account for not only the edges of the part and profile but also the non physical convex volume edges as well, which must also be included as part

of the aligning process since a part can sit on three points instead of two edges. The three-dimensional placement heuristic follows the steps of its two dimensional counterpart adding to it as needed. The overall process follows:

Align vertex of the part j with a vertex of a profile i (Figure 3.2d.4a). Each vertex now has a list of edges it shares. Thus the vertex j of the part has edges 1 thru u represented as $e_{j,u}$. In a similar fashion the profile's vertex i has edges 1 thru v represented as $e_{i,v}$. Align the first set of edges $e_{j,1}$ and $e_{i,1}$ from the part and profile respectively (Figure 3.2d.4b). We now have two sets of faces that can be aligned as seen on Figure 3.2d.4b. Align each of the two sets calculate the "Potential Energy" associated with these placements (Figure 3.2d.4c and 4d). As with the two-dimensional heuristic compare the best objective value with the current value and if the current placement yields a better objective value then make the current placement the best so far. The process then repeats itself for all the sets of edges for a specific vertex alignment and furthermore for all possible vertex alignments between the part and the profile. Pseudo-Code 2 and Figure 3.2d.4 illustrate this process.

```
Begin
{
   Do for all vertices in the profile i
   {
         Do for all vertices in part j
         {
                  align the vertices(i, j)
                  Do for all the edges coincident with i and j
                  {
                  align the first part face with the first profile face with coincident vertices i and j.
                  currentPE = place(part)
                  if(currentPE<bestPE)
                           bestPE=currentPE
                 align the second part face with the second profile face with coincident vertices i, j.
                  currentPE = place(part)
                  if(currentPE<bestPE)
                           bestPE=currentPE
                  }
}
   }
}
```

Pseudo-Code 2: Proposed Online 3D Placement Heuristic

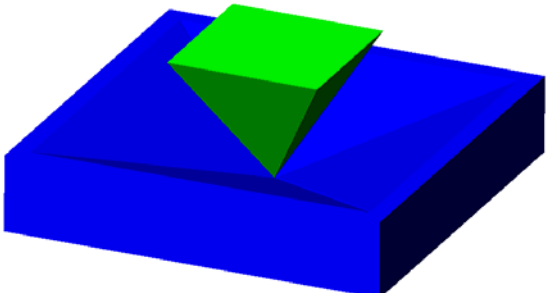

Figure 3.2d.4a: Part and Profile vertices aligned

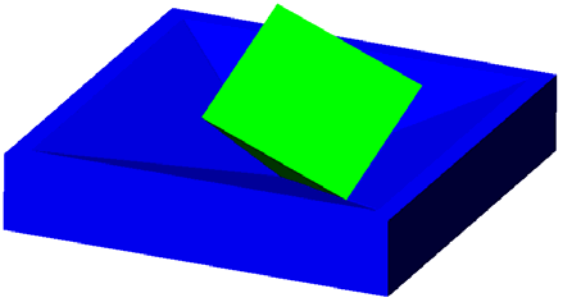

Figure 3.2d.4b: Edge Alignment

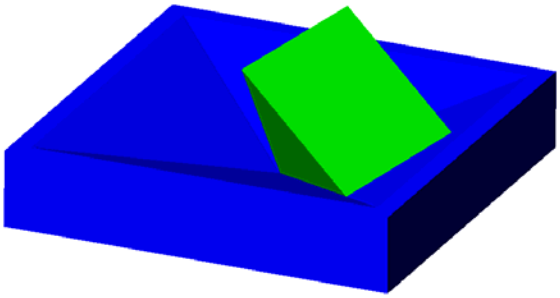

Figure 3.2d.4c: First Face Alignment

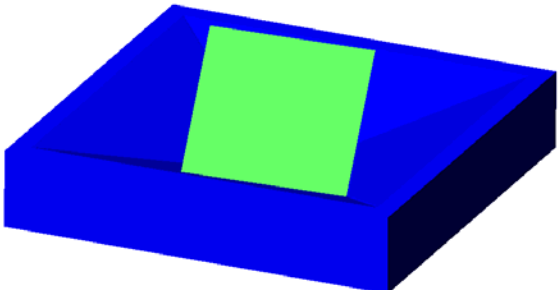

Figure 3.2d.4b: Second Face Alignment

3.2d.6 Programming Considerations

In order to simplify the placement heuristic added classes will be required for the three dimensional data structure of the part and the profile. The part and profile must hold as one of its members a new data structure called edgelist. The edgelist class will be a list of edges for the part and profile indexed by vertex. This way the heuristic has the means of accessing the required edges and faces for alignment.

3.2d.7 Hybrid Combinatorial Algorithm for the Three-Dimensional Case

The offline ordering algorithm takes packing orderings and based on an "Energy" function will create a new ordering or move. The main approach was slightly changed from the original Simulated Annealing / Genetic Algorithms methodology used in the two dimensional case to allow for a more in depth integration of the genetic approach by making the algorithm "Evolutionary" in its outer loop. The main structure is outlined in Figure 3.2d.5.

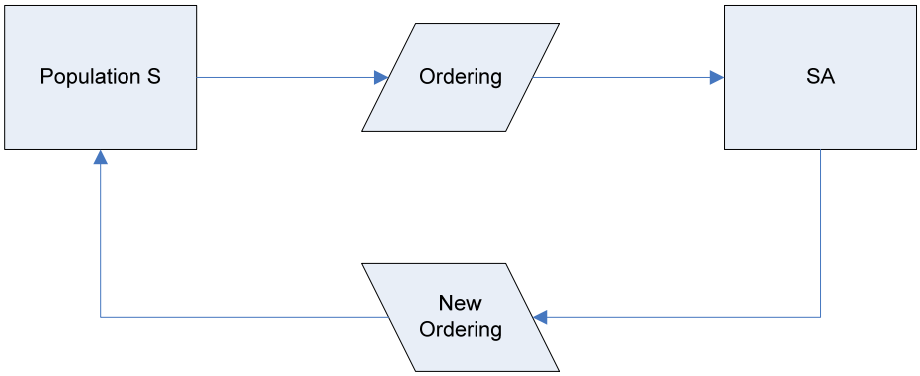

Figure 3.2d.5: Proposed Evolutionary Simulated Annealing Algorithm Main Structure

3.2d.8 Evolutionary Phase

Generate a population S $\{S_1, S_2, S_3, \ldots, S_s\}$ of s random orderings. One ordering will be randomly selected from the population. This ordering will now be passed to the Simulated Annealing Phase and once the temperature schedule for the SA has finished the resulting ordering will be placed back into the population S and a new ordering will be selected again. This process will continue until a termination criterion has been satisfied. The advantage of using an evolutionary outer phase is that the algorithm can now be implemented in a distributed environment which can greatly reduce the computational time. All the parallel platforms would contain the Simulated Annealing functions and they will all draw orderings from a single population replacing the ordering after the termination of each of their respective temperature schedules.

3.2d.9 Simulated Annealing Structure

The Simulated Annealing algorithm will randomly take one of the orderings from population S and run SA on it. The main structure of simulated annealing can be seen on Figure 3.2d.6.

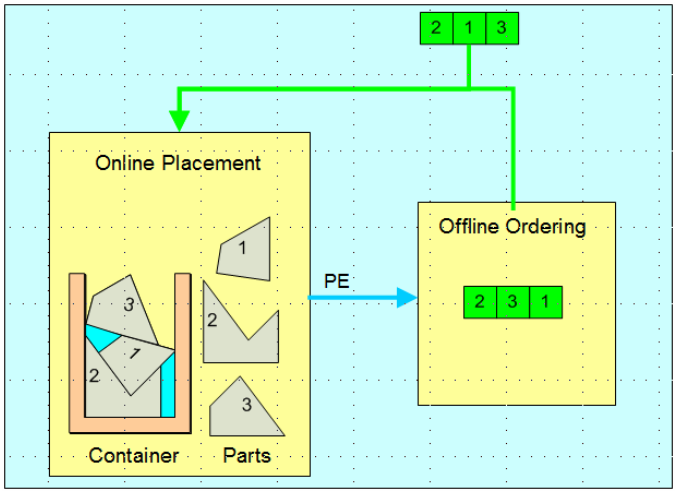

Figure 3.2d.6: Simulated Annealing Structure

The process begins by calculating the Potential Energy for the current part. This is done by passing the current ordering of parts to the online placement heuristic which in turn will place the parts accordingly and return a Potential Energy value to the SA. The SA offline algorithm will now generate a new ordering based on the previous one using a move function. A move function in this case is simply a function which generates a new ordering based on the previous or current one. This "new" ordering is now placed and its associated Potential Energy obtained. At this point the "Potential Energies" of the new and current orderings are compared. If the new Potential Energy is less than the current one then we accept or "move" to the new ordering. However if the new Potential Energy is not a better solution then the current, there is still a probability of accepting or "moving" to that new solution based on a probability. Thus the algorithm generates a random number ρ and compares this value with the probability of accepting an inferior move:

$$P = e^{-\frac{PE_{new} - PE_{curretn}}{T}}$$

This process is what gives the Simulated Annealing algorithm its "hill climbing" property. The parameter T specifies the current temperature at which the algorithm is running. At higher temperatures the probability of accepting inferior moves Pr will be very high (around 1) allowing the algorithm to accept inferior moves more often, thus making a more global search. At lower temperatures the probability P will decrease and the algorithm will conduct a more local search. Every simulated annealing algorithm has a temperature schedule which will dictate how the temperature T changes as the algorithm progresses. The temperature will always begin high to

allow the algorithm to perform a global search and be lowered at later stages dependent on the temperature schedule.

The move function has not been changed from the original two-dimensional case using the inver-over operator.

3.2d.10 Programming Goals

Due to the high computational complexity of the problem concern grew about the correct platform and programming approach to take. The initial programming for the two dimensional case was performed on an emulated Linux platform not running natively with the Lesstif API for the GUI and Open Inventor to be used for 3D graphics. The original algorithm took a built in performance hit based on the emulated Linux platform (which runs on top of Windows). There was also a concern for the programming approach which was a mixture of sequential and object-oriented programming, and as the problem was extended to three dimensions the programming would become very difficult to tract due to the sequential parts of the code. A decision was made to reprogram the two dimensional case running natively on a Windows platform using fully object oriented managed C++ code. Based on this fact the original programming milestones of programming the heuristic and the hybrid model have been pushed back. Additionally, there has been given consideration to program the algorithm using a distributed computing approach which is the reason for the addition of the "Evolutionary Phase" outer loop which was added to this work.

Another important aspect to report is that there is already expressed interest in this work for other commercial applications which would require software running on a Windows platform. The work was submitted to the technology license office of the University of Florida which after consideration decided that the work has the technological importance such that the University will assert its right to it.

3.2d.11 References

- [LI99] C++ Unleashed, Jesse Liberty et. al. , Sams Publishing, 1999.
- [LA98] Waite Group's Object-Oriented Programming in C++, Third Edition, Robert LaFore, Macmillan Computer Publishing, 1998.
- [Pa03] A. Pasha, Geometric Bin Packing Algorithm for Arbitrary Shapes, Masters Thesis, University of Florida, Gainesville FL, 2003.
- [IB97] I. Ikonen, W.E. Biles, "A Genetic Algorithm for Optimal Object Packing in a Selective Sintering Rapid Prototyping Machine", Proceedings for the 7th International FAIM Conference, University of Teeside, Middlesbrough, England, June 25-27, 1997.

- [Sy95] S. Szykman, Optimal Product Layout Using Simulated Annealing, Thesis, Carnegie Mellon University, Pittsburg PA, 1995.
- [Me53] N. Metropolis, A. W. Rosenbluth, M. N. Rosenbluth, A. H. Teller, and E. Teller. J. Chem. Phys., 21, 1087, 1953
- [Ki83]S. Kirkpatrick, J.C.D. Gellat, M.P. Vecchi, Optimization by Simulated Annealing, Science, 13, 220(4598), pp. 671-680, 1983
- [SY99] Sadiq M. Sait and Habib Youssef, Iterative Computer Algorithms with Applications in Engineering, IEEE Computer Society Press, 1999
- [Ik98] I. Ikonen, A Genetic Algorithm for a Three-Dimensional Non-Convex Bin Packing Problem, Thesis, University of Louisville, 1998.
- [GL97] F. Glover, M. Laguna, Tabu Search, Kluwer, MA, 1997
- [KB87] R. M. Kling, P. Banerjee. ESP: "A new standard cell placement package using simulated evolution". Proceedings of 24th Design Automation Conference, pp. 60-66, 1987.
- [Sa89] Y. G. Saab, Combinatorial optimization by stochastic evolution with applications to the physical design of VLSI circuits. Doctoral dissertation, University of Illinois, Urbana, 1990.
- [DD99] Dorigo M. and G. Di Caro (1999). The Ant Colony Optimization Meta-Heuristic. In D. Corne, M. Dorigo and F. Glover, editors, New Ideas in Optimization, McGraw-Hill, 11-32.
- [EK95] R.C. Eberhart, J. Kennedy, A new optimizer using particle swarm theory. Proceedings of the Sixth International Symposium on Micromachine and Human Science, Nagoya, Japan. pp. 39-43, 1995

UF 1.2.6 APPENDIX

High Dose Co-60 Gamma Irradiation of InGaN Quantum Well Light-Emitting Diodes

Papers submitted for publication:

"High Dose Co-60 Gamma Irradiation of InGaN Quantum Well Light-Emitting Diodes," Rohit Khanna, Sang Youn Han and S. J. Pearton, Department of Materials Science and Engineering, University of Florida, Gainesville, FL 32611

D. W. Schoenfeld

Department of Nuclear and Radiological Engineering, University of Florida, Gainesville, FL 32611

W. V. Schoenfeld

CREOL, University of Central Florida, Orlando, FL 32816

F. Ren

Department of Chemical Engineering, University of Florida, Gainesville, FL 32611

ABSTRACT

InGaN multi-quantum-well light-emitting diodes (LEDs) in the form of unpackaged die with emission wavelengths from 410-510 nm were irradiated with ^{60}Co γ-rays with doses in the range 150-750 Mrad (Si). The forward turn-on voltage for all the irradiated LEDs was increased slightly (eg. by only ~0.1-0.15 V for 500 MRad dose irradiation) while the reverse breakdown voltage was unchanged within experimental error. The light output intensity for the 410nm diodes was decreased by 20% after a dose of 150 MRad and 75% after 750 MRad. The current transport in the LEDs was dominated by generation-recombination (ideality factor ~2) both before and after irradiation. The morphology and appearance of the p and n-Ohmic metallization did not show any detectable change as a result of even the highest γ-ray dose.

There continues to be strong interest in the development of GaN/InGaN multi quantum well (MQW) light-emitting diodes (LEDs)[1-8] .These are commercially available in a broad range of visible wavelengths for use in applications including architectural and stage lighting, indoor and outdoor accent lighting, traffic and railway signaling, commercial and retail signs and displays, outdoor illumination and traffic lights. There is also interest in shorter wavelength LEDs with high Al content AlGaN active regions, for use in emerging bio-remediation and detection systems [7,9,20]. The most promising application for nitride LEDs will be in white lighting, where color-combining of red, green and blue LEDs or pumping of phosphors can be used for general room lighting [7-20] .There is a $12 billion-a-year market for sources of white light, including light bulbs and fluorescent tubes [21]. There is also strong interest in the effects of directly or indirectly ionizing radiation on nitride-based devices, for space-based applications and radiation-monitoring [22-28]. In this situation, a premium is placed on radiation-resistance. InGaN/GaN light-emitting devices showed only small changes (<10%) in their electrical characteristics for 2-40 MeV proton irradiation at doses equivalent to 100 years in low-earth orbit[24] and to neutron and energetic electron fluxes[25-28], although the optical output intensity was more significantly degraded. In general, GaN is reported to be 2-3 orders of magnitude more resistant than GaAs to decreases in its luminescence due to proton or electron irradiation [24,25,27,28] .This is a result of the higher displacement threshold energy (Td) in GaN [25].

In this letter, we report on the effect of Co-60 γ-rays on GaN/InGaN MQW LEDs at very high doses of up to 750 MRad (Si). Exposure of semiconductor devices to gamma ray fluxes can produce displacement damage and eventual device failure. Minority carrier devices such as LEDs that rely on carrier lifetime for their operation are expected to be the most sensitive to radiation damage. The behavior of neutral radiation like gamma rays passing through semiconductors is fundamentally different than the interaction with charged particles such as protons, electrons or alpha particles and the energy loss mechanisms are the photoelectric effect, Compton scattering and pair production. We find that unpackaged InGaN/GaN LEDs with emission wavelengths in the range 410-510 nm are still operational after exposure to very large doses (750Mrad (Si)) of Co-60 γ-rays, showing that these devices are indeed radiation-hard and that other issues such as degradation of the epoxy lens will likely be more important in high γ-ray flux environments.

The GaN LEDs were commercial unpackaged die from UniRoyal Optoelectronics with four different emission wavelengths, namely 410, 445, 465 and 510 nm. The maximum output powers were 3 mW in the first three cases and 1.6 mW in the final case. The forward voltages (defined as the voltage at which the current density is 50 mA/cm^2) were ~3.3 V for the 410,445 and 465 nm devices and ~3.1 V for the 510 nm devices. The epitaxial structures with InGaN multi-quantum wells and GaN cladding layers were grown by metal organic chemical vapor deposition on sapphire substrates. Figure 1 shows an optical microscope image of one of these dies. The devices were exposed to a 600Ci ^{60}Co source for accumulated doses up to 750 Mrad. The calibration of dose was performed with radioactive films and ion chamber radiation meters. The absorption depth of the gamma rays is >500 μm in GaN and sapphire and therefore the radiation traverses the entire epi structure and the sapphire substrate. The irradiated devices were measured approximately 7 days after exposure. The forward and reverse current-voltage(I-V) characteristics before and after irradiation were measured at 25°C on an Agilent 4156C parameter analyzer with the die heat-sink on a probe station. The optical output intensity with fixed LED placement in the test fixture was recorded at room temperature with an emission spectrometer.

As an example of the effect of high γ-ray doses, Figure 2 shows the time dependence of forward voltage (defined as the voltage at which the current density is 50 mA/cm^2) from 410 nm diodes, both before and after irradiation up to 500 MRad (Si). We measured the forward voltage as a function of time with bias applied to check for any post-irradiation annealing effects that might occur. The forward voltage was increased only slightly (~0.1-0.15V) by the γ-ray exposure at doses of 250-500 MRad. Similar results were obtained from the LEDs of longer wavelengths. The ideality factor of all the LEDs was ≥ 2 even prior to γ-irradiation, indicating that recombination is the dominant transport mechanism. The forward voltage (V_F) of the p-i-n junction can be written in terms of the applied voltage V_A as $\mathbf{V_F} = V_A - V_B$, where V_B is the built-in voltage given by $V_B=(e/2\varepsilon)/N_D x_d^2 + /N_A x_a^2$.In the latter equation, e is the electronic charge, ε is the dielectric constant ,$N_{D,A}$ and $x_{d,a}$ are the donor(acceptor) concentrations and depletion depths in the two end regions of the p^+-n-n^+ (the p^+-n and n^+-n regions) [29,30]. In a typical LED, the forward current includes terms from the diffusion recombination and tunnel currents. The small increase in turn-on voltage as a result of γ-ray irradiation may be due to several factors, including a decrease in the hole concentration on the p-side of the junction through creation of deep hole traps and introduction of shallow donors

such as nitrogen vacancies. Even though γ-rays are not directly ionizing, they can lead to atomic displacements through secondary effects. Surface effects are less likely due to the very long range of the γ-rays, in this case longer than the thickness of the die, so that a uniform damage path is expected.

Figure 3 shows the change in output light intensity measured from the electroluminescence (EL) spectra before and after irradiation, as a function of the total γ-ray dose for the 410 nm LEDs. The forward voltage was held constant at 3.5 V during the measurement. Note that the decrease in light output in UF's case is intrinsic to the unpackaged InGaN/GaN structure and not to extrinsic factors such as degradation of the epoxy lens package which is known to degrade during reliability testing experiments [31]. The longer wavelength LED showed similar degrees of light output degradation with dose and all were still functional with ~25% of the initial emission intensity after a dose of 750 MRad. Therefore, the In-content in the quantum well active regions does not appear to influence the radiation hardness of the LEDs over the range available to us. The appearance and morphology of both the n-and p-metallization was also unchanged by the irradiation up to the maximum dose.

The reverse bias breakdown voltage (defined as the voltage at which the reverse current density is $1 mA.cm^{-2}$) of the LEDs was not degraded by any of the doses we investigated. Figure 4 shows the dependence of reverse breakdown voltage on dose for all four wavelength LEDs investigated. Within experimental error there was no change for any of UF's conditions. Moreover, the reverse current density was essentially unchanged, indicating minimal change in carrier density or mobility as a result of the irradiation. This suggests that the main degradation mechanism is introduction of non-radiative centers at a low enough density that they do not significantly affect the electrical properties.

In conclusion, γ-irradiated GaN/InGaN MQW LEDs exhibit very small increases in forward voltage even after total doses of 750 MRad. Their electroluminescence characteristics are more affected by the irradiation, suggesting that the main degradation mechanism is creation of recombination centers. These devices appear well-suited for both aerospace and terrestrial applications where irradiation hardness is a prerequisite.

ACKNOWLEDGMENTS

The work at UF is partially supported by AFOSR grant under grant number F49620-03-1-0370, by the Army Research Office under grant no. DAAD19-01-1-0603, NSF (CTS-0301178, monitored by Dr. M. Burka and Dr. D. Senich) and the National Science Foundation (DMR

0400416, Dr. L. Hess). This work was also supported from the post-doctoral fellowship program of Korea Science & Engineering Foundation and Samsung Electro-Mechanics.

References

1. See, for example, Introduction to Solid-State Lighting, A. Zukauskas, M. S. Shur and R. Gaska (Wiley and Sons, NY 2002).

2. Introduction to Nitride Semiconductor Blue Lasers and Light-Emitting Diodes, ed. S. Nakamura and S. F. Chichibu (Taylor and Francis, London, 2000).

3. X.A.Cao and S.D.Arthur, Appl.Phys.Lett.85 3971(2004).

4.X. A. Cao, S. F. LeBoeuf, M. P. D'Evelyn, S. D. Arthur, J. Kretchmer, C.H. Yan, and Z. H. Yang, Appl. Phys. Lett. **84**, 4313 (2004).

5.T.Mukai, S.Nagahama, N.Iwasa, M.Senoh and T.Yamada, J. Phys.Condens.Matter 13 7089 (2001).

6.X. A. Cao, J. M. Teetsov, M. P. D'Evelyn, D. W. Merfeld, and C. H. Yan, Appl. Phys. Lett. **85**, 7 (2004).

7. A.Yasan,R.McClintok,K.Mayes,S.R.Darvish,P.Kung,M.Razeghi and R.J.Molnar, Opto-Electronics Review 10 287(2002).

8. D. D. Koleske, A. J. Fischer, A. A. Allerman, C. C. Mitchell, K. C. Cross, S. R. Kurtz, J. J. Figiel, K. W. Fullmer, and W. G. Breiland ,Appl. Phys. Lett. 81, 1940 (2002).

9. M. Khizar, Z. Y. Fan, K. H. Kim, J. Y. Lin, and H. X. Jiang ,Appl. Phys. Lett. 86, 173504 (2005).

10. M. L. Nakarmi, K. H. Kim, M. Khizar, Z. Y. Fan, J. Y. Lin, and H. X. Jiang Appl. Phys. Lett. 86, 092108 (2005)

11. Y. Xi, J.-Q. Xi, Th. Gessmann, J. M. Shah, J. K. Kim, E. F. Schubert, A. J. Fischer, M. H. Crawford, K. H. A. Bogart, and A. A. Allerman Appl. Phys. Lett. 86, 031907 (2005

12. J. P. Zhang, X. Hu, Yu. Bilenko, J. Deng, A. Lunev, M. S. Shur, R. Gaska, M. Shatalov, J. W. Yang, and M. A. Khan Appl. Phys. Lett. 85, 5532 (2004)

13. K. Mayes, A. Yasan, R. McClintock, D. Shiell, S. R. Darvish, P. Kung, and M. Razeghi, Appl. Phys. Lett. 84, 1046 (2004)

14. K. H. Kim, Z. Y. Fan, M. Khizar, M. L. Nakarmi, J. Y. Lin, and H. X. Jiang Appl. Phys. Lett. 85, 4777 (2004)

15. A. Yasan, R. McClintock, K. Mayes, D. Shiell, L. Gautero, S. R. Darvish, P. Kung, and M. Razeghi Appl. Phys. Lett. 83, 4701 (2003)

16. V. Adivarahan, W. H. Sun, A. Chitnis, M. Shatalov, S. Wu, H. P. Maruska, and M. Asif Khan Appl. Phys. Lett. 85, 2175 (2004).

17. V. Adivarahan, S. Wu, W. H. Sun, V. Mandavilli, M. S. Shatalov, G. Simin, J. W. Yang, H. P. Maruska, and M. Asif Khan Appl. Phys. Lett. 85, 1838 (2004) .

18. H. Peng, E. Makarona, Y. He, Y.-K. Song, A. V. Nurmikko,J. Su, Z. Ren, M. Gherasimova, S.-R. Jeon, G. Cui, and J. Han,Appl.Phys.Lett. 85 1436(2004).

19. K. B. Nam, J. Li, M. L. Nakarmi, J. Y. Lin, and H. X. Jiang ,Appl. Phys. Lett. 84, 5264 (2004)

20. A. J. Fischer, A. A. Allerman, M. H. Crawford, K. H. A. Bogart, S. R. Lee, R. J. Kaplar, W. W. Chow, S. R. Kurtz, K. W. Fullmer, and J. J. Figiel ,Appl. Phys. Lett. 84, 3394 (2004)

21. G.Zorpette,IEEE Spectrum Online, May 9, 2005

22. M. Osinski, P. Perlin, H. Schone, A. H. Paxton, and E. W. Taylor. Electron. Lett., **33**, 1252 (1997).

23. R. Khanna, K. Allums, C.R. Abernathy, S.J. Pearton, J. Kim, F. Ren, R. Dwivedi, T.N. Fogarty and R. Wilkins, Appl. Phys. Lett. 85 3131 (2004).

24. F. Gaudreau, C. Carlone, A. Houdayer and S.M. Khanna, IEEE Transactions on Nuclear Science 48 1778 (2001).

25. A. Ionascut-Nedelcescu, C. Carlone, A. Houdayer, H.J. von Bardeleben, J.L. Cantin, and S. Raymond,IEEE Transactions on Nuclear Science, 49 2733(2002).

26. S.M. Khanna, D. Estan, L.S. Erhardt, A. Houdayer, C. Carlone, A. Ionascut-Nedelcescu, S.R. Messenger, R.J.Walters, G.P. Summers, J.H. Warner and Insoo Jun, IEEE Trans. Nucl. Sci, 51 2729 (2004).

27. C. Li and S. Subramanian, IEEE Trans Nucl.Sci.50 1998 (2003).

28. S.M. Khanna, D.Estan, A. Houdayer, H.C. Liu and R. Dudek, IEEE Trans Nucl.Sci.51 3585 (2004)

29.H. Hirayama,J. Appl. Phys. **97**, 091101 (2005)

30. M. Fukuda, Reliability and Degradation of Semiconductor Lasers and LEDs (Artech House, Boston, 1991).

31.M.Osinski and D.L. Barton, Chapter 6 in Introduction to Nitride Semiconductor Blue Lasers and Light-Emitting Diodes, ed. S. Nakamura and S. F. Chichibu (Taylor and Francis, London, 2000).

Figure Captions

Figure 1. Optical micrograph of the 410 nm LED die .The central circular contact is the p-metal while the surrounding area is the n-metal.

Figure 2.Variation of forward turn-on voltage in 410 nm LEDs as a function of measurement time after various ^{60}Co γ-ray doses .Turn-on voltage is defined as the voltage at which the forward current is 50 mA. The data for the unirradiated diodes are from a total of 15 die whose data are overlapped, for the 250MRad samples there were 6 die and for the 500 MRad samples there were 18 die.

Figure 3. Emission spectra from 410nm LEDs as a function of ^{60}Co γ-rays doses .The forward voltage was held constant at 3.5V during the measurement.

Figure 4. Variation of reverse breakdown voltage in 410, 440 465 nm and 510 nm LEDs as a function of ^{60}Co γ-ray dose.

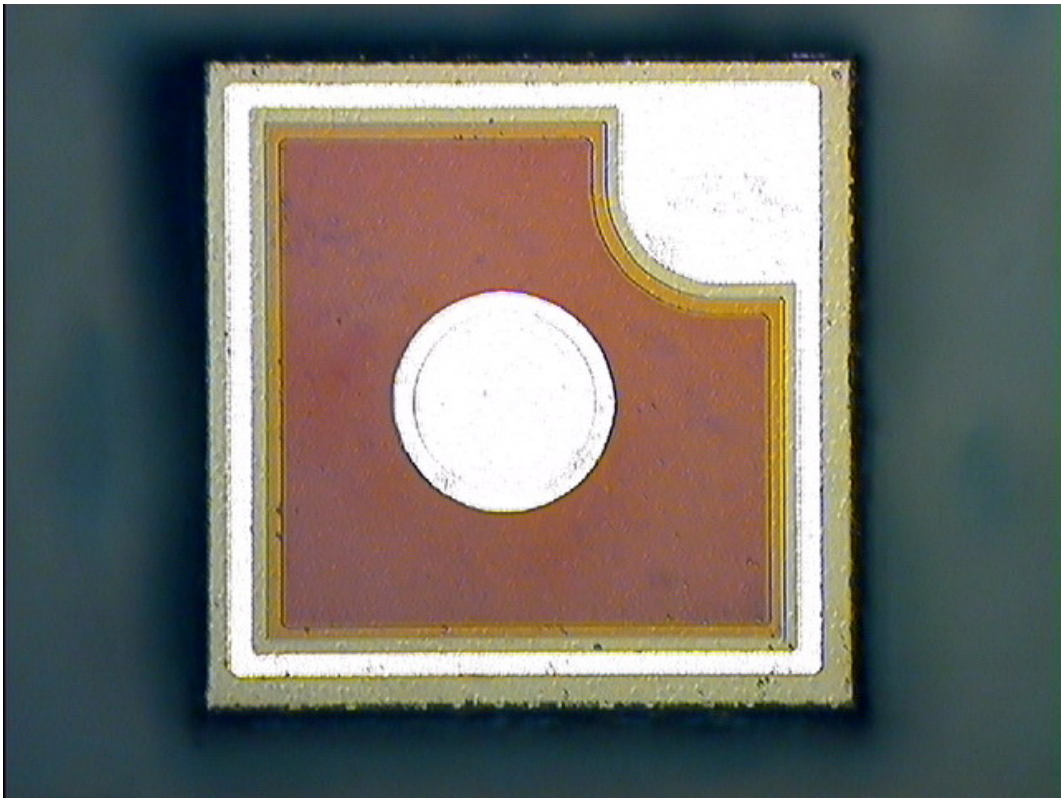

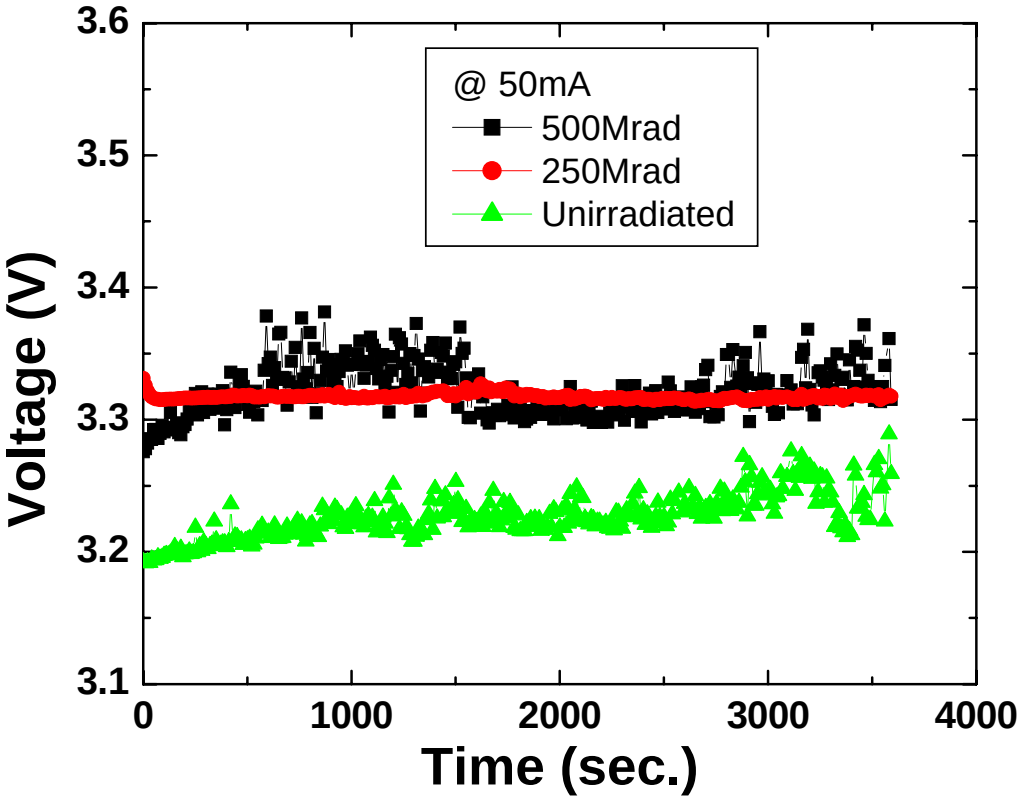
@ 50mA
500Mrad
250Mrad
Unirradiated
Voltage (V)
Time (sec.)
3.6
3.5
3.4
3.3
3.2
3.1
0
1000
2000
3000
4000

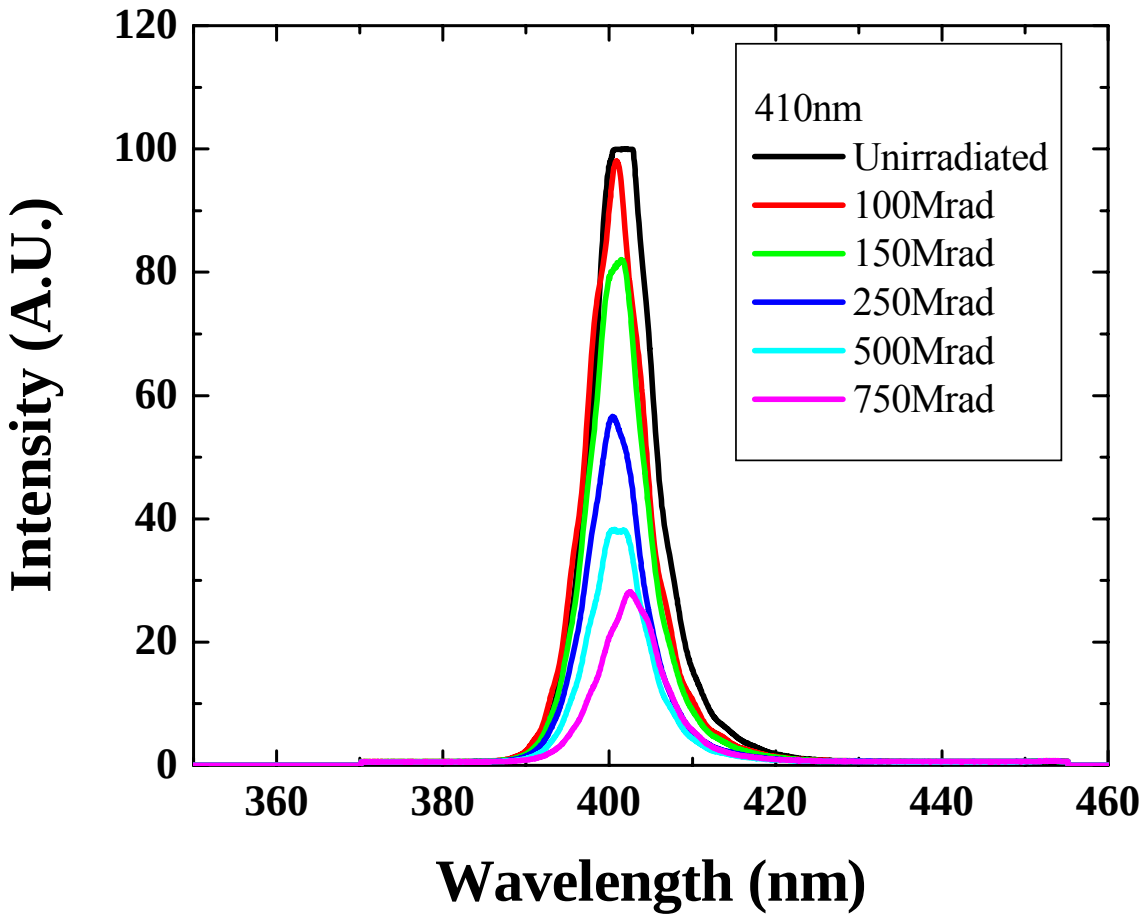
120
100
80
60
40
20
0
Intensity (A.U.)
360
380
400
420
440
460
Wavelength (nm)
410nm
Unirradiated
100Mrad
150Mrad
250Mrad
500Mrad
750Mrad

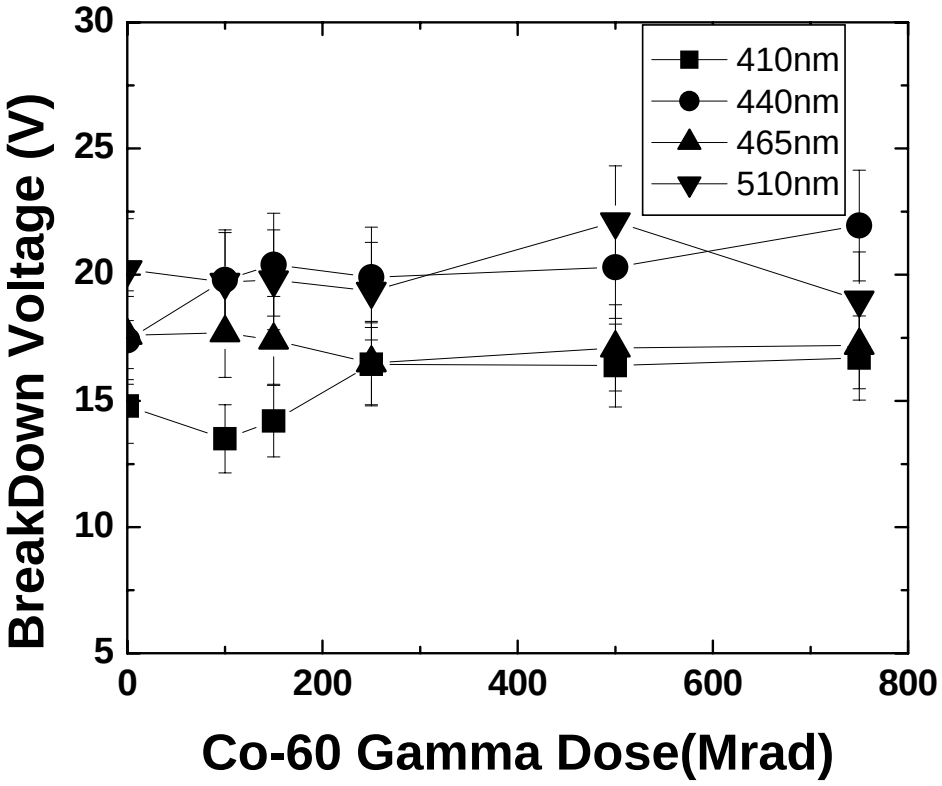
BreakDown Voltage (V)
30
25
20
15
10
5
0
200
400
600
800
Co-60 Gamma Dose(Mrad)
410nm
440nm
465nm
510nm